Retrieval of Sea Ice Parameters Using Fusion of High Resolution Model and Remote Sensing Data

by

© *Siva Prasad*

A thesis submitted to the

School of Graduate Studies

in partial fulfilment of the

requirements for the degree of

Doctor of Philosophy

Faculty of Engineering and Applied Sciences

Memorial University of Newfoundland

June 2018

St. John's Newfoundland

Abstract

This thesis discusses the retrieval of sea ice parameters using the combination of remote sensing data and a sea ice model for the region of the Baffin Bay, Hudson Bay, Labrador Sea and the Gulf of St. Lawrence. The Los Alamos sea ice model, CICE, which is used as a module for coupled global ice-ocean models, was used for this work. The model was implemented with a 7-category thickness distribution, open boundaries and a variable coefficient for ice-ocean heat flux. A slab ocean mixed-layer model based on density criteria was used for the standalone regional implementation of the model. The model estimates of ice concentration were validated using seasonal means, and anomalies. A combined optimal interpolation and nudging scheme was implemented to assimilate Sea Surface Temperature (SST) and ice concentration from Advanced very-high-resolution radiometer (AVHRR) and Advanced Microwave Scanning Radiometer for EOS (AMSR-E) respectively. The inclusion of the variable drag coefficient required updates of ice volume and dependent tracers corresponding to the updates in the ice concentration estimates. The sea ice variables of thickness, freeboard, level ice draft and keel depth were compared with the estimates derived from Soil Moisture and Ocean Salinity (SMOS), CryoSat2, and a ULS instrument respectively. The assimilated model provided better estimates of ice concentration, thickness, freeboard and level ice draft. The model estimated ice thickness compared well with the thin ice thickness estimated from the SMOS data, except during March, when there is significant ice extent. The reason for this discrepancy could be attributed to the absence of mixed layer heat flux forcing in the model and also the effect of snow and the onset of melt that alters the observation.

Field measurements were also used for the comparison of model estimates. The measurements from the Upward Looking Sonar (ULS) instrument located at Makkovick Bank were used to estimate the level ice draft and keel depth. The observations from ULS along with model estimates were used to determine the coefficient that relates the sail and keel measurements. The level ice draft showed a good match with the values extracted from the ULS data, while the sail to keel relationship coefficient seems to vary between a value of 3 during January and February and a value of 7 from March to May. Further studies have to be conducted to understand these variations.

The ice concentration estimates from the assimilated model were compared with the ice concentration estimates derived from the images that were obtained during a field survey along the Labrador coast. The results of the ice concentration derived from the images showed a good match with the model values. The results were also compared with the estimates from Canadian Ice Service (CIS) ice charts and Advanced Microwave Scanning Radiometer-Earth observation (AMSR-E).

Acknowledgements

It has been quite a journey for the last four years to complete my Ph. D. thesis work. I am delighted that finally, it is time to thank all the amazing people who have provided support and encouragement throughout this journey and made it possible for me to reach my destination.

This thesis would not have been possible without the guidance and support from my Ph.D. supervisor Dr. Igor Zakharov. I would like to express my deepest gratitude to him for his wisdom, guidance, encouragement, and patience. He was a constant source of inspiration and helped me to realize the power of critical reasoning. He provided me with an excellent atmosphere for conducting research and was always ready for discussions and friendly conversations. I am greatly indebted to him for introducing me to the fascinating field of ice-ocean modeling, data assimilation, and remote sensing.

I would like to graciously thank my Ph.D. co-supervisor Dr. Peter McGuire for his support, guidance, discussions, inspiration and mentoring. I thank the current and past members of my thesis committee, Desmond Power, Dr. Martin Richard, and Pradeep Bobby for generously giving their time to offer me valuable suggestions, comments and discussions to improve my work. I thank Thomas Puestow for his comments on my Ph.D. proposal and for connecting me with the ice modeling community.

I am greatly indebted to the co-authors of my research papers for their contribution and the anonymous reviewers for their comments, which significantly helped to improve the content and presentation of this thesis. A special note of thanks to

the CCSM, ICE model developers, and Los Alamos sea ice modeling community for making the model available and offering help towards using the models. I would also like to thank the Linux, ferret, and NCL users community and forums.

My sincere thanks to Dr. Elizabeth Simms, Dr. Mohamed Shehata, and Dr. Reza Shahidi for their support and the courses offered to us.

My heartfelt gratitude goes to Prof. A. M. Geevargese from my Alma-mater Union Christian College who supported and encouraged me as a teacher, mentor, and friend throughout my research life. I am also grateful to my Masters supervisor Dr. Ronald Haynes (Department of Mathematics at Memorial University) and my project supervisor Dr. P. N. Vinaryachandran (CAOS, Indian Institute of Science) for their guidance and mentorship. I also thank Dr. Jaison Kurian (Texas A&M University) for his support and encouragement during my research work.

Thank you to all the faculty, office staff, my classmates, project mates at C-CORE, Memorial University, Union Christian College and to my colleagues at Indian Institute of Science. I would also like to acknowledge C-CORE and all the staff members for the facilities and support they provided throughout my Ph.D.

I am grateful to the Research and Development Corporation (RDC) of Newfoundland and Labrador for the financial assistance provided through the RDC Ignite, Ocean Industries Student Research Awards and also to the School of Graduate Studies at Memorial University. My sincere gratitude to Stephen Green, Director Research, and Development at PAL Aerospace, for his interest in my work, support towards RDC OISRA application. Without this support, it would not have been possible to pursue this thesis on a full-time basis. I thank Tony King (C-CORE) and Ingrid Peterson (DFO, Government of Canada) for providing ULS data from Makkovik Bank.

I would also like to acknowledge the computational support provided by the ACENet community. Many thanks to Mitch Sturge, Associate Director, Center for Health Informatics and Analytics (CHIA) and the system administrators for giving us the permission and support to use the computational facility. Thanks to ACENet for the group meetings, discussions and for provided the access, support, and the courses for the use of computational facilities required for my research.

Lastly, but most importantly, I wish to thank my parents for their support and love. My heartfelt thanks to my brother Krishna Prasad, my relatives Reghu Neelakandan, Dr. Anu Joy and my friends Dr. Hari Varma, Dr. Neema C .P, Sunish Kumar for their encouragement, support, suggestions, and advice at every stage of my research life. They have always been a constant source of inspiration and motivation. Without their support and encouragement, it would have been impossible to achieve this thesis. And finally, I thank with love to my better half Sushama Devi, for being a great companion and helping me get through this journey by your love, support, patience, and optimism.

It has been an exciting endeavor..thank you, everyone.

Contents

List of Tables

List of Figures

List of Abbreviations

GSA	Great Salinity Anomaly
ULS	Upward Looking Sonar
PSU	Practical Salinity Unit
AVHRR	Advanced Very High-Resolution Radiometer
AMSRE	Advanced Microwave Scanning Radiometer for Earth Observation
SAR	Synthetic Aperture Radar
3D-CEMBS	3D Coupled Ecosystem Model of the Baltic Sea
ITD	Ice Thickness Distribution
EVP	Elastic Viscous Plastic
CICE	Los Alamos sea ice Model
CIOM	Coupled Ice Ocean Model
SST	Sea Surface Temperature
OSI SAF	Ocean and Sea Ice Satellite Application Facility
SMOS	Soil Moisture and Ocean Salinity
GCM	General Circulation Model
SSMI	Special Sensor Microwave Imager
3D-VAR	3 dimensional variation (scheme)
4D-VAR	4 dimensional variation (scheme)
CIS	Canadian Ice Service
SSMR	Special Scanning Multichannel Microwave Radiometer
SSMIS	Special Sensor Microwave Imager/Sounder

AMSR2 Advanced Microwave Scanning Radiometer 2

CFSR Climate Forecast System Reanalysis

WOA World Ocean Atlas

NARR North American Regional Reanalysis

MLD Mixed Layer Depth

RMSE Root Mean Square Error

...

Nomenclature

a	Model estimated ice concentration
f_{sen}	Sensible heat flux
f_{lat}	Latent heat flux between the atmosphere and the open-ocean surface
f_{lwout}	Black body heat flux from the open-ocean surface to the atmosphere
f_{lwin}	Downward long-wave radiative heat flux
f_{swabs}	Downward short-wave radiative heat flux
f_{ice}	Heat flux from the ocean surface to the base of the ice
f_{swthru}	Short wave radiative heat flux that passes through the ice and is absorbed by the ocean
Q_{mix}	Mixed-layer heat flux
c_ρ	Product of specific heat of ocean and density of sea water
T	SST

T_f	Freezing temperature
S	Salinity
h_{mix}	MLD
$frzmlt$	Potential to freeze or melt ice
μ	Ratio of freezing temperature of brine to its salinity
σ_θ	Potential density
ρ	Density of snow or ice
q	Enthalpy of snow or ice
h	Ice thickness
K_i	Conductivity of ice
S_i	Internal ice salinity
T_i	Internal ice temperature
ρ_i	Density of ice
ρ_s	Density of snow
f_{cb}	Conductive heat flux at the bottom surface
f_b	The net downward heat flux from ice to the ocean
D_w	Variable ice-ocean drag
u^*	Friction velocity
a_n	Ice area fraction in category n
v_{in}	Ice volume in category n
v_{sn}	Snow volume in category n

u	Ice velocity
$a_{lvl}a_n$	Level ice fraction
$a_{pnd}a_{lvl}a_n$	Pond ice fraction
$h_{pnd}a_{pnd}a_{lvl}a_n$	pond volume
$h_{ipnd}a_{pnd}a_{lvl}a_n$	pond ice volume
$p(h)$	Function that describes the thickness distribution of ice participating in ridging
$n(h)$	Function that describes the thickness distribution of ridged ice
ψ	Ridging function
$b(h)$	Weighing function used in ridging scheme
P	Ice strength
τ_w	ocean stress
τ_a	wind stress
X_a	Analysis of ice concentration/SST
X_o	Observation of ice concentration/SST
X_b	Background state of ice concentration/SST
K	Nudging coefficient
σ_o	Standard deviation of Observation
α	Parameter in data assimilation

τ Basic time scale used in data assmilation

M0 Non-assimilated model

M1 Model assimilated with ice concentration

M2 Model assimilated with ice concentration and SST

Chapter 1

Introduction

1.1 Importance of sea ice information

Monitoring and understanding the dynamics and the formation/melting of sea ice are critical for regional and global climate studies, navigational, marine and industrial applications.

During winter, cooling increases the ice cover extent in the polar regions. The surface of the ice has increased albedo, which results in minimal absorption of solar energy and leads to more cooling [5, 21]. During summer, the warm temperatures melt the snow and ice creating melt ponds. The melt ponds have reduced albedo causing more absorption of solar energy thus initiating more melt and a warmer climate. This cycle of events where slight cooling causes more cooling and slight warming causes more warming is known as ice-albedo feedback [5, 21]. The increased greenhouse gas emissions result in a warmer climate which leads to earlier sea ice melt and delayed ice formation. Thus ice-albedo feedback plays a vital role in climate change [5].

As sea ice forms, it rejects salt into the ocean water and also accumulates salt into droplets called brine that get trapped in small pockets of ice crystals. The rejection of salt during the sea ice formation produces cold saline water below the ice which is denser than the surrounding water column [22, 29]. The cold dense water that forms at the surface of the ocean near the Arctic sinks toward the North Atlantic Deep water ocean bottom, and surface water moves in to replace the sinking water thus creating currents. This deep water flows towards the south and moves around the edge of Antarctica, where the water cools and sinks again, as it does in the North Atlantic. The current is then split off into two sections. One section moves towards the Indian Ocean and the other towards the Pacific Ocean. The parts of the current that split off warm up and becomes less dense as they travel northward towards the equator, so that they rise to the surface. The currents then loop back, southward and westward to the South Atlantic, eventually returning to the North Atlantic, where the cycle repeats. This flow pattern is known as the oceans global conveyor belt circulation or thermohaline circulation. The formation and ablation of sea ice can thus contribute towards changes in the conveyer-belt circulation, which controls the heat distribution over the globe and thus results in global climate change [40]. Therefore the presence of sea ice may affect the movement of ocean water and the global heat transport.

Studies by Zhang and Vallis [40] showed that the Great Salinity Anomaly (GSA) event, caused by the melting of sea ice in the late 1960s, led to the warming of the U.S. East Coast and the cooling of Europe. Moreover, the GSA event affected the fish population in the Labrador Sea [20]. During GSA events low-salinity water propagates into North Atlantic waters and reduce the deep water formation in the region. Previous modeling studies have shown that GSA events could also affect thermohaline

circulation, the deep Western Boundary Current, the Northern Recirculation Gyre and the Gulf Stream [6, 9, 37]. The weakening of thermohaline circulation would force the atmosphere to transport heat leading to an increase in storm activities [40].

Reduction of sea ice increases the open-water area, and the escalation of waves due to the storm increases shoreline erosion and flooding. For instance, the melting of ice in the Chukchi Sea on the coastal areas of the village of Shishmaref, Alaska, led to massive waves that eroded the shoreline [2].

Sea ice and the freshwater that forms due to the melting of sea ice float on the surface of the saline ocean water as a thin layer, preventing the interaction between air and ocean. Such a thin layer of fresh water affects the growth of phytoplankton that controls the aquatic food chain and the carbon cycle in the ocean. Phytoplankton consumes carbon dioxide and carries it to the deep ocean maintaining the carbon cycle. The reduced interaction between air and ocean will lead to the increased presence of carbon dioxide in the atmosphere thereby triggering global climate disruption. There has been evidence of massive phytoplankton bloom beneath sea ice where light transmission has increased because of thinning ice cover and proliferation of melt ponds [3].

The formation of polynyas, an area of open water surrounded by sea ice, are beneficial to some marine species. For instance, the North Water polynya in the Baffin Bay provides a warm environment used as shelter by marine animals [32]. Studies on the formation of such polynyas could be helpful to track the movement of aquatic life forms.

Winds and currents may push ice floes against each other resulting in a line or wall of broken ice forced up by pressure known as ridges which pose a threat to marine

navigation through ice frequented regions. On the other hand, the formation of leads, open water areas within a vast expanse of sea ice, provide safer transportation through ice frequented areas [29].

The recent reduction of ice extent in the Arctic region has resulted in the exploration of new navigational routes and exploitation of non-renewable resources in the area. Costly equipment and safety mechanisms are required to work in the harsh environments of the Arctic. Reliable and timely information on ice concentration, thickness and strength, movement and ice types would improve efficiency and safety of navigation through ice rich waters. Such information would be of great value in the estimation of ice stresses and forces for the construction of offshore stations [29].

Information on sea ice conditions provides critical inputs for logistics and contributes to the safety of offshore stations. For instance, a 30-mile long ice floe which suddenly changed its direction due to high winds forced Shell to shut down its drilling rig and to disconnect it from the Burger-A well in the Chukchi Sea [1].

1.2 Background

1.2.1 Physics of the sea ice processes

The ocean surface mixed layer is where the temperature, salinity and, therefore, density remain homogeneous. The surface mixed layer plays a vital role in heat and freshwater transfer between atmosphere and ocean. The homogeneity in the layer is caused by the turbulence generated by winds, surface heat fluxes, processes such as evaporation or sea ice formation. The layer usually occupies the uppermost $10-100$ m

but may reach much deeper during winter. In regions of sea ice formation, the resulting rise in salinity also increases the density. When the surface water becomes denser than the underlying water, a convective overturning occurs, and the dense surface water mixes downwards. During a cooling cycle, the convective overturning releases the heat stored in the ocean to the atmosphere and seeps to a depth determined by salinity and temperature-controlled density of cooled water. The overturning is continuous until the layer reaches the freezing point (determined by the salinity) at which point sea ice forms. Since brine rejection occurs during sea ice formation, the salinity beneath the ice increases and the convective overturning continues. The continuing overturn requires a large volume of water to be cooled to a freezing temperature, depending on the salinity increase before the additional ice forms. Once the ice begins to grow, it acts as an insulator between ocean and atmosphere and slows down the heat transfer thus slowing down the ice growth. As the ice thickens, it takes longer for the water below the ice to reach the freezing point. Also, the poor thermal conductivity of snow on the top of ice slows down the heat flux from the ice-water interface to the atmosphere through the ice volume further slowing down the ice growth. The surface ablation caused by sublimation or surface melt may also slow down the ice growth [29, 26].

The process of salt rejection during the formation of sea ice can be categorized into one rapid, and one slow process. The rapid process occurs at the ice-water interface as soon as the seawater freezes while rejecting the impurities. The rapid process is active only during the initial phase of the formation of sea ice. As sea ice forms, some of the liquid salt accumulations gets trapped between ice crystals. Along with brine, air bubbles and biogeochemical matter also gets trapped in the crystals. The trapped

brine and air bubbles change the physical and dielectric properties of sea ice. As freezing advances, the slow process of salt rejection leads to brine drainage from the bulk of the ice sheet. The brine inclusions surrounded by ice will require much cooler temperatures to freeze. There are various mechanisms by which the brine escapes into the ocean: brine pocket migration, brine expulsion, gravity drainage and brine flushing. Brine pocket migration depends on the principle that the liquid inclusions of salt migrate towards the warmer end of the ice sheet. Brine pocket migration through the ice sheet is caused by the temperature gradient. In winter, the ice sheet is colder at the top and warmer at the bottom, thus draining brine. Consequently, the solute diffuses from the upper to the lower end resulting in simultaneous freezing at the upper end of the pockets and melting at the lower ends. The process is reversed during spring when ice temperature becomes warmer at the top of the ice sheet. Brine expulsion occurs due to further cooling of the ice sheet and thermal expansion. As the cooling continues the bulk ice temperature decreases and, thus, the volume of brine pockets decrease due to further solidification of water inside the brine pockets. The solidification induces pressure and results in the cracking of brine channels migrating the brine. The gravity drainage occurs due to the density differences between brine in the interior of the ice and the surrounding seawater salinity. The greater weight of the brine relative to that of the seawater tends to drive the brine out of the ice-water interface. The fourth mechanism of brine drainage, known as flushing, occurs during the melt season when melt ponds form and drain through the pores and cracks in sea ice, flushing the remaining brine into the ocean. As sea ice ages or thickens, sea ice salinity decreases due to brine rejection [10, 29].

Geophysical forces such as winds, ocean currents, Coriolis force, sea surface tilt,

and tides contribute to sea ice motion [26]. Different types of ice deformation may occur when ice floes are pushed around and interact with each other. Rafting and pressure ridging are the most common results of ice deformation and occur when two ice sheets are pushed against each other. Shear ridges may form when ice floes move laterally against each other. If the sheets are thin, rafting is more likely to occur, and if they are thick, a pressure ridge will form [29]. Moreover, rafting and ridging contribute to the increase of ice thickness. Leads are another type of deformation caused by ice divergence. They are wide openings or fractures within in an expanse of sea ice and provide navigational routes to marine vessels. Ridges, on the other hand, represent a hazardous condition for navigation through ice frequented regions. Leads enhance the heat exchange between the ocean and atmosphere [29, 33].The study of ice deformation is important since it influences to the ice thickness, concentration, and climate variability.

1.2.2 Observation of sea ice

Satellite observation generates images of the surface of the earth. The images are captured using sensors that can detect electromagnetic radiation scattered from the object or the earths surface. The images obtained are then analyzed to derive relevant information about the area or the objects. There are tradeoffs when using various ranges of the electromagnetic spectrum for sea ice surveillance, e.g., the information from visible spectra can be obtained only during the daytime. Clouds and other particles in the atmosphere scatter the visible radiation which results in loss of information, however, cloud-free images are used to identify and map sea ice. In-

frared radiation, which can detect temperature differences, are also used to capture sea ice information, e.g., Advanced Very High-Resolution Radiometer (AVHRR) uses the $1.58 - 1.64$ μm (Mid-infrared) band for snow and ice detection.

Radiation in the microwave spectra can penetrate clouds and are used to derive sea ice information. Moreover, the microwave spectrum can be used during day and night. The instruments in the microwave spectra fall into two categories - passive and active. Passive microwave instruments use the natural radiation emitted from the earth's surface and process the information to derive sea ice related variables, e.g., Advanced Microwave Scanning Radiometer for Earth Observation (AMSR-E) is used to obtain ice concentration. The drawback of passive microwave sensors is that it is hard to detect small details such as leads due to low energy emitted. Active microwave instruments emit radiation towards the earth's surface and use reflected radiation to derive sea ice information. Various types of active microwave sensors are used for the detection of sea ice features. Imaging radars like Synthetic Aperture Radar (SAR) detect information on leads; non-imaging radar or Scatterometers detect the presence of ice, but provide less information than SAR; altimeters which are used to measure the altitude of features on the earth's surface are used to derive freeboard and ice thickness, e.g., CryoSat-2.

Though we use the instruments mentioned above to derive information on sea ice, the reflected energy depends on the physical properties of sea ice which is quite complex. In certain cases, it becomes practically difficult to extract the required information on sea ice parameters. Sea ice is a heterogeneous mixture; the dielectric properties can vary with the presence of ice crystals, liquid brine, and air bubbles present inside the structure, which affect its signature in microwave images [10].

Furthermore, the presence of snow renders the penetration of ice by microwave signals further difficult. Snow is fairly transparent to microwave wavelengths except when the snow is wet, or there are several layers of snow separated by thin ice [27].

The data derived from satellites or aircraft may have data gaps since the information retrieved depends on the revisit time of the satellite or flight routes. Also, as mentioned above, the data derived using remote sensing method also depends on the penetration level of microwave spectrum, the ice type, snow cover or atmospheric conditions, e.g., AMSR-E ice concentrations have an error of about 10% for ice concentration above 65%, the estimates of error for ice concentration less than 65% depends on various atmospheric conditions [31]. The ice thickness estimates derived from SMOS-MIRAS has an uncertainty of about 100% for ice thickness greater than 50 cm [17].

1.2.3 Mathematical modeling of sea ice processes

To retrieve sea ice parameters such as ice concentration, thickness and to understand the physical process of the formation and ablation of ice, the future ice conditions, or to predict climate scenarios, scientists use mathematical models that represent the atmosphere-ocean interactions and properties of sea ice. Such models can be utilized to aid operational services for navigation and long-term planning, and for the development of an operational ice dynamics model for ice service [28]. The models, coupled with ecosystem models are used for obtaining approximations of the environmental process; e.g., 3D Coupled Ecosystem Model of the Baltic Sea (3D-CEMBS), Marine ecosystem model designed for the Baltic Sea [7].

Four governing equations are used to model the sea ice process. The first of these is the Ice Thickness Distribution (ITD) equation that describes the probability that the ice cover in a particular region has CISied thickness. The ITD equation considers the ice that participates in redistribution or the deformation, and advection in thickness space [34]. Most importantly, the characteristics of growth, melting and deformation vary for different ice thicknesses [14]. The second equation covers the conservation of momentum which takes into account the effects of Coriolis force, air water stress, the force due to ocean surface tilt and internal ice force. The stress-strain rates also depend on the consideration of the rheology Viscous Plastic rheology [12] or Elastic Viscous Plastic (EVP) rehology [13], or Elastic Anisotropic Viscous Plastic rheology [39, 38]. The third equation involves the conservation of enthalpy which considers the energy required to melt the sea ice. The last of these is the heat equation for ice and snow which considers the thermal energy change in layers of ice, conductive flux and absorption of solar radiation [4]. Chapter 3, section 3.4 discusses in detail the equations used to represent the atmospheric-ice-ocean process.

As mentioned earlier, the processes that describe the evolution of sea ice are complex, and hence only mathematical approximations can be made [15]. Such approximations carry assumptions that produce inherent uncertainties. Model accuracy will depend on the model physics and the boundary conditions of atmospheric and oceanic forcing that are used to derive sea ice parameters. In long-term simulations, the solutions of such models may deviate from observed values. In such cases, data assimilation methods are used to bring the initial model conditions close to the observation [18, 28].

1.3 Motivation

Many ice models are used coupled with the ocean model on the regional and global scale implementations. These models were validated for estimated ice concentration, thickness and drift parameters. These models also demonstrate some drawbacks either due to the physical parameterizations or due to the poor quality of the boundary forcing used to estimate the parameters. NEMO-LIM3 reports an overestimation of ice thickness in the Southern Ocean [35]. The LIM 3 ice concentration estimates have been validated with the estimates from Scanning Multichannel Microwave Radiometer (SMMR) and the Special Sensor Microwave/Imager (SSM/I). The mean absolute error of ice concentration between LIM3 model and Sea Ice Satellite Application Facility (OSI SAF) showed an error of 79% in the Northern Hemisphere [19]. The mean absolute error of ice draft compared with the draft from Upward Looking Sonar (ULS) measures showed an error of 67cm in the Northern Hemisphere [19]. For the MITgcm with 32 km resolution, used to study the interannual variability of sea ice in the Labrador Sea and the Baffin Bay, the spatially and temporally varying sea ice concentration uncertainties ranged from 8.5% to 18% [8]. The results of ice thickness estimates from 'Estimating the Circulation and Climate of the Ocean, Phase II' (ECCO2) model, which is based on MITgcm, was compared with thickness derived from satellites. The study reported that ECCO2 model overestimates satellite-derived thickness when less than 2.0 m and underestimates the thickest ice by 2 or more meters [16]. The study also compares several other models: Goddard Space Flight Center (GSFC), Institute of Numerical Mathematics Ocean Model (INMOM) Russian Academy of Science, the Naval Postgraduate School Arctic Modeling Effort (NAME),

the National Oceanography Centre Southampton (ORCA), and the PIOMAS of the University of Washington UW model). Almost all the models overestimated thickness of ice thinner by 2 m.

ROMS [11] was used for modeling studies of Storfjorden polynyas using one-way nesting where a coarse-resolution model was used to provide boundary conditions for a high-resolution (2 km) model. The model was partially validated using field and satellite data and performed well in reproducing the ice extent [30]. In another study, Ocean and OSI SAF data for ice concentration were assimilated into ROMS for simulating sea ice concentrations and produced better results than the simulation without assimilated OSI SAF data. Ice concentration and extent were overestimated, possibly due to the bias in atmospheric forcing and underestimation of heat flux and over/underestimation of sea ice growth/melt processes [36]. Also, the model estimates on the ice thickness or other parameters such as freeboard, draft were rarely discussed. The CICE [15] model was also used to study the parameters but were mostly implemented on a global scale or in regional scale with closed boundaries. The grid system that was used for the discretization of the model equations on regional configurations were also ambiguous [7].

The observation of sea ice conditions requires several parameters, some of which can be easily and accurately determined using satellite measurements, but still, data gaps exist within the information. With the availability of high-resolution reanalysis data, models with advanced physics and algorithms and data assimilation/fusion techniques can be used in combination with remote sensing and modeling methods to determine most of the sea ice parameters. Moreover, sea ice processes are mostly studied using data assimilated or non-assimilated coupled global models and are rarely

discussed in regional implementation, as most discussions are confined only to the estimated ice concentration.

Since mixed layer properties drive sea ice processes using a coupled vertical high resolution, an ocean model would require significant data analysis resources for tuning ocean parameters and also additional computational requirements. In this thesis, we explore the ways to implement, develop and parameterize sea ice physics using an uncoupled/standalone sea ice model that derives its forcing boundary conditions from already available high-resolution atmospheric and ocean data sets.

1.4 Research objective(s) and Methodology

The primary purpose of this research was to combine the information from remote sensing data and a regionally implemented high-resolution sea ice model to retrieve the sea ice parameters in the region of Baffin Bay and Labrador Sea, see Figure 1.1. The primary objective was broken down into a number of functional objectives. The first of these was to implement an advanced sea ice model for the region of interest. See Section 2.4 for a review of some sea ice models that were available. The region of interest was identified on the basis of the importance of application relevant to the province of Newfoundland and Labrador and Canada. The model may be implemented in other polar regions but may require a substantial changes in the configuration. Many industrial firms have plans to set up their stations in the offshore areas of the province, and this research serves as a method to derive the sea ice parameters in the region for risk/logistic analysis. The second objective was to include data assimilation methods to reduce inherent uncertainties within the model.

The third objective was to derive sea ice parameters and validate it with remote sensing data. The final objective was to derive information based on the assimilation of remote sensing data with the model results.

1.5 Thesis writing

The thesis follows the publication-oriented style/manuscript-based thesis format. The research papers chosen for this dissertation are summarized in Section 1.6. The complete list of references used in the thesis is listed as an additional Bibliography at the end of Chapter 6.

1.5.1 Publications

The contributions/findings from this research have been published in the following articles.

Journal Papers

1. Prasad, S. Zakharov, I., McGuire P., Power, D., Martin, R., 2018. Estimation of sea ice parameters from sea ice model with assimilated ice concentration and SST, Cryosphere *(submitted)*

2. Prasad, S., Zakharov, I., Bobby, P., 2016.Model-Based Estimation of Sea Ice Characteristics in the Region of Baffin Bay and the Labrador Sea, Journal of Ocean Technology 11(1), 39–47.

3. Prasad, S., Zakharov, I., Bobby, P., McGuire, P., 2015. The implementation of

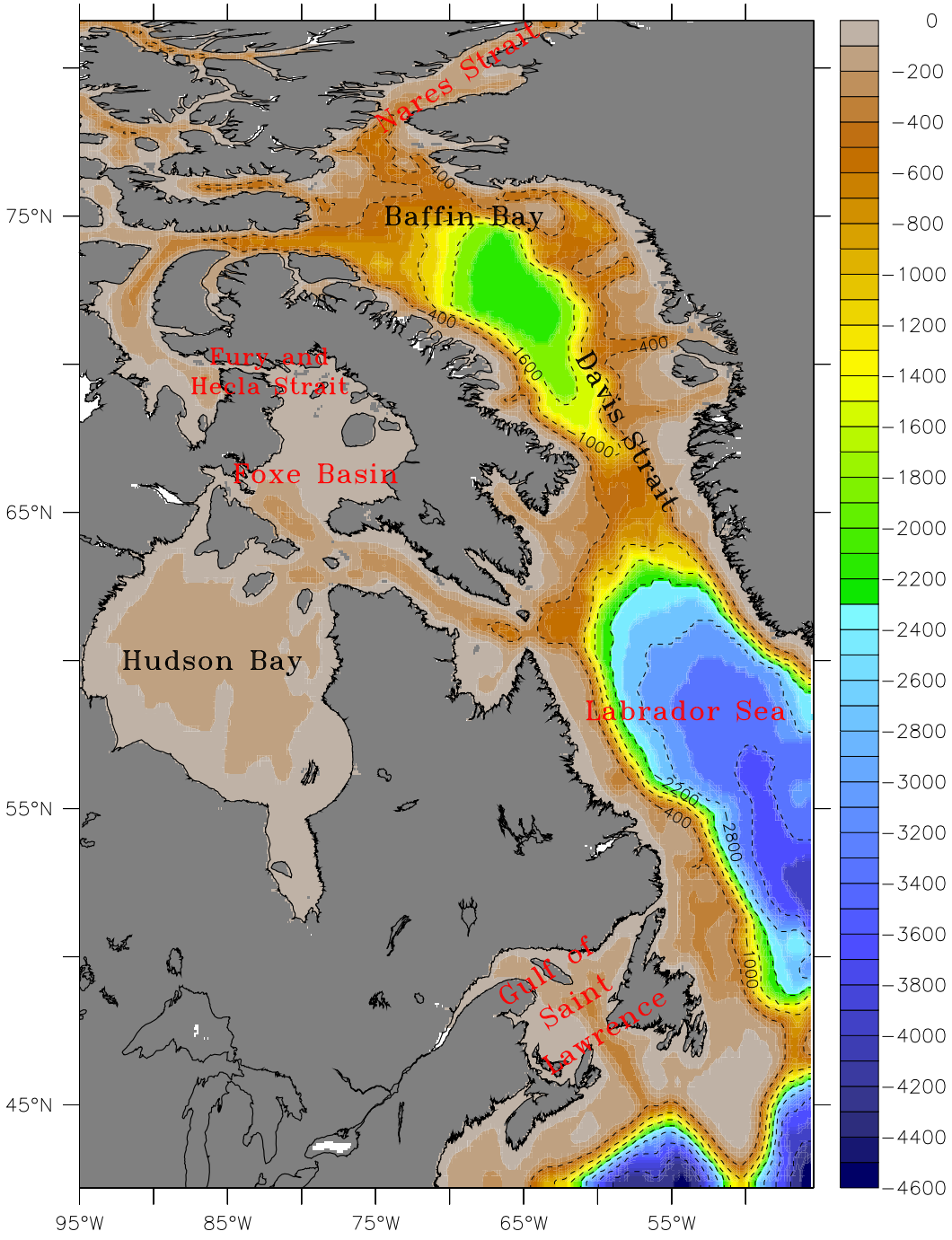

Figure 1.1: Region of interest.

sea ice model on a regional high-resolution scale. Ocean Dynamics 65, 1353–1366.

Conferences

1. Prasad S., Zakharov I., McGuire P., 2016. High-resolution sea ice modeling for the region of Baffin Bay and the Labrador Sea. AGU Fall Meeting, 12-16 December. San Francisco, USA.

2. Prasad S., Zakharov I., Bobby P., McGuire P., Power D., 2016. Model-based estimation of sea ice parameters. Arctic Technology Conference (ATC) 24-26 October. St. Johns, NL, Canada.

3. Prasad S., Zakharov I., Bobby P., McGuire P., Data assimilated sea ice model for the Baffin Bay and Labrador region, 18th May 2016, Association of Polar Early Career Scientists (APECS) online conference.

4. Prasad S., Zakharov I., Bobby P. and McGuire P., Analysis of sea ice conditions based on model and Remote Sensing Data, Ocean Innovation, 26th October-28th October 2015, St. John's, NL (Best Poster Award).

5. Prasad S., Zakharov I., Bobby P. and McGuire P. Inter-comparison of sea ice freeboard, thickness, and ice concentration extracted from sea ice model with satellite data. 36th Canadian Symposium on Remote Sensing, 8th June - 11th June 2015, St. John's, NL, Canada.

6. Prasad S., Zakharov I. The implementation of sea ice model on a high-resolution regional scale, 6th International Workshop on Modeling the Ocean, 23rd June - 27th June, 2014, Halifax, NS, Canada.

7. Zakharov I., Power D., Prasad S., 2016. Measurement of sea ice and icebergs Topography using satellite imagery. AGU Fall Meeting, 12-16 December. San Francisco, USA.

8. Zakharov I., Prasad S., Bobby P., Power D., Walsh D., Warren S., Puestow T., 2016. Monitoring of Sea Ice-Covered Areas for Ship Navigation. In Living Planet Symposium 2016. Prague, Czech Republic: ESA. 9-13 May 2016.

9. Zakharov I., Prasad S., Steven Q. and Bobby P. Extracting sea ice geophysical parameters from multi-source data (24135), AGU Fall Meeting, 14th December - 18th December 2014, San Francisco.

Other Presentations

1. Discussion on the implementation of data assimilated regional high-resolution sea ice Model, New York University, Abu Dhabi Nov 17, 2016

2. Project presentation on retrieval of sea ice parameter using high-resolution sea ice model, Canadian Ice Service - Jun 21, 2016

3. Retrieval of sea ice parameters that are useful for offshore resources in risk analysis using numerical modeling techniques, Statoil, June 18, 2015

1.6 Organization of the dissertation

The remaining part of the thesis is organized as follows

Chapter 2: Literature Review. The chapter presents the work that has been done in the area of remote sensing of sea ice, sea ice modeling and data assimilation.

The chapter also reviews the work on grid generation methods that were used for ice-ocean models in the global and regional framework.

Chapter 3: Implementation of a Sea Ice Model on a Regional High-Resolution Scale. The chapter describes the implementation of the Los Alamos sea ice model (CICE) on a regional level at a high resolution. The boundary forcing comes from various sources of data. The sea ice simulation was performed over Baffin Bay and the Labrador Sea to retrieve relevant parameters such as ice concentration, thickness, ridging, and drift. Sea ice behavior over eleven years were simulated. Validation of the model was based on the comparison of model results with remote sensing data. The previous global and regional modeling framework like 3D-CEMBS used closed boundaries and also a rotated grid coordinate system to implement the global/regional framework. The rotated grid coordinate system is useful when studying the Central Arctic region where the poles are located. In this work, the regional model was implemented on a non-rotated orthogonal curvilinear grid, and the open boundaries were introduced by restoring the values at the boundaries to the initial/restart conditions as suggested by Hunke et al. (2013). The chapter discusses the work that was published in the Journal of Ocean Dynamics by Prasad et al. (2015) [24]. The work was also presented at IWMO conference (2014) and Canadian Symposium on Remote Sensing.

Chapter 4: Estimation of sea ice characteristics in the region of Baffin Bay Labrador Sea using a high-resolution model with the assimilation of ice concentration and SST.

This chapter describes the addition of a data assimilation scheme into the model to estimate sea ice parameters with better accuracy. The data assimilation techniques

were applied to correct SST that was estimated by the slab ocean mixed layer model and also the ice concentration estimated by the model. The model results (SST) were compared with the remote sensing data derived from OSI SAF, SMOS, and CryoSat2. The chapter is based on the article by Prasad et al. (2016) [23]. The earlier modeling framework introduces the assimilation of SST in the ocean model and passes on the information to the coupled ice model. Here, in this work, the details on directly assimilating the information to reduce the error within the ice model are discussed. Along with the discussion of assimilated SST and ice concentration we also explore the impacts of the same on other parameters such as ice thickness and freeboard measures.

Chapter 5: Model comparison with in-situ measurements. This chapter describes the estimation of level ice draft and the coefficient that relates the sail height and keel depth. The model estimates were compared with the data derived from ULS measurements located in the Makkovik Bank. Also, the model-estimated ice concentration was compared with videos/images acquired during a field campaign. Unlike the previous studies were the draft estimate were directly compared with the ULS measurements. ULS data were used to extract the draft for level and deformed ice. The level ice draft measurement derived from ULS were compared with the level ice draft estimated from the model. The deformed ice draft from ULS was compared with the keel depth estimated by the model. The chapter is a part of work that was published and presented at the Arctic Technology Conference (ATC) [25] and at AGU Fall Meeting 2016.

Chapter 6: Summary. This is a concluding chapter summarizing the work from this research. Also, suggestions for future work have been provided.

1.7 Co-authorship statement

Mr. Siva Prasad (thesis author) is the main author of all papers pertaining to this research work including those presented in Chapters 3 to 5. Other co-authors are: Dr. Igor Zakharov (thesis supervisor), Dr. Peter McGuire (co-supervisor), Mr. Desmond Power (Vice President of the Department of Remote Sensing at C-CORE), Dr. Martin Richard (Senior Research Engineer at National Research Council Canada) and Mr. Pradeep Bobby (former Director of Earth Observation with C-CORE). Dr. Zakharov is a Senior Remote Sensing Scientist with C-CORE. Dr. McGuire is a Senior Project Engineer with C-CORE. He is also cross-appointed with the Faculty of Engineering and Applied Science at the Memorial University of Newfoundland. Dr. Richard is also Adjunct Professor at the Memorial University of Newfoundland. The candidate was responsible for the conception and development of the ideas contained in each research paper. Programming for the techniques developed, and data analysis were performed by the candidate, as were all duties associated with the preparation of each manuscript. Dr. Zakharov, Dr. McGuire, Mr. Power, Dr. Richard and Mr. Bobby critically reviewed the research manuscripts and suggested revisions.

Bibliography

[1] *The Los Angeles Times September*. 2012.

[2] T. Afifi and J. Jäger. *Environment, forced migration and social vulnerability*. Springer, 2010.

[3] K. R. Arrigo, D. K. Perovich, R. S. Pickart, Z. W. Brown, G. L. Van Dijken, K. E. Lowry, M. M. Mills, M. A. Palmer, W. M. Balch, F. Bahr, et al. Massive phytoplankton blooms under Arctic sea ice. *Science*, 336(6087):1408–1408, 2012.

[4] C. M. Bitz. Numerical modeling of sea ice in the climate system, 2008.

[5] J. A. Curry, J. L. Schramm, and E. E. Ebert. Sea ice-albedo climate feedback mechanism. *Journal of Climate*, 8(2):240–247, 1995.

[6] T. L. Delworth and M. E. Mann. Observed and simulated multidecadal variability in the northern hemisphere. *Climate Dynamics*, 16(9):661–676, 2000.

[7] L. Dzierzbicka-Glowacka, M. Janecki, A. Nowicki, and J. Jakacki. A new marine ecosystem 3D CEMBS model (version 2) for the Baltic Sea. In *Complex Systems (ICCS), 2012 International Conference on*, pages 1–6. IEEE, 2012.

[8] I. Fenty and P. Heimbach. Coupled sea ice–ocean-state estimation in the Labrador Sea and Baffin Bay. *Journal of Physical Oceanography*, 43(5):884–904, 2013.

[9] S. Häkkinen. An arctic source for the great salinity anomaly: A simulation of the arctic ice-ocean system for 1955–1975. *Journal of Geophysical Research: Oceans*, 98(C9):16397–16410, 1993.

[10] M. Hallikainen and D. P. Winebrenner. The physical basis for sea ice remote sensing. *Microwave Remote Sensing of Sea ice*, pages 29–46, 1992.

[11] K. S. Hedström. *Technical manual for a coupled sea-ice/ocean circulation model (version 3)*. Citeseer, 2009.

[12] W. Hibler III. A dynamic thermodynamic sea ice model. *Journal of Physical Oceanography*, 9(4):815–846, 1979.

[13] E. Hunke and J. Dukowicz. An elastic–viscous–plastic model for sea ice dynamics. *Journal of Physical Oceanography*, 27(9):1849–1867, 1997.

[14] E. C. Hunke, W. H. Lipscomb, and A. K. Turner. Sea-ice models for climate study: retrospective and new directions. *Journal of Glaciology*, 56(200):1162–1172, 2010.

[15] E. C. Hunke, W. H. Lipscomb, A. K. Turner, N. Jeffery, and S. Elliott. CICE: the Los Alamos Sea Ice Model Documentation and Software Users Manual Version 5.1 LA-CC-06-012. *T-3 Fluid Dynamics Group, Los Alamos National Laboratory*, 675, 2015.

[16] M. Johnson, A. Proshutinsky, Y. Aksenov, A. T. Nguyen, R. Lindsay, C. Haas, J. Zhang, N. Diansky, R. Kwok, W. Maslowski, et al. Evaluation of Arctic sea ice thickness simulated by Arctic Ocean Model Intercomparison Project models. *Journal of Geophysical Research: Oceans*, 117(C8), 2012.

[17] L. Kaleschke, X. Tian-Kunze, N. Maaß, G. Heygster, M. Huntemann, H. Wang, and C. Haas. SMOS Sea Ice Retrieval Study (SMOSIce), ESA Support To Science Element (STSE), Final Report ESA ESTEC contract no. Technical report, 4000101476/10/NL/CT, 2013.

[18] Lindsay, RW and Zhang, J. Assimilation of ice concentration in an ice–ocean model. *Journal of Atmospheric and Oceanic Technology*, 23(5):742–749, 2006.

[19] F. Massonnet, T. Fichefet, H. Goosse, M. Vancoppenolle, P. Mathiot, and C. K. Beatty. On the influence of model physics on simulations of Arctic and Antarctic sea ice. *Cryosphere*, 5(3):687, 2011.

[20] G. Mertz and R. Myers. The ecological impact of the Great Salinity Anomaly in the northern North-west Atlantic. *Fisheries Oceanography*, 3(1):1–14, 1994.

[21] NSIDC. "All About Sea Ice." National Snow and Ice Data Center. `https://nsidc.org/cryosphere/seaice/index.html`. Accessed: 2013-10-15.

[22] G. L. Pickard and W. J. Emery. *Descriptive physical oceanography: an introduction*. Elsevier, 2016.

[23] S. Prasad, I. Zakharov, and P. Bobby. Model Based Estimation of Sea Ice Characteristics in the Region of Baffin Bay and the Labrador Sea. *Journal of Ocean Technology*, 11(1):39–47, 2016.

[24] S. Prasad, I. Zakharov, P. Bobby, and P. McGuire. The implementation of sea ice model on a regional high-resolution scale. *Ocean Dynamics*, 65(9-10):1353–1366, 2015.

[25] S. Prasad, I. Zakharov, P. Bobby, D. Power, P. McGuire, et al. Model Based Estimation of Sea Ice Parameters. In *Arctic Technology Conference*. Offshore Technology Conference, 2016.

[26] J. P. Rafferty et al. *Oceans and oceanography*. Britannica Educational Publishing, 2010.

[27] S. Sandven, O. M. Johannessen, and K. Kloster. Sea ice monitoring by remote sensing. *Encyclopedia of Analytical Chemistry*, 2006.

[28] M. Sayed, T. Carrieres, H. Tran, S. B. Savage, et al. Development of an operational ice dynamics model for the Canadian Ice Service. In *The Twelfth International Offshore and Polar Engineering Conference*. International Society of Offshore and Polar Engineers, 2002.

[29] M. Shokr and N. Sinha. *Sea ice: physics and remote sensing*. John Wiley & Sons, 2015.

[30] L. H. Smedsrud, W. P. Budgell, A. D. Jenkins, et al. Fine-scale sea-ice modelling of the Storfjorden polynya, Svalbard. *Annals of Glaciology*, 44(1):73–79, 2006.

[31] G. Spreen, L. Kaleschke, and G. Heygster. Sea ice remote sensing using AMSR-E 89-GHz channels. *Journal of Geophysical Research: Oceans*, 113(C2), 2008.

[32] I. Stirling. The biological importance of polynyas in the Canadian Arctic. *Arctic*, pages 303–315, 1980.

[33] D. N. Thomas. *Sea ice*. John Wiley & Sons, 2017.

[34] A. Thorndike, D. Rothrock, G. Maykut, and R. Colony. The thickness distribution of sea ice. *Journal of Geophysical Research*, 80(33):4501–4513, 1975.

[35] M. Vancoppenolle, S. Bouillon, T. Fichefet, H. Goosse, O. Lecomte, M. Morales Maqueda, and G. Madec. The Louvain-la-Neuve sea ice model. *Notes du pole de modélisation, Institut Pierre-Simon Laplace (IPSL), Paris, France*, (31), 2012.

[36] K. Wang, J. Debernard, A. K. Sperrevik, P. E. Isachsen, and T. Lavergne. A combined optimal interpolation and nudging scheme to assimilate OSISAF sea-ice concentration into ROMS. *Annals of Glaciology*, 54(62):8–12, 2013.

[37] A. J. Weaver, J. Marotzke, P. F. Cummins, and E. Sarachik. Stability and variability of the thermohaline circulation. *Journal of Physical Oceanography*, 23(1):39–60, 1993.

[38] J. Weiss and E. M. Schulson. Coulombic faulting from the grain scale to the geophysical scale: lessons from ice. *Journal of Physics D: Applied Physics*, 42(21):214017, 2009.

[39] A. V. Wilchinsky and D. L. Feltham. Modelling the rheology of sea ice as a collection of diamond-shaped floes. *Journal of Non-newtonian Fluid Mechanics*, 138(1):22–32, 2006.

[40] R. Zhang and G. K. Vallis. Impact of great salinity anomalies on the low-frequency variability of the North Atlantic climate. *Journal of Climate*, 19(3):470–482, 2006.

Chapter 2

Literature Review

2.1 Overview

This chapter highlights significant contributions to sea ice modeling. First, an introduction to remote sensing of sea ice is provided followed by a detailed discussion on sea ice modeling and assimilation methods. Lastly, the chapter reviews grid generation methods used in the ice-ocean models.

2.2 Remote sensing of sea ice

Sea ice monitoring is done primarily using satellites. To fill temporal and spatial data gaps the monitoring community also depends on measurements from airborne data, ships, submarines, and instruments such as ULS.

The first remote observations of sea ice were made from air balloons in 1897 [42] but were found to be unsuitable for deriving information on ice conditions. Since the development of aircraft technology, airborne ice measurements began in 1914. Once

the satellite era started, sea ice monitoring technology came to depend mainly on satellite-acquired images. Satellite remote sensing methodologies involve interpreting electromagnetic signatures of various sea ice types and characteristics. Remote sensing is performed using visible, infrared, and microwave spectral ranges.

Each spectral range has benefits and limitations for sea ice surveillance. Sea ice monitoring using the visible range is more intuitive to interpret but requires cloud-free images. The visible spectrum also depends on the sensitivity to conditions of natural illumination. In the visible spectrum, open water and ice types are differentiated by the albedo values, texture or reflection coefficient. The advantage of not requiring sunlight and capability to penetrate cloud cover gave an edge to passive microwave sensors for collecting measurements during the night. Several factors contribute towards the determination of sea ice information from these sensors, e.g., emissivity, ice types, snow, type of snow, snow grain radius, incident angle and so on [26] and hence make it challenging to interpret the data.

The visible spectrum of Advanced Very High-Resolution Radiometer (AVHRR) instruments onboard NOAA satellites 1.58 - 1.64 (um) are used to detect snow and ice. AVHRR near-infrared and thermal infrared images under cloud-free conditions were used to compute ice concentration and ice edge [22]. AVHRR spectral information was also used to derive sea ice motion vectors [64, 57] and high-resolution sea surface temperature products [75]. The global sea ice cover had also been estimated from satellite passive microwave sensors Scanning Multichannel Microwave Radiometer (SSMR) and later Special Sensor Microwave Imager/Sounder (SSMIS) [88] onboard Nimbus 7 and Defence Meteorological Satellites [10, 94]. The assimilation of remote sensing data into atmospheric/ocean models (observations) was performed to quantize

the error and produce improved estimates of sea ice parameters [67].

The AMSR-E sensor on NASA's Aqua satellite was used to retrieve sea ice concentration between 0% and 100%, using weather filters to reduce the atmospheric influence [84]. AMSR-E stopped collecting data on October 4, 2011. The successor AMSR2 onboard GCOM-W was processed to derive ice concentrations since August 2012 [39]. AMSR-E was also used to estimate sea ice drift in the central Arctic region [23].

SAR provides images with finer spatial resolution than microwave radiometers and is widely used to derive various ice information such as estimating ice type [83, 63], ice drift patterns [25, 89], and detecting polynias [19]. European Remote Sensing satellites, ERS-1 (1991-2000) and ERS-2 (1995-2011) were used for the detection of sea ice for various ice applications [6]. A combination of information derived from instruments such as AVHRR, SAR and in situ measurements were also used for ice detection [20]. The data derived from RADARSAT-1 were single polarisation and hence had limited capability. The RADARSAT-2 SAR collects data in dual and quad polarization modes and is used widely for various applications such as ice-edge detection, ice concentration, and stages of development of sea ice which are required for operational ice monitoring [79]. RADARSAT-2 was also used to estimate ice thickness, and snow properties [79] and for ice motion tracking [47]. National Ice Centres around the globe use predominantly SAR for ice mapping. For example, Operational ice monitoring at the Canadian Ice Service (CIS) generates products derived from RADARSAT-2 [17, 82]. The other SARs that are used for ice monitoring includes TerraSAR-X, Cosmo SkyMed, Sentinel-1, Advanced Land Observing Satellite (ALOS). TerraSAR-X was used for sea ice classification [74, 45], Cosmo SkyMed

X-band was used for the detection of polynias [14], Sentinel-1 SAR imageries were used for tracking sea ice motion [61], Advanced Land Observing Satellite (ALOS) PALSAR L-band images were used for detection of large ridges and to determine ice types during summer melt season [4]. Envisat Advanced Synthetic Aperture Radar (ASAR) Alternate Polarization (AP) C-band have been used to discriminate between the open water and ice during high wind conditions enabling better separation of ice types [3]. ASAR was also used to acquire information on deformed new ice [3].

Along with the determination of sea ice concentration and drift, there are sensors and algorithms that capture the information on other ice parameters, such as ice thickness and freeboard measures, which are more important for risk/safety in navigational and offshore resources. The ice thickness information was initially measured using the radar altimeters on board European Remote Sensing (ERS 1, ERS 2) satellites. Ice thickness was determined from the ice freeboard measurements determined using other altimeters [52]. Also, the previously mentioned sensors (AVHRR) thermal band information was combined with an ice growth model to estimate ice thickness during the winter season [107]. ICESat laser altimeter freeboard information was used to retrieve snow and ice thickness [49]. Sea-ice thickness retrieval and uncertainty estimations were also done using satellite radar/altimetry along with the freeboard/buoyancy principle and knowledge of geoid [95]. Ice thickness retrievals were also carried out using MODIS thermal images [49]. The brightness temperatures of L-band from Soil Moisture and Ocean Salinity satellite have been used to retrieve sea ice thickness up to 50 cm. [91, 43]. The presence of snow increased the uncertainty of the ice thickness retrieved from SMOS [91, 43]. CryoSat-2, a European Space Agency satellite provides information on ice freeboard and thickness in polar

and sub-polar region [29]. Ice thickness determination and information on leads were also done using SAR [27, 100].

IceBridge is a program that was initiated by NASA to acquire sea ice information from research aircraft [48]. The other means of deriving ice information was using upward Looking sonars, e.g., [87]. In most of the retrieval cases using satellite data, validation was done using the data derived from in situ sensors, such as ULS [49].

2.3 Sea ice modeling

The role of sea ice in the global climate has been known for half a century or more. Numerical models provide valuable information on how sea ice evolves and how it affects climate. Additionally, well-tuned numerical sea ice models may be used for short-term operational forecasts (one to five days) for navigation in sea ice-frequented regions, as well as seasonal forecasts (one to three months) to aid in planning. The models can be used to investigate weather patterns or events. GCMs simulate the climate of the whole world. They are usually used to study the effects of global climate disruptions caused by increases in carbon dioxide and other factors. Even a small increase in temperature can lead to greater warming over time, making the polar regions the most sensitive areas to climate change on Earth and hence most GCMs include sea ice models. The evolution of sea ice is highly complex and can only be approximated by mathematical equations, or statistical approaches that address the relevant dynamic and thermodynamic processes. Thermodynamic equations consider air and ocean temperatures, heat fluxes, albedo, and other forces that affect the formation and ablation of sea ice. Dynamic equations consider factors that influence

sea ice motion such as winds, currents, ice-ocean drag and other forces.

Thermodynamic modeling efforts of sea ice processes started with the classical work of Stefan [86] in 1891 where he discussed the theoretical approaches to heat conduction in ice to compute growth rates. Later, Untersteiner [98, 99] discussed the internal heat source due to solar radiation in 1961 and 1964. His work examined internal heat source, variable thermal conductivity, specific heat, and vertical advection of heat in ice during melting or formation. Modeling efforts were further improved by Maykut and Untersteiner [58] in 1971 by creating a more complex model for sea ice thermodynamics, which laid the foundation for today's modeling studies. The one-dimensional model developed by Maykut and Untersteiner [58] included the surface energy balances to determine rates of ablation and accretion and the effects of snow cover, ice salinity and internal heating due to the penetration of solar radiation. The study showed that snow depths of less than 70 cm had little effect on equilibrium ice thickness, but snow depths greater than 70 cm resulted in thicker ice. Maykut and Untersteiners [58] model had been too complex to be used for coupled climate simulation studies. Semtner [80] (in 1976) simplified the model of Maykut and Untersteiner [58] so that it could be employed in climate models. He presented a model with two-layer ice and one layer snow that considered pure-ice values of heat capacity and thermal conductivity [80]. He also presented a zero-layer model, by assuming a linear temperature profile in the ice and neglecting the internal energy [80]. Hibler [32] made further contributions in sea ice modeling by considering the oceanic mixed layer and lateral melting effects. Parkinson and Washington (1979) [66] included the effect of leads. Cox and Weeks developed an empirical formula for winter sea-ice desalination [16] (1988). The approach by Cox and Weeks was later used to determine transitions

from the first year to the multiyear ice by Vancoppenolle and others in 2005 [102]. Ebert and Curry in 1993 [21] developed parameterization to include brine pockets, melt ponds, and albedos with different spectral bands. Bitz and Lipscomb [9] developed an energy-conserving thermodynamic model with brine-pocket parametrization. The energy absorbed during the melt was used to raise the temperature of the ice and also to expand the brine pockets. Feltham et al. [24] treated sea ice as a mush layer that consists of a mixture of ice crystals and concentrated brine. Based on mushy layer parametrization of Feltham et al. [24] gravity drainage was introduced in the thermodynamic component of the sea ice model by Hunke et al. [97].

Campbell [11] treated the ice as a Newtonian viscous fluid while Hibler [30] treated ice as a linear viscous fluid. Thorndike et al. [90] treated sea ice as a viscous-plastic material and also considered thickness changes using the ITD equation [90]. Lipscomb [55] explained the remapping method for the thickness distribution and suggested that five to seven categories of ice thickness with high resolution for thin ice thickness, plus open water, were sufficient to simulate the annual cycles of ice thickness. The modeling studies were also accompanied by fieldwork programs such as the Arctic Ice Dynamics Joint Experiment (AIDJEX). AIDJEX [71] experiments and simulation studies by Coon et al. [15] proposed an elastic-plastic rheology. A nonlinear viscous-plastic (VP) rheology proposed by Hibler [31] had a significant effect on the drift, deformation, and thickness of sea ice [40, 60]. Hunke et al. [37] introduced the EVP model for ice dynamics to provide more accurate results. The EVP model was computationally more efficient and reduced to the original VP model on long timescales. Wilchinsky and Feltham [104] proposed an elastic anisotropic plastic rheology model and treated ice as the anisotropic interlocking, anisotropic

diamond-shaped ice floes.

In 1980s, large-scale climate models began incorporating sea ice models, e.g., Hibler and Bryan in 1987 coupled ocean model with a sea ice model [33]. The model was used to investigate the effect of ocean circulation on seasonal sea ice variations. Along with the modeling of thermodynamics and dynamics to generate more physically realistic models, the geometry and process of ridging and rafting which influences the ice thickness distributions were also required. Timco and Burden [92] and Timco et al. [93] investigated the structure and formation of first-year ridges and the relationships between ridge parameters. Bailey et al. [7] investigated the process of rafting of sea ice using a 1-D thermal consolidation model. Tsamados et al. [96] introduced the estimation of ice-ocean drag from the properties of ice cover such as ice concentrations, ridges, freeboard and floe draft, the size of floes and melt ponds. Most recently, NANSEN environment services have been developing a Lagrangian sea ice model that includes a wave-ice interaction module [73]. Attempts had also been made to develop model-based forecasting tools for monitoring formation/ablation and movement of sea ice. Sayed et al. [77] provided an overview of an operational ice model that was coupled with an atmospheric, ocean modules. The work was followed by the development of an operational ice dynamics model for the Canadian Ice Service [78]. The coupled model included viscous plastic rheology and a Particle-In-Cell (PIC) method to model ice advection. The Zhang-Hibler scheme was used to solve the momentum equations. A scheme to model the evolution of thickness distribution was also introduced to the work. It was observed that the model's performance was good, though the estimated accuracy of the results based on ice thickness and volume were hard to determine [78]. Caya [13] used a multi-thickness category ice model coupled with Princeton

Ocean Model (CIOM) for the simulation of ocean parameters. The model had a grid resolution of $(1/5)^\circ$ longitude, $(1/6)^\circ$ latitude with 16 vertical layers for the ocean. The study concluded that the model's performance was not good enough to capture a 24-hour future forecast. The imperfections in the forecast model were attributed due to the non-optimal update of ice velocity and ocean variables by the assimilation process, the imperfect ocean lateral boundary conditions, and atmospheric forcing [13].

2.4 Review of sea ice models

In this section, we discuss the available sea ice models, their advantages, disadvantages and some related works. There are several coupled and standalone ice models that were available for sea ice simulation studies on both regional and global scales. An inter-comparison of some of the available coupled sea-ice models and their physics can be found in [35, 8]. Other coupled models such as the Regional Ocean Modeling System (ROMS), Nucleus for European Modelling of the Ocean (NEMO), MIT General Circulation Model (MITgcm), and Community Climate Systems Model (CCSM) provide insights into the physical processes between the ocean, atmosphere, and sea ice. However, the sensitivity of coupled models to atmospheric, oceanic and sea ice parameters must be studied in detail to tune the model physics and parameters depending upon the feedback among these modules.

ROMS was a tightly coupled sea ice model based on EVP dynamics [37]. The sea ice component of ROMS is a single-layered ice and snow thermodynamics model. The modeling framework, physics, and equations are described in the ROMS Manual

[28]. NEMO was a coupled ice-ocean model with the sea ice component Louvain-la-NeuveSea Ice Model (LIM2 and LIM3). LIM2, a two-layer thermodynamic-dynamic model, and LIM3, a five-category model, were both coupled with the NEMO ocean model. The model result analyses include ice concentration, thickness and drift parameters [101]. There are other versions of NEMO which used the Los Alamos sea ice model (CICE) instead of LIM1 and LIM2 [72]. The ice-ocean coupled model MITgcm also came with a sea ice module [1] based on the thermodynamics schemes in the CICE model [38].

The major disadvantages of coupled ice-ocean models are their complexity, additional computation time, parameter tuning and management of large data quantities. Most sea ice modeling studies focus on a global scale simulations using coupled models. Models that have most of the advanced features that represent sea ice information are shown in Table 2.1.

The sea ice models that are presented in Table 2.1 are all coupled global climate models. There are also regional coupled ice-ocean models, e.g., the Regional Ocean Modeling System (ROMS) has a coupled sea ice model which has one layer of ice/snow, ITD and has EVP dynamics. Besides solving ITD, momentum equations, enthalpy and heat equations, an advanced model such as CICE [38] considers snow grain radius, melt pond schemes, melt pond albedos, floe size, sails and keels, ridging and redistribution schemes that use realistic physics, and freeboard measures. The sea ice model, CICE used in this study is a component of CCSM, see Table 2.1, developed at Los Alamos Laboratory, USA and can also be implemented in uncoupled, standalone mode [38, 70].

Table 2.1: List of sea ice models

	Model Name	Model Strength
1	ROMS	1 layer ice and 1 layer snow model. Tightly coupled with the ocean model. The ice deformation and ridging effects are not considered. Based on EVP dynamics.
2	LIM (NEMO)	LIM2 and LIM3 (advanced) with EVP dynamics, ITD equations, coupled with the NEMO ocean model
3	MITgcm	Sea ice model is a part of MITgcm. Coupled with ocean. EVP dynamics.
4	CIOM	Coupled Princeton Ocean model and sea ice model. EVP dynamics and ITD equation.
5	CICE	Los Alamos Sea Ice Model. EVP and EAP dynamics, Melt pond parameterizations, Ridging, and ice deformation ITD equations.
6	Finnish Ice Prna, Center	EVP rheology, Ridging and ice deformation ITD equations.

2.5 Data assimilation

Due to computational complexity and sophisticated physical processes, several parameters in general circulation models are based on certain assumptions. The assumptions on model physics, uncertainties associated with boundary or forcing data in the geophysical models limit model accuracy. Data assimilation aims to optimally combine observations with the model and serves as a valuable tool for improving model estimates for a forecast. Observational data may include ground, satellite, aircraft, buoy, ULS or any other field, or remote sensing measurement.

Geophysical models provide estimates in their domain of interest either regional or global. Observation from satellite sensors or in-situ measurements depends on several factors such as revisiting time, the location of the instruments, band frequency and ice properties, e.g., the retrieval of quantities like snow thickness and ice thickness are limited since the electromagnetic radiation can penetrate only a very thin surface layer. Data assimilation systems can expand information from remote sensing observations to all model variables that are in some way dependent on the observations and produce a better forecast.

The optimal combination for data assimilation is based on the consideration of uncertainties of the observations and model estimates. Whenever highly accurate remote sensing data are available, the assimilated estimates will be close to the observations otherwise model estimates are accepted as the true state. Several data assimilation methodologies such as nudging, probabilistic, multivariate statistical methods, variational method such as 3D variational (3D-VAR), Kalman filters, and ensembles exist [51]. In addition to the methods above, advanced data assimilation methods such as

extended and ensemble Kalman filters, as well as 4D variational (4D-VAR),also exists. The fundamental principle of all data assimilation methods includes merging models and observations, but the sophistication, computational burden and the quality of results of the merging algorithm vary widely. Some are computationally efficient with satisfactory or even substantial results, while others are computationally intense and lead to better results. Following is a summary of some of the data assimilation methods.

The most straightforward type of the data assimilation is the nudging method [34, 46]. It introduces into the dynamical equations of the model an additional term that is proportional to the difference of the calculated meteorological variable and the observed value. The nudging method continuously relaxes the model values (background) towards the observations. The gain matrix in the nudging method is usually prescribed rather than derived from the observation and model errors. There exist variations of the nudging techniques such as back and forth nudging [50]. Back and forth nudging first solves the forward equations with a nudging term. The final state obtained is then used as an initial condition to solve the same equation in a backward direction with a feedback term. The analysis of this backward equation gives an estimate of the initial state of the system. The process is iterated until convergence of the initial state is achieved. The advantage of the nudging method is reduced sophistication, increased flexibility, greater ease of implementation and low computational cost. A case of nudging is used to introduce open boundaries [38, 28] in ice-ocean models. Usually, such methods do not use any theoretical or statistical basis as they just push the model values close to the observation/climatology. The advantage is its ease of use and low computational expense.

One of the simple and powerful methods used in various weather prediction models is the optimal interpolation (OI) method. OI is more computationally expensive than nudging and uses a least square method for data assimilation where the weights for the observations are assigned according to some known or estimated error statistics [18]. Variations of OI have also been applied to sea ice models, e.g., Lindsay et al. [54] and Wang et al. [103]. Both methodologies showed improvement in the estimated model results when compared with the free runs.

Another method of assimilation is the variational cost function approach [76]. Here the variational methods of assimilation replace the update step with an optimization problem; these are typically nonprobabilistic and provide a single best estimate of the state. 3D-VAR and 4D-VAR are based on the variational cost function approach. The variational methods usually require minimization of a cost function [53]. The selection of cost function is in such a way that the analysis does not drift too far from observations and forecasts that are known to be usually reliable. It depends on the deviation of analysis values from the observations weighted by the accuracy of observations and the deviations of the forecast fields and analyzed fields weighted by the accuracy of the forecast. Variational methods like 3D-VAR and 4D-VAR use information about the spatial distribution of covariance functions of the errors of the previous forecast and the actual observation. 3D-VAR uses all the observations in the domain simultaneously, whereas OI restricts the effect of any observation on all the grid cells of the domain. However, in the linear case, 3D-VAR and OI are equivalent. Also, the model error covariance matrix in OI is usually assumed to be constant, unlike 3D-VAR, where the model covariances may be estimated from the average of multiple analysis model differences from short range data assimilation forecasts.

3D-VAR propagates adjustments in the control variables according to the linear or nonlinearity of the system rather than through only statistical relationships as OI. 3D-VAR does not account for variation of observation over time, which is considered in 4D-VAR. Caya et al. [13] used the 3D-VAR scheme to assimilate the SSMI/SSMIS observation into the ice-ocean model. The 3D-VAR scheme was also extended to include more observations like CIS ice chart and RADARSAT SAR analysis [12]. Stark et al. [85] used a different cost function to assimilate the ice concentration and ice motion vectors into the coupled ice-ocean model.

The assumption of constant error covariance matrix over time could add additional errors to the assimilated model. To compute the propagation of error over time, advanced data assimilation methods such as 4D-VAR, extended Kalman filter, ensemble, and other variants of Kalman filters [65] are used. They are computationally expensive but have the possibility of providing better estimates. Kalman filter (KF) can be considered similar to OI except OI calculates a constant estimate whereas KF uses the model to calculate the error covariance matrix. Extended Kalman Filter [41] uses a linear adjoint model to forecast the evolved error covariance matrix that is employed in the analysis step. If an adequate number of observations are available over time, the extended Kalman could provide the best assimilation results compared to the inexpensive computational methods discussed above. Extended Kalman filter is one of the most computationally expensive methods [44] and hence in many cases replaced with assumptions of constant errors to minimize computational time. Ensemble Kalman filtering [36] reduces the computational time of extended Kalman filter. It runs a collection of simultaneous data assimilation cycles independently and finally combines them to produce an analysis of the control variables [5]. The singular

evolutive extended Kalman (SEEK) [69] is another type of Kalman filter. SEEK filters make use of square root factorization of the covariance matrices and reformulate the KF steps using square roots instead of the full matrices. When the linearization in a SEEK filter is replaced by linear interpolation, it becomes the Singular Evolutive Interpolated Kalman (SEIK) Filter [68]. SEIK is thus a variant of the SEEK filter that can be interpreted as an ensemble filter with a reduced ensemble. The benefit of SEIK is that it avoids the complex computational burden of the gradient required by the SEEK filter and is more robust concerning model nonlinearities. While using Kalman filters, to keep the computation time low, the ensembles are chosen to be small even for large-scale models. Small ensembles may lead to significant sampling errors of the error covariance matrix. To overcome this issue localization of covariance matrices are preferred in which long-distance covariances are damped or neglected. Yang et al. [106] used a Localized Singular Evolutive Interpolated Kalman (LSEIK) filter to assimilate ESA's SMOS ice thickness data and SSMIS ice concentration. Ensemble-based prediction is the other set of methods in data assimilation where, instead of making a single forecast, several ensembles or future states are generated [81, 51]. Xie et al. [105] used ensemble Kalman filtering for the assimilating thin ice from SMOS into the TOPAZ system, which is a coupled ice-ocean forecast system and the system also assimilated sea surface temperature, altimetry data, temperature and salinity profiles, ice concentration, and ice drift.

2.6 Grid generation methods

By default, CICE uses displaced pole grids of 3° and 1° for global applications. The regional implementation of the model is rarely discussed in the literature. One of the regional implementations, 3D-CEMBS, a coupled ice-ocean model that used CICE, was implemented on a rotated stereographic grid co-ordinates. The work did not discuss the results of the sea ice parameters such as ice concentration, thickness. This section presents a literature review of the methods that are used to generate rotated grids for global and regional implementations. A non-rotated orthogonal curvilinear grid is used for the regional implementation discussed in Chapter 3.

The ice-ocean or atmospheric models are represented by partial differential equations to define the physical processes of atmosphere-ice-ocean. They are solved using advanced computational methods such as domain decomposition and parallel algorithms. In GCMS, prognostic variables such as temperature, salinity, and velocity, are discretized on Arakawa grids which include five different varieties of grids. The Arakawa grids include unstaggered and staggered grids. An unstaggered grid or A grid will define all the variables at the same point either at the center or the corner point of a grid cell, whereas staggered grids (B, C, D, and E) define the variables at different points of the grid cell [2]. The staggered grids B and C are usually preferred in the climate modeling framework.

Along with discretization of model equations, another issue that the numerical ice-ocean models have to overcome is the singularity at the poles caused by the convergence of latitude and longitude. The convergence at the poles generates numerical errors in the Arctic configuration of the GCMs. To overcome such singularity the

mesh/grid generation techniques follow different methodologies. One of the methodologies is to shift the pole over the land cells and generate orthogonal curvilinear grids using a conformal transformation [56], see Figure 2.1. Another methodology follows the generation of more than one pole, all located over the land cells [62], see Figure 2.1. The method for regional models which does not include the poles can be resolved easily by using orthogonal curvilinear, rectilinear (arises as a special case of the above methodology) or spherical coordinates, with fitted boundaries [59]. Also, there are methods, which include the use non-orthogonal grids usually used for finite volume, finite element methods of modelig the ocean [59].

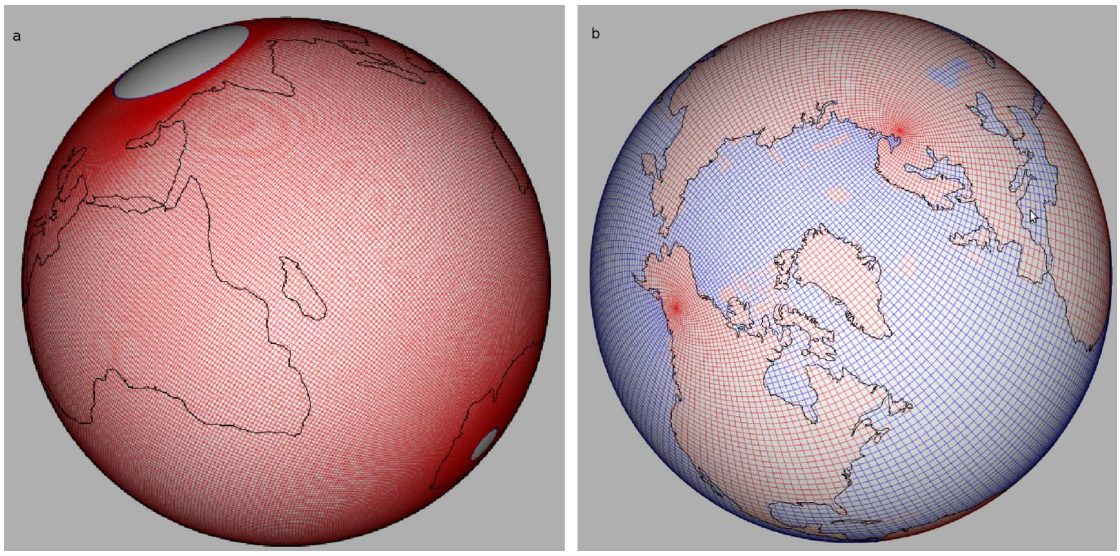

Figure 2.1: (a) Dipole grid (b) Tripole grid

Bibliography

[1] A. Adcroft, J. Campin, S. Dutkiewicz, C. Evangelinos, D. Ferreira, G. Forget, B. Fox-Kemper, P. Heimbach, C. Hill, E. Hill, et al. MITgcm user manual, 2008.

[2] A. Arakawa and V. R. Lamb. Methods of computational physics. *Academic Press*, 17:174–265, 1977.

[3] M. Arkett, D. Flett, and R. De Abreu. C-band multiple polarization SAR for ice monitoring–What can it do for the Canadian ice service. 2003.

[4] M. Arkett, D. Flett, R. De Abreu, P. Clemente-Colón, J. Woods, and B. Melchior. Evaluating ALOS-PALSAR for ice monitoring-what can L-band do for the North American ice service? In *Geoscience and Remote Sensing Symposium, 2008. IGARSS 2008. IEEE International*, volume 5, pages V–188. IEEE, 2008.

[5] M. Asch, M. Bocquet, and M. Nodet. *Data assimilation: methods, algorithms, and applications*. SIAM, 2016.

[6] J. Askne, A. Carlstrom, W. Dierking, and L. Ulander. ERS-1 SAR backscatter modeling and interpretation of sea ice signatures. In *Geoscience and Remote*

Sensing Symposium, 1994. IGARSS'94. Surface and Atmospheric Remote Sensing: Technologies, Data Analysis and Interpretation., International, volume 1, pages 162–164. IEEE, 1994.

[7] E. Bailey, D. Feltham, and P. Sammonds. A model for the consolidation of rafted sea ice. *Journal of Geophysical Research: Oceans*, 115(C4), 2010.

[8] C. M. Bitz. Numerical modeling of sea ice in the climate system, 2008.

[9] C. M. Bitz and W. H. Lipscomb. An energy-conserving thermodynamic model of sea ice. *Journal of Geophysical Research: Oceans*, 104(C7):15669–15677, 1999.

[10] E. Bjørgo, O. M. Johannessen, and M. W. Miles. Analysis of merged SMMR-SSMI time series of Arctic and Antarctic sea ice parameters 1978–1995. *Geophysical Research Letters*, 24(4):413–416, 1997.

[11] W. J. Campbell. The wind-driven circulation of ice and water in a polar ocean. *Journal of Geophysical Research*, 70(14):3279–3301, 1965.

[12] A. Caya, M. Buehner, and T. Carrieres. Analysis and forecasting of sea ice conditions with three-dimensional variational data assimilation and a coupled ice–ocean model. *Journal of Atmospheric and Oceanic Technology*, 27(2):353–369, 2010.

[13] A. Caya, M. Buehner, M. Shokr, and T. Carrieres. A first attempt of data assimilation for operational sea ice monitoring in Canada. In *Geoscience and Remote*

Sensing Symposium, 2006. IGARSS 2006. IEEE International Conference on, pages 1705–1708. IEEE, 2006.

[14] A. Ciappa and L. Pietranera. High resolution observations of the Terra Nova Bay polynya using COSMO-SkyMed X-SAR and other satellite imagery. *Journal of Marine Systems*, 113:42–51, 2013.

[15] M. Coon, G. Maykut, and R. Pritchard. Modeling the pack ice as an elastic-plastic material. 1974.

[16] G. Cox and W. Weeks. Numerical simulations of the profile properties of undeformed first-year sea ice during the growth season. *Journal of Geophysical Research: Oceans*, 93(C10):12449–12460, 1988.

[17] R. De Abreu, D. Flett, B. Scheuchl, and B. Ramsay. Operational sea ice monitoring with RADARSAT-2-a glimpse into the future. In *Geoscience and Remote Sensing Symposium, 2003. IGARSS'03. Proceedings. 2003 IEEE International*, volume 2, pages 1308–1310. IEEE, 2003.

[18] R. Deutch. Estimation theory. 1965.

[19] S. T. Dokken, P. Winsor, T. Markus, J. Askne, and G. Björk. ERS SAR characterization of coastal polynyas in the Arctic and comparison with SSM/I and numerical model investigations. *Remote Sensing of Environment*, 80(2):321–335, 2002.

[20] R. Drucker, S. Martin, and R. Moritz. Observations of ice thickness and frazil ice in the St. Lawrence Island polynya from satellite imagery, upward looking

sonar, and salinity/temperature moorings. *Journal of Geophysical Research: Oceans*, 108(C5), 2003.

[21] E. E. Ebert and J. A. Curry. An intermediate one-dimensional thermodynamic sea ice model for investigating ice–atmosphere interactions. *Journal of Geophysical Research: Oceans*, 98(C6):10085–10109, 1993.

[22] W. Emery, M. Radebaugh, C. Fowler, D. Cavalieri, and K. Steffen. A comparison of sea ice parameters computed from advanced very high resolution radiometer and Landsat satellite imagery and from airborne passive microwave radiometry. *Journal of Geophysical Research: Oceans*, 96(C12):22075–22085, 1991.

[23] R. Ezraty, F. Girard-Ardhuin, and D. Croizé-Fillon. Sea ice drift in the central Arctic using the 89 GHz brightness temperatures of the Advanced Microwave Scanning Radiometer. *Users Manual, IFREMER, Brest, France*, 2007.

[24] D. Feltham, N. Untersteiner, J. Wettlaufer, and M. Worster. Sea ice is a mushy layer. *Geophysical Research Letters*, 33(14), 2006.

[25] M. Fily and D. Rothrock. Sea ice tracking by nested correlations. *IEEE Transactions on Geoscience and Remote Sensing*, (5):570–580, 1987.

[26] M. Hallikainen and D. P. Winebrenner. The physical basis for sea ice remote sensing. *Microwave Remote Sensing of Sea ice*, pages 29–46, 1992.

[27] D. Haverkamp, L. K. Soh, and C. Tsatsoulis. A comprehensive, automated approach to determining sea ice thickness from SAR data. *IEEE Transactions on Geoscience and Remote Sensing*, 33(1):46–57, 1995.

[28] K. S. Hedström. *Technical manual for a coupled sea-ice/ocean circulation model (version 3)*. Citeseer, 2009.

[29] S. Hendricks, R. Ricker, and V. Helm. AWI CryoSat-2 Sea Ice Thickness Data Product. *Data product manual, Alfred-Wegener-Institut*, 2013.

[30] W. Hibler. Differential sea-ice drift. II. Comparison of mesoscale strain measurements to linear drift theory predictions. *Journal of Glaciology*, 13(69):457–471, 1974.

[31] W. Hibler III. A dynamic thermodynamic sea ice model. *Journal of Physical Oceanography*, 9(4):815–846, 1979.

[32] W. Hibler Iii. Modeling a variable thickness sea ice cover. *Monthly weather review*, 108(12):1943–1973, 1980.

[33] W. Hibler III and K. Bryan. A diagnostic ice–ocean model. *Journal of Physical Oceanography*, 17(7):987–1015, 1987.

[34] J. E. Hoke and R. A. Anthes. The initialization of numerical models by a dynamic-initialization technique. *Monthly Weather Review*, 104(12):1551–1556, 1976.

[35] M. M. Holland and C. M. Bitz. Polar amplification of climate change in coupled models. *Climate Dynamics*, 21(3-4):221–232, 2003.

[36] P. L. Houtekamer and H. L. Mitchell. Data assimilation using an ensemble Kalman filter technique. *Monthly Weather Review*, 126(3):796–811, 1998.

[37] E. Hunke and J. Dukowicz. An elastic–viscous–plastic model for sea ice dynamics. *Journal of Physical Oceanography*, 27(9):1849–1867, 1997.

[38] E. C. Hunke, W. H. Lipscomb, A. K. Turner, N. Jeffery, and S. Elliott. CICE: the Los Alamos Sea Ice Model Documentation and Software Users Manual Version 5.1 LA-CC-06-012. *T-3 Fluid Dynamics Group, Los Alamos National Laboratory*, 675, 2015.

[39] K. Imaoka, M. Kachi, M. Kasahara, N. Ito, K. Nakagawa, and T. Oki. Instrument performance and calibration of AMSR-E and AMSR2. *International Archives of the Photogrammetry, Remote Sensing and Spatial Information Science*, 38(8):13–18, 2010.

[40] B. Ip, W. Hibler, and G. Flato. The Effect Of Rheology On Seasonal Sea-Ice Simulations. *Annals of Glaciology*, 14:340–340, 1990.

[41] A. Jazwinski. Stochastic Process and Filtering Theory, Academic Press. *A subsidiary of Harcourt Brace Jovanovich Publishers*, 1970.

[42] O. M. Johannessen, V. Alexandrov, I. Y. Frolov, S. Sandven, L. H. Pettersson, L. P. Bobylev, K. Kloster, V. G. Smirnov, Y. U. Mironov, and N. G. Babich. *Remote sensing of sea ice in the Northern Sea Route: studies and applications*. Springer Science & Business Media, 2006.

[43] L. Kaleschke, X. Tian-Kunze, N. Maaß, M. Mäkynen, and M. Drusch. Sea ice thickness retrieval from SMOS brightness temperatures during the Arctic freeze-up period. *Geophysical Research Letters*, 39(5), 2012.

[44] E. Kalnay. *Atmospheric modeling, data assimilation and predictability*. Cambridge University Press, 2003.

[45] J.-W. Kim, D.-j. Kim, and B. J. Hwang. Characterization of Arctic sea ice thickness using high-resolution spaceborne polarimetric SAR data. *IEEE Transactions on Geoscience and Remote Sensing*, 50(1):13–22, 2012.

[46] R. E. Kistler. *A study of data assimilation techniques in an autobarotropic, primitive equation, channel model*. PhD thesis, Pennsylvania State University, 1974.

[47] A. S. Komarov and D. G. Barber. Sea ice motion tracking from sequential dual-polarization RADARSAT-2 images. *IEEE Transactions on Geoscience and Remote Sensing*, 52(1):121–136, 2014.

[48] N. Kurtz, S. Farrell, M. Studinger, N. Galin, J. Harbeck, R. Lindsay, V. Onana, B. Panzer, and J. Sonntag. Sea ice thickness, freeboard, and snow depth products from Operation IceBridge airborne data. 2013.

[49] R. Kwok and G. Cunningham. ICESat over Arctic sea ice: Estimation of snow depth and ice thickness. *Journal of Geophysical Research: Oceans*, 113(C8), 2008.

[50] S. Lakshmivarahan and J. M. Lewis. Nudging methods: a critical overview. In *Data Assimilation for Atmospheric, Oceanic and Hydrologic Applications (Vol. II)*, pages 27–57. Springer, 2013.

[51] K. Law, A. Stuart, and K. Zygalakis. *Data assimilation: a mathematical introduction*, volume 62. Springer, 2015.

[52] S. Laxon, N. Peacock, and D. Smith. High interannual variability of sea ice thickness in the Arctic region. *Nature*, 425(6961):947–950, 2003.

[53] F.-X. Le Dimet, I. M. Navon, and R. Ştefănescu. Variational data assimilation: optimization and optimal control. In *Data Assimilation for Atmospheric, Oceanic and Hydrologic Applications (Vol. III)*, pages 1–53. Springer, 2017.

[54] Lindsay, RW and Zhang, J. Assimilation of ice concentration in an ice–ocean model. *Journal of Atmospheric and Oceanic Technology*, 23(5):742–749, 2006.

[55] W. H. Lipscomb. Remapping the thickness distribution in sea ice models. *Journal of Geophysical Research: Oceans*, 106(C7):13989–14000, 2001.

[56] G. Madec and M. Imbard. A global ocean mesh to overcome the North Pole singularity. *Climate Dynamics*, 12(6):381–388, 1996.

[57] J. Maslanik, C. Fowler, J. Key, T. Scambos, T. Hutchinson, and W. Emery. AVHRR-based Polar Pathfinder products for modeling applications. *Annals of Glaciology*, 25:388–392, 1997.

[58] G. A. Maykut and N. Untersteiner. Some results from a time-dependent thermodynamic model of sea ice. *Journal of Geophysical Research*, 76(6):1550–1575, 1971.

[59] G. L. Mellor and S. Häkkinen. A review of coupled ice-ocean models. *The Polar Oceans and Their Role in Shaping the Global Environment*, pages 21–31, 1994.

[60] P. A. Miller, S. W. Laxon, and D. L. Feltham. Improving the spatial distribution of modeled Arctic sea ice thickness. *Geophysical Research Letters*, 32(18), 2005.

[61] S. Muckenhuber and S. Sandven. Open-source sea ice drift algorithm for Sentinel-1 SAR imagery using a combination of feature tracking and pattern matching. *Cryosphere*, 11(4):1835, 2017.

[62] R. J. Murray. Explicit generation of orthogonal grids for ocean models. *Journal of Computational Physics*, 126(2):251–273, 1996.

[63] S. Nghiem and C. Bertoia. Study of multi-polarization C-band backscatter signatures for Arctic sea ice mapping with future satellite SAR. *Canadian Journal of Remote Sensing*, 27(5):387–402, 2001.

[64] R. Ninnis, W. Emery, and M. Collins. Automated extraction of pack ice motion from advanced very high resolution radiometer imagery. *Journal of Geophysical Research: Oceans*, 91(C9):10725–10734, 1986.

[65] S. K. Park and L. Xu. *Data assimilation for atmospheric, oceanic and hydrologic applications*, volume 2. Springer Science & Business Media, 2013.

[66] C. L. Parkinson and W. M. Washington. A large-scale numerical model of sea ice. *Journal of Geophysical Research: Oceans*, 84(C1):311–337, 1979.

[67] L. T. Pedersen. Merging microwave radiometer data and meteorological data for improved sea ice concentrations. *EARSeL Advances in Remote Sensing*, 3(2-XII):81–89, 1994.

[68] D. T. Pham. Stochastic methods for sequential data assimilation in strongly nonlinear systems. *Monthly weather review*, 129(5):1194–1207, 2001.

[69] D. T. Pham, J. Verron, and M. C. Roubaud. A singular evolutive extended Kalman filter for data assimilation in oceanography. *Journal of Marine systems*, 16(3):323–340, 1998.

[70] S. Prasad, I. Zakharov, P. Bobby, and P. McGuire. The implementation of sea ice model on a regional high-resolution scale. *Ocean Dynamics*, 65(9-10):1353–1366, 2015.

[71] R. Pritchard, M. Coon, and M. McPhee. Simulation of sea ice dynamics during AIDJEX. *Journal of Pressure Vessel Technology*, 99(3):491–497, 1977.

[72] J. Rae, H. Hewitt, A. Keen, J. Ridley, A. West, C. Harris, E. Hunke, and D. Walters. Development of the Global Sea Ice 6.0 CICE configuration for the Met Office Global coupled model. *Geoscientific Model Development*, 8(7):2221–2230, 2015.

[73] P. Rampal, S. Bouillon, E. Ólason, and M. Morlighem. neXtSIM: a new Lagrangian sea ice model. *Cryosphere*, 10(3), 2016.

[74] R. Ressel, A. Frost, and S. Lehner. A neural network-based classification for sea ice types on X-band SAR images. *IEEE Journal of Selected Topics in Applied Earth Observations and Remote Sensing*, 8(7):3672–3680, 2015.

[75] R. W. Reynolds, T. M. Smith, C. Liu, D. B. Chelton, K. S. Casey, and M. G. Schlax. Daily high-resolution-blended analyses for sea surface temperature. *Journal of Climate*, 20(22):5473–5496, 2007.

[76] Y. Sasaki. Some basic formalisms in numerical variational analysis. *Monthly Weather Review*, 98(12):875–883, 1970.

[77] M. Sayed, T. Carrieres, et al. Overview of a new operational ice model. In *The Ninth International Offshore and Polar Engineering Conference*. International Society of Offshore and Polar Engineers, 1999.

[78] M. Sayed, T. Carrieres, H. Tran, S. B. Savage, et al. Development of an operational ice dynamics model for the Canadian Ice Service. In *The Twelfth International Offshore and Polar Engineering Conference*. International Society of Offshore and Polar Engineers, 2002.

[79] B. Scheuchl, D. Flett, R. Caves, and I. Cumming. Potential of RADARSAT-2 data for operational sea ice monitoring. *Canadian Journal of Remote Sensing*, 30(3):448–461, 2004.

[80] A. J. Semtner Jr. A model for the thermodynamic growth of sea ice in numerical investigations of climate. *Journal of Physical Oceanography*, 6(3):379–389, 1976.

[81] G.-H. Seo, S. Kim, B.-J. Choi, Y.-K. Cho, and Y.-H. Kim. Implementation of the ensemble Kalman filter into a Northwest Pacific Ocean circulation model. *Data Assimilation for Atmospheric, Oceanic and Hydrologic Applications*, pages 341–352, 2009.

[82] M. Shokr and N. Sinha. *Sea ice: physics and remote sensing*. John Wiley & Sons, 2015.

[83] M. E. Shokr. Evaluation of second-order texture parameters for sea ice classification from radar images. *Journal of Geophysical Research: Oceans*, 96(C6):10625–10640, 1991.

[84] G. Spreen, L. Kaleschke, and G. Heygster. Sea ice remote sensing using AMSR-E 89-GHz channels. *Journal of Geophysical Research: Oceans*, 113(C2), 2008.

[85] J. D. Stark, J. Ridley, M. Martin, and A. Hines. Sea ice concentration and motion assimilation in a sea ice- ocean model. *Journal of Geophysical Research: Oceans*, 113(C5), 2008.

[86] J. Stefan. Ueber die Theorie der Eisbildung insbesondere uebcr die Eisbildung im Polarmeere. *Ann. Phvs. Chem. NF 42, 269*, 286, 1891.

[87] V. H. Strass. Measuring sea ice draft and coverage with moored upward looking sonars. *Deep Sea Research Part I: Oceanographic Research Papers*, 45(4-5):795–818, 1998.

[88] N. Sun and F. Weng. Evaluation of special sensor microwave imager/sounder (SSMIS) environmental data records. *IEEE Transactions on Geoscience and Remote Sensing*, 46(4):1006–1016, 2008.

[89] Y. Sun. Automatic ice motion retrieval from ERS-1 SAR images using the optical flow method. *International Journal of Remote Sensing*, 17(11):2059–2087, 1996.

[90] A. Thorndike, D. Rothrock, G. Maykut, and R. Colony. The thickness distribution of sea ice. *Journal of Geophysical Research*, 80(33):4501–4513, 1975.

[91] X. Tian-Kunze, L. Kaleschke, N. Maaß, M. Mäkynen, N. Serra, M. Drusch, and T. Krumpen. SMOS-derived thin sea ice thickness: algorithm baseline, product specifications and initial verification. *Cryosphere*, 8(3):997–1018, 2014.

[92] G. Timco and R. Burden. An analysis of the shapes of sea ice ridges. *Cold Regions Science and Technology*, 25(1):65–77, 1997.

[93] G. Timco, K. Croasdale, and B. Wright. An overview of first-year sea ice ridges. *PERD/CHC report*, pages 5–112, 2000.

[94] R. Tonboe, J. Lavelle, R.-H. Pfeiffer, and E. Howe. Product User Manual for OSI SAF Global Sea Ice Concentration. 2016.

[95] R. Tonboe, L. Pedersen, and C. Haas. Simulation of the satellite radar altimeter sea ice thickness retrieval uncertainty. *The Cryosphere Discussions*, 3(2):513–559, 2009.

[96] M. Tsamados, D. L. Feltham, and A. Wilchinsky. Impact of a new anisotropic rheology on simulations of Arctic sea ice. *Journal of Geophysical Research: Oceans*, 118(1):91–107, 2013.

[97] A. K. Turner, E. C. Hunke, and C. M. Bitz. Two modes of sea-ice gravity drainage: A parameterization for large-scale modeling. *Journal of Geophysical Research: Oceans*, 118(5):2279–2294, 2013.

[98] N. Untersteiner. On the mass and heat budget of Arctic sea ice. *Archiv für Meteorologie, Geophysik und Bioklimatologie, Serie A*, 12(2):151–182, 1961.

[99] N. Untersteiner. Calculations of temperature regime and heat budget of sea ice in the central Arctic. *Journal of Geophysical Research*, 69(22):4755–4766, 1964.

[100] M. M. Van Dyne, C. Tsatsoulis, and F. Fetterer. Analyzing lead information from SAR images. *IEEE Transactions on Geoscience and Remote Sensing*, 36(2):647–660, 1998.

[101] M. Vancoppenolle, S. Bouillon, T. Fichefet, H. Goosse, O. Lecomte, M. Morales Maqueda, and G. Madec. The Louvain-la-Neuve sea ice model. *Notes du pole de modélisation, Institut Pierre-Simon Laplace (IPSL), Paris, France*, (31), 2012.

[102] M. Vancoppenolle, T. Fichefet, and C. M. Bitz. On the sensitivity of undeformed Arctic sea ice to its vertical salinity profile. *Geophysical Research Letters*, 32(16), 2005.

[103] K. Wang, J. Debernard, A. K. Sperrevik, P. E. Isachsen, and T. Lavergne. A combined optimal interpolation and nudging scheme to assimilate OSISAF sea-ice concentration into ROMS. *Annals of Glaciology*, 54(62):8–12, 2013.

[104] A. V. Wilchinsky and D. L. Feltham. Modelling the rheology of sea ice as a collection of diamond-shaped floes. *Journal of Non-newtonian Fluid Mechanics*, 138(1):22–32, 2006.

[105] J. Xie, F. Counillon, L. Bertino, X. Tian-Kunze, and L. Kaleschke. Benefits of assimilating thin sea ice thickness from SMOS into the TOPAZ system. *Cryosphere*, 10(6):2745, 2016.

[106] Q. Yang, S. N. Losa, M. Losch, X. Tian-Kunze, L. Nerger, J. Liu, L. Kaleschke, and Z. Zhang. Assimilating SMOS sea ice thickness into a coupled ice-ocean model using a local SEIK filter. *Journal of Geophysical Research: Oceans*, 119(10):6680–6692, 2014.

[107] Y. Yu and D. Rothrock. Thin ice thickness from satellite thermal imagery. *Journal of Geophysical Research: Oceans*, 101(C11):25753–25766, 1996.

Chapter 3

Implementation of a Sea Ice Model on a Regional High-Resolution Scale

3.1 Overview

This chapter discusses the implementation of the Los Alamos sea ice model, CICE, on a regional high-resolution scale. The CICE model, which is part of the global ice-ocean modeling framework, has been implemented in a standalone (uncoupled from ocean/atmospheric models) mode using ocean and atmospheric forcing derived from Climate Forecast System Reanalysis (CFSR), World Ocean Atlas (WOA) and North American Regional Reanalysis (NARR) data. Implementation of a regional domain requires the adaptation of open boundary conditions, assumptions of no ice state initial conditions and a mixed layer criterion for the slab ocean mixed layer

model. The resulting ice concentration is compared with ice concentrations from AMSR-E and OSI SAF and validated using statistical anomalies, means, and standard deviations. Ice thickness is compared visually with the thickness estimates derived from SMOS sensor.

3.2 Introduction

Several coupled and stand-alone ice models were available for numerical simulation studies at both regional and global scales and have been discussed in Section 2.4. A coupled ice-ocean model is a more complex system requiring additional computational time, parameter tuning, and management of large data quantities. With the availability of high-resolution atmospheric and ocean data from satellite observations, reanalysis and forecast models, we attempt to implement a high-resolution uncoupled sea ice model on a regional scale. We use the Los Alamos sea ice model (CICE), which is also the sea ice component of atmosphere-land-ice-ocean coupled models such as CCSM and Community Earth System Model (CESM). The sea ice components of other ocean models such as ROMS closely follow the physics explained by the CICE model.

CICE [11] is an advanced multi-thickness category sea ice model that has thermodynamic and dynamic components, with ridging, melt pond and biogeochemistry parameterizations. For uncoupled (stand-alone) simulation studies, it includes a slab ocean mixed layer model. It can also be coupled to atmospheric and ocean models like Community Atmosphere Model (CAM), Parallel Ocean Program (POP), NEMO, CCSM, Princeton Ocean Model (POM), and ROMS.

The literature does not provide details and discussion on regional implementation and results for stand-alone models. The 3D-CEMBS is an eco-hydrodynamic model that includes a coupled POP-CICE model for operational forecasting implementation of CICE on a regional scale. The implementation on the regional scale of the ice component and the validation work is still ongoing [7]. The general guidelines for configuring CICE on global and regional scales are already available [11]. The model is available with a displaced pole global grid of 1° and 3° resolution for testing purposes. The model is forced with the default National Centers for Environmental Prediction (NCEP) atmospheric forcing along with the low-resolution CCSM climate runs for ocean fields which include the currents, sea surface slope, salinity, temperature, and ocean heat flux.

3.3 General circulation and ice regimes in the region of interest

The role of ocean currents and salinity in the region is of utmost importance for modeling ice conditions. One of the main outflows from the Arctic Ocean, the Eastern Greenland current, turns northwards at the southern tip of Greenland and flows up to Baffin Bay. A part of the current turns westward into the Davis Strait; the rest re-circulates within the region forming the Baffin Current. A portion of the Arctic surface water enters the region through the Fury and Hecla Strait; part of it forms a cyclonic circulation in Hudson Bay and then exits with the currents from the Foxe Basin, as shown in Figure 3.1 [12, 29, p. 836]. The ice cover in the region consists of

rafted ice floes, level ice with thickness up to 2 m, and multi-year ice in the area of the Canadian Archipelago [12]. Ice conditions in Baffin Bay and surrounding Arctic regions during summer from 1968 to 2010 were investigated by Environment and Climate Change Canada and showed a decline in multi-year ice [8]. Ice thickness in northern Nares Strait varied from 2 to 6 m [16]. Another main feature is the open-water area or polynya known as North Water, which contributes to the ecosystem in the region. The process of warm water upwelling and ice divergence also contributes significantly to ice conditions in the area. Warm water delays freeze-up and ice divergence keep the North Water area ice-free during strong winds [12].

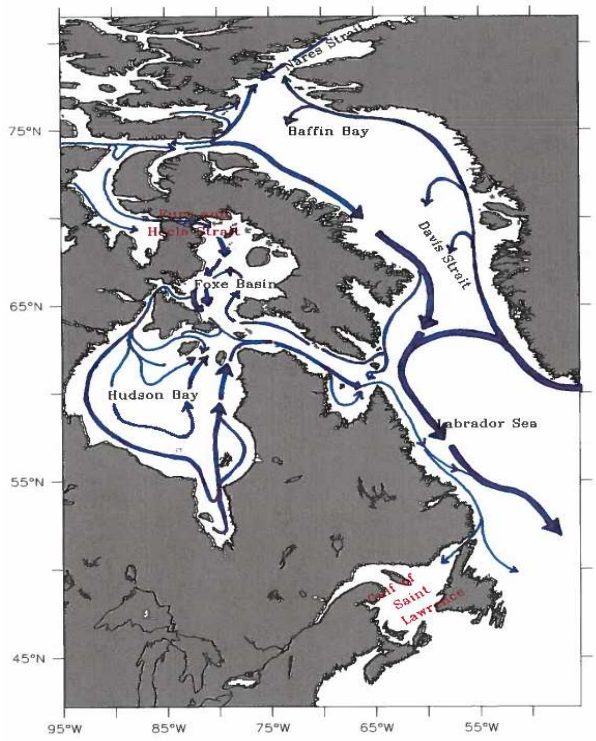

Figure 3.1: General circulation pattern in the domain of interest. Figure is reproduced from [12, 29, p. 836].

A common trend observed in the region was the low extent of sea ice from the beginning of August until the end of September. Sea ice formation starts in the Baffin Bay during October and extends south, with maximum sea ice extent during March extending up to the Gulf of St. Lawrence, and then sea ice gradually begins to melt by the beginning of April. Figure 3.2 shows sea ice concentrations from a monthly climatology (2005-2015) derived from AMSR-E.

3.4 Model configuration

The CICE model has several components:

- Thermodynamic component that computes ice growth and ablation due to vertical heat conductivity, radiative and turbulent fluxes
- Dynamic component that computes the velocity field based on the material strength of the ice
- Transport model that computes advection of tracers such as ice area, ice volume and other tracers
- Ridging model that shifts ice among thickness categories

The heat flux into the ocean surface layer from the ice and open-ocean fractions (all fluxes are positive downwards) is calculated as

$$f_{surf} = (1-a)(f_{sen} + f_{lat} + f_{lwout} + f_{lwin} + f_{swabs}) + a(f_{ice} + f_{swthru}), \qquad (3.1)$$

where f_{sen} is the sensible heat flux between the atmosphere to the open ocean surface; f_{lat} is the latent heat flux between the atmosphere and the open-ocean surface; f_{lwout} is

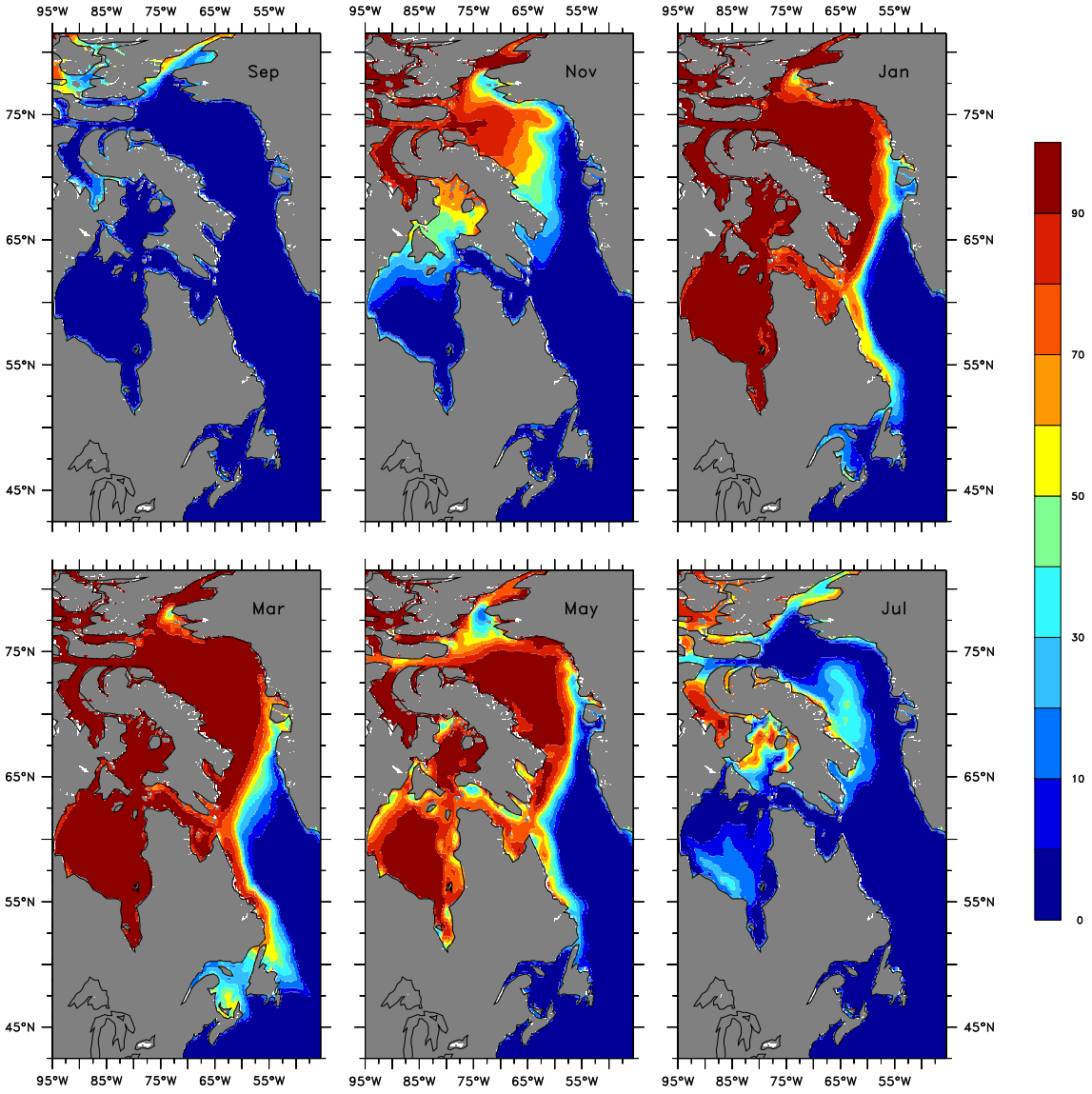

Figure 3.2: Monthly climatology of ice concentration from AMSR-E.

the outgoing longwave radiation from the open-ocean surface to the atmosphere; f_{lwin} is the incoming long-wave radiation; and f_{swabs} is the downward short-wave radiative heat flux calculated as a sum of four radiative categories (direct and diffuse, visible and near-infrared) with varying albedo parameterizations, f_{ice} is the heat flux from the ocean surface to the base of the ice (aggregated over all ice categories/thickness), and f_{swthu} is the short-wave radiative heat flux that passes through the ice and is absorbed by the ocean [11]. Delta-Eddington method [6] was used for computing albedo and short-wave fluxes. The method also considers the effect of ice, snow, change in snow grain radius, and meltponds on albedo [11]. The SST is then computed from

$$\frac{dT}{dt} = \frac{f_{surf} - Q_{mix}}{c_\rho h_{mix}}, \tag{3.2}$$

where, T is the SST, Q_{mix} is the mixed-layer heat flux, c_ρ is the volumetric heat capacity, and h_{mix} is the mixed-layer depth. The potential to freeze or melt ice is then computed from

$$frzmlt = \frac{(T_f - T)c_\rho h_{mix}}{dt}, \tag{3.3}$$

where, the freezing temperature, $T_f = -\mu S$, S is the sea water salinity, and $\mu = 0.054$ is the ratio of freezing temperature of brine to its salinity [5]. New ice is formed when the ocean temperature falls below freezing. If $frzmlt$ is positive, new frazil ice of $0.05m$ is added to the thinnest ice category; if it is negative, then it is used to heat already existing ice. CICE assumes a default value of $20m$ for the mixed-layer depth h_{mix} and fixed value of 0 W/m^2 for Q_{mix}.

The growth and melt of sea ice are calculated by computing new temperatures and rate of melting at the top and bottom of ice [5] by assuming a fixed vertical salinity profile [5]. If there is latent heat transfer from the ice to atmosphere i.e., the

latent heat flux is negative then snow or snow-free ice sublimates at the top surface. If latent heat flux is positive then vapor from the atmosphere is deposited at the surface as snow or ice.

The thickness change is given by

$$(\rho L_v - q)\delta h = f_{lat}\Delta t, \tag{3.4}$$

where ρ is the density of the snow or ice, and $L_v = 2.50110^6$ J/kg is the latent heat of vaporization of liquid water at 0° C, q is the enthalpy of surface ice or snow.

The present configuration considers a constant thermal conductivity of snow (0.25 W/m/deg), while the thermal conductivity of ice, K_i, is parametrised based on the "bubbly" brine model of [25] by

$$K_i = \rho_i/\rho_0(2.11 - 0.11T_i + 0.09S_i/T_i), \tag{3.5}$$

where ρ_i is the density of sea ice ($917Kg/m^3$), ρ_0 is the density of pure ice ($917Kg/m^3$). S_i and T_i are the internal ice Salinity and Temperature.

Growth and melt at the bottom are given by

$$q\delta h = (f_{cb} - f_b)\Delta t, \tag{3.6}$$

where f_{cb} is conductive heat flux at the bottom surface and f_b is the net downward heat flux from the ice to the ocean, f_b is given by

$$f_b = \rho_w c_w D_w u^*(T - T_f), \tag{3.7}$$

where $\rho_w = 1026\ kg/m^3$ is the density of seawater, $c_w = 4218J/kg/K$ is the specific heat of seawater, D_w is the ice-ocean drag coefficient given by equation (3.22), and u^* is the friction velocity.

Since the thermodynamic and dynamic properties of sea ice depend on the amount of ice in each thickness category [9, 23] the basic problem of sea ice modeling is to describe the evolution of ice thickness distribution (ITD) [30] given by equation

$$\frac{\partial g}{\partial t} + \nabla \cdot (g\mathbf{u}) + \frac{\partial}{\partial h}(fg) = \psi, \tag{3.8}$$

where $\mathbf{u}$ is the horizontal ice velocity, $\nabla = (\frac{\partial}{\partial x}, \frac{\partial}{\partial y})$, ψ is the ridging redistribution function, f is the rate of thermodynamic ice growth and g is the ice thickness distribution function, $g(\mathbf{x}, h, t)dh$, defined as the fractional area covered by ice in the thickness range $(h, h + dh)$ at a given time and location. The equation (3.8) is solved in several stages by operator splitting and by partitioning the ice pack in each grid cell into discrete thickness categories [11]. The model configuration presented in this chapter uses seven thickness categories and a single category for open water for approximating the ice thickness distribution. The category lower bounds used are shown in Table 3.1;

Table 3.1: Lower boundary values for thickness categories

Thickness categories	1	2	3	4	5	6	7
Lower bounds (m)	0.00	0.1	0.15	0.30	0.75	1.20	2.00

The conservation equation or the horizontal transport of ice area after neglecting the thermodynamics and the ridging distribution is given by

$$\frac{\partial a_n}{\partial t} + \nabla \cdot (a_n\mathbf{u}) = 0, \tag{3.9}$$

where a_n is the ice area fraction in each category and $\mathbf{u}$ is the ice velocity. Similary,

the conservation equations [11] for ice volume, v_{in}, and snow volume, v_{sn} are given by

$$\begin{aligned} \frac{\partial v_{in}}{\partial t} + \nabla \cdot (v_{in}\mathbf{u}) &= 0, \\ \frac{\partial v_{sn}}{\partial t} + \nabla \cdot (v_{sn}\mathbf{u}) &= 0. \end{aligned} \tag{3.10}$$

Conservation equations for ice energy e_{in} and snow energy e_{sn} and the dependent tracers such as level (non-deformed) ice fraction $a_{lvl}a_n$, pond ice fraction $a_{pnd}a_{lvl}a_n$, pond volume $h_{pnd}a_{pnd}a_{lvl}a_n$, pond ice volume $h_{ipnd}a_{pnd}a_{lvl}a_n$ are simlar to the equations (3.9) [11]. See AppendixA.1 for the equations on dependent tracers . The incremental remapping scheme by [19] is used to solve the continuity or transport equations in each thickness category.

The equation for transport in thickness space [11] is obtained after neglecting the second term on the left-hand side and term on the right-hand-side of equation (3.8) given by

$$\frac{\partial g}{\partial t} + \frac{\partial}{\partial h}(fg) = 0, \tag{3.11}$$

and is solved using linear remapping scheme for ice thickness simulation [18].

Afterwards, the term on the right-hand side, ψ, of the equation (3.8) that describes the redistribution of ice in thickness space due to the mechanical process of ridging is solved. The ridging scheme has four components: "(1) A rule for computing the rates of opening, closing, and ridging (2) A function, $p(h)$, that describes the thickness distribution of ice participating in ridging, given $g(h)$. (3) A function, $n(h)$, that describes the thickness distribution of the resulting ridged ice, given $p(h)$; and (4) a procedure for computing the ice strength P, given $p(h)$ and mean thickness h [20]."

The ridging function requires that when ice diverges and leaves a given region, ice must be replaced with open water. When the pack ice converges, the ridging

must reduce the open water area and deform thin ice into thick ridges. The shear ridging function may generate a combination of opening, closing, and ridging. Also, the strain rate, ψ, must enforce conservation of area and volume [20, 11]. In order to satisfy these criteria ψ [20] is defined by

$$\psi = |\dot{\epsilon}|[\alpha_0(\theta)\delta(h) + \alpha_r(\theta)w_r], \tag{3.12}$$

where $\dot{\epsilon}$ is the strain rate magnitude, θ gives the relative contributions of divergence and shear ($\theta = 0,\pi/2$, and π for pure divergence, shear, and convergence, respectively), δ denotes the delta fuction at $h = 0$, α_0,α_r are coefficients for opening and ridging/closing, respectively, w_r is the ridging mode which must enforce the conservation of area and volume [20, 11] and is given by

$$w_r = \frac{-p(h) + n(h)}{N}, \tag{3.13}$$

where $p(h)$ is the function that describes the ice participating in riding, given by equation (3.14) and $n(h)$ is the ITD of the resulting ridged ice, and N is a normalization factor required to conserve area [20, 11]. $p(h)$ is given by

$$p(h) = b(h)g(h), \tag{3.14}$$

where $b(h)$ is a weighing function that favours ridging of thin ice and closing of open water in preference to ridging of thicker ice. To ensure numerical stability the weighting function given by equation (3.15) [20, 11] is used for the present configuration of the model.

$$b(h) = \frac{e^{[G(h)/a^*]}}{a^*[1 - e^{(-1/a^*)}]}, \tag{3.15}$$

where $G(h)$ is the fractional area covered by ice thinner than h and a^* is an emperical constant (0.05).

The ITD of newly formed ice ridges, $n(h)$ in equation (3.13) is given by

$$n(h) = \int_0^\infty a(h_1)\gamma(h_1, h)dh_1, \tag{3.16}$$

where $\gamma(h_1, h)dh$ is the ice area ridged to the thickness interval $(h, h + dh)$ per unit area lost by ice of thickness h_1. γ, the ITD of ridges is approximated by [20]

$$\gamma_n(h) = \begin{cases} \gamma_{0_n} e^{[-(h-H_{min})/\lambda]} & h \geq H_{min}, \\ 0 & h < H_{min}, \end{cases} \tag{3.17}$$

where λ is an empirical e-folding scale and $H_{min} = 2h_n$ (where h_n is the thickness of ridging ice, γ_{0_n} is a normalization factor.

Finally, the ice strength formulation is given by

$$P = P^* h e^{[-C(1-a_n)]}, \tag{3.18}$$

where $P = 27,500N/m$ and $C = 20$ are empirical constants, and h is the mean ice thickness. The formulation given in equation (3.18) is used since it ensures stability for high resolution models [20].

The dynamics part of the sea ice models predicts the movement of the ice pack based on winds, ocean currents, Coriolis force and a model of the material strength of the ice. The movement of the pack contributes to the thickness and extent. The governing equation of momentum that represents the force balance per unit area in the ice pack is given by

$$m\frac{\partial \mathbf{u}}{\partial t} = \nabla\sigma + \tau_a + \tau_w - \hat{k} \times mf\mathbf{u} - mg\nabla H_o, \tag{3.19}$$

where m is the combined mass of ice and snow per unit area, τ_a and τ_w are wind and ocean stresses, respectively. σ is the ice internal stress, f is the Coriolis parameter,

g is the acceleration due to gravity and H_o is the sea surface slope. The rheology of ice is presented by an alternative relationship between the ice stress and strain rate through ice strength. The present configuration uses the EVP rheology model developed by [10]. The surface currents are used to compute the sea surface slope, ∇H_o, to determine the ice-ocean stress and afterward the ice velocity [11].

The ocean stress is given by

$$\boldsymbol{\tau}_w = D_w \rho_w |\boldsymbol{U_w} - \boldsymbol{u}|[(\boldsymbol{U_w} - \mathbf{u})\cos\theta + \hat{k} \times (\mathbf{U_w} - \boldsymbol{u})\sin\theta], \tag{3.20}$$

where D_w is the ocean drag coefficient, ρ_w is the sea water density, $\boldsymbol{U_w}$ is the surface currents, $\boldsymbol{u}$ is the ice velocity and θ is the turning angle. Since the ocean currents are used in the present configuration the turning angle, θ, is zero.

The wind stress $\boldsymbol{\tau}_a$ is determined from

$$\boldsymbol{\tau}_a = \frac{\rho_a {u^*}^2 \boldsymbol{U_a}}{|\boldsymbol{U_a}|}, \tag{3.21}$$

where ρ_a is the air density, U_a is the wind component, and u^* is the friction velocity [1]. A variable drag coefficient suggested by [35] has been used in the configuration since it produces more realistic ice concentration and thickness in the Arctic with respect to the constant drag coefficients [35]. The drag, D_w, is estimated from properties of the ice cover such as ice concentration, vertical extent and area of the ridges, and floe size [21, 22] as

$$D_w = D_{keel} + D_{floe} + D_{skin}, \tag{3.22}$$

where D_{keel} is the contribution from keels, D_{floe} is the contribution from floe edges, D_{skin} is the contribution from the ice-ocean boundary.

All the equations were spatially discretized on a non-rotated orthogonal Arakawa B-grid [2]. Ice thickness, snow area, volume, energy, and thermodynamic variables

such as temperature were defined at the center of the grid cell while the velocities were defined at the corners and were aligned along the grid lines [11]. The results of this study were discussed for a model resolution of almost-identical 10-km grid cells. The open boundaries were implemented by restoring the non-land halo (ghost) cells along the grid edge to specified values. For domain decomposition each local domain had one ghost (halo) cell on each side which communicates with one another. Halo cells duplicate the subset of neighbour cells that each iteration depends on. For the mixed-layer slab ocean model, the boundary conditions for SST were achieved by restoring it towards a monthly climatology. The ice concentration, volume, and snow volume were restored to the initial timestep [11].

3.5 Forcing data

Atmospheric parameters were derived from a high-resolution climate data set for the North American Domain, NARR [24] obtained from NCEP reanalysis data provided by the NOAA/OAR/ESRL PSD were used for forcing the model; see AppendixA.2 for data sources. The data includes air density, zonal wind speed, meridional wind speed, air temperature, specific humidity, precipitation, cloud fraction, and incoming short-wave radiation. The NARR data are of high temporal (eight times daily) and spatial ($0.3^\circ \times 0.3^\circ$) resolution. Ocean currents were obtained from the CFSR monthly climatology data, see AppendixA.2 for data source. A fixed ocean salinity profile was derived from monthly climatology data, World Ocean Atlas 2013 ($0.25^\circ \times 0.25^\circ$) [17]. SST is derived from monthly climatology derived from high-resolution data provided by NOAA/OAR/ESRL PSD [26], see AppendixA.2 for data source. The ocean data

were processed to be consistent with the masking used for the high-resolution model. The missing values near coastal areas were replaced by a 5 point average of the respective data. The mixed layer depth (MLD) is calculated from WOA-2013 monthly climatology using fixed threshold density criteria as

$$h_{mix} = \text{depth where}(\sigma_\theta = \sigma_\theta|_{10} \pm 0.2\text{Kg/m}^3), \tag{3.23}$$

where σ_θ is the potential density, $\sigma_\theta|_{10}$ is the potential density at 10 m depth. If the mixed-layer depth is greater than the bathymetry, then the mixed-layer depth is relaxed to the bathymetry value at the grid cell. The mixed-layer heat flux is assumed to be zero. Also, a minimal mixed layer depth of 10 m is maintained for all computations. There are several formulations for mixed-layer depth computation, e.g., the French Research Institute for the exploration of the sea (Ifremer) uses a density criterion of 0.03. For the following experiments, the equation (3.23) was used to compute the MLD in equations (3.2) and (3.3).

3.6 Remote sensing data for validation

Remote sensing data were used for the validation of ice parameters estimated by the model. Ice concentration derived from AMSR-E of resolution 6×4 km [29] were used for validation of model estimated ice concentration. AMSR-E was developed by JAXA, and was deployed on Aqua satellite. AMSR-E and AMSR2 are passive sensors that look at the emitted or reflected microwave radiation from the earth's surface with multiple frequency bands. The vertical (V) and horizontal (H) polarization channels near 89 GHz were used to compute the ice concentration from AMSR-E [29]. The Arctic Radiation and Turbulence Interaction STudy (ARTIST) Sea Ice

algorithm used to determine ice concentration from AMSR-E show excellent results above 65% ice concentration where the error does not exceed 10%. With low ice concentrations, substantial deviations can occur depending on atmospheric conditions [29]. The parameters of the sensor are provided in Table 3.2. AMSR-E ice concentration were available from January 2005 to September 2011, after which it stopped functioning. From August 2012 AMSR2 had been used for data collection. The same frequency (89 GHz) as that of the AMSR-E instrument was used to derive information from AMSR2. The spatial resolutions also remain the same for both AMSR-E and AMSR2. The same algorithm was applied to derive ice concentrations from both AMSR-E and AMSR2. Also, the sea ice concentration product from Ocean and Sea Ice Satellite Application Facility (OSI SAF) - EUMETSAT of 10-km resolution were used for comparison [34]. OSI SAF product was derived from Special Sensor Microwave Imager Sounder (SSMIS) [34, 4]. The data were available on a 10 km polar stereographic grid and were derived from 19 V, 37 VH channels, see Table 3.2 for sensor specifications.

Table 3.2: Specifications of microwave radiometers used to estimate ice concentration.

Specifications	AMSR-E/AMSR2	SSMIS	
Center Frequency, GHz	89	19	37
Mean Spatial resolution, km	5.4	69×43	37×28
Polarization	HV	V	HV
Incidence angle, deg	55	50	
Swath, km	1445	1700	
Data availability, month/year	08/2002 − 10/2011/08/2012-present	03/2005−Present	

For ice thickness, data of resolution 35 to 50 km derived from the SMOS Microwave Imaging Radiometer with Aperture Synthesis (MIRAS) instrument (1.4-GHz channel) [14] was used. The ice thickness uncertainties were lower for thin ice and uncertainty increased as the thickness increased. SMOS data are available from 15 October 2010. The presence of snow accumulated over months also can increase the uncertainty. The uncertainty of SMOS ice thickness (observation) includes the error contributions caused by the brightness temperature, ice temperature and ice salinity, See Table3.4 [31, 27, 33, 32]. The insufficient knowledge on the snow cover also introduces a large uncertainty in the thickness estimates from SMOS. Moreover, large errors occur during the melting period. In general, the uncertainty of thickness observation increased with increasing ice thickness, increasing snow cover and onset of melt [13]. The SMOS ice thickness retrieval produces large uncertainty during the melt season and hence retrieval was not conducted during the melt season. Therefore, data from April to October were not available for our region of interest. Refer to Table 3.3 [15, 3] for details on SMOS sensor.

Table 3.3: SMOS sensor specifications.

Polarization	HV
Incidence angle	$0 - 55^{\circ}$
Swath, km	900
Center Frequency (GHz)	1.4 (L-band)
Mean Spatial resolution (km)	$30 - 50$
Radiometric sensitivity over ocean, K	2.5 and 4.1

Table 3.4: SMOS uncertainties caused by brightness temperature, ice temperature, and ice salinity.

Ice thickness	Uncertainty caused by a standard deviation of		
	0.5 K brightness temperature	1 K ice tempearture	1 g/Kg ice salinity
0 -10 cm	$<$ 1 cm	$<$ 1cm	$<$ 1cm
10-30 cm	$<$ 1 cm	1-5 cm	1- 13 cm
30-50 cm	1-4 cm	2-10 cm	2-22 cm
$>$ 50 cm	$>$ 4cm	$>$ 7cm	$\leq$ 40 cm

Data derived from AVHRR were used for sea surface temperature (SST) comparison [26, 28]. SST data products were generated using a combination of satellite and in situ observations from buoy and ship observations and were available on a $(0.25^\circ \times 0.25^\circ)$ resolution.

3.7 Results and validation

3.7.1 Ice concentration

For consistency in the analysis, model and observations were interpolated to a grid resolution of 10 km. The data points missing in the observation, either temporal or spatial, were considered as missing points in the model estimates too. Thus, model and observations had same temporal and spatial data gaps.

Different algorithms have been tested to derive sea ice concentration from AMSR-E channels. These algorithms have been validated with visual inspections from cruise

data. The algorithm shows relevant results at mid and high ice concentrations of above 65%. The error does not exceed 10% in such regions. Significant deviations may occur in the areas with low ice concentration depending on the atmospheric conditions [29].

OSI SAF data was defined based on the confidence level of the probability of sea ice presence. The confidence levels of OSI SAF are defined as Unprocessed (No data), Erroneous (computation failed), Unreliable ($50-74\%$ probability), Acceptable ($75-94\%$ probability), Good ($95-98\%$ probability), and Excellent ($99-100\%$ probability) [34]. For analysis, the acceptable, good and excellent data have been used. The rest of the grid cells were treated as missing points both in observation and model estimated values.

The simulation studies were initiated with a no-ice state assumption from 1 September 2004. The model was integrated from this initial date to 31 December 2015. Figure 3.3 shows the results for three years of simulation from 01 January 2005 to 31 December 2007. The model was numerically stable and simulates physically realistic values for the ice parameters in the region. The maximum values of ice speed and strength did not exceed 1 m/s and 1000 kN, which showed consistency with the conditions for numerical stability [20]. The ice concentration is zero during August and September; increasing gradually to high ice concentration over the domain during February and March and then decreasing gradually to a no-ice condition.

Figure 3.4 shows the spatial root mean square error (RMSE) of the model with the observed ice concentrations from AMSR-E and OSI SAF, and model SST with the SST derived from AVHRR. The RMSE was calculated from the daily climatology value of the model estimates and the observation. RMSE was below 15% for ice

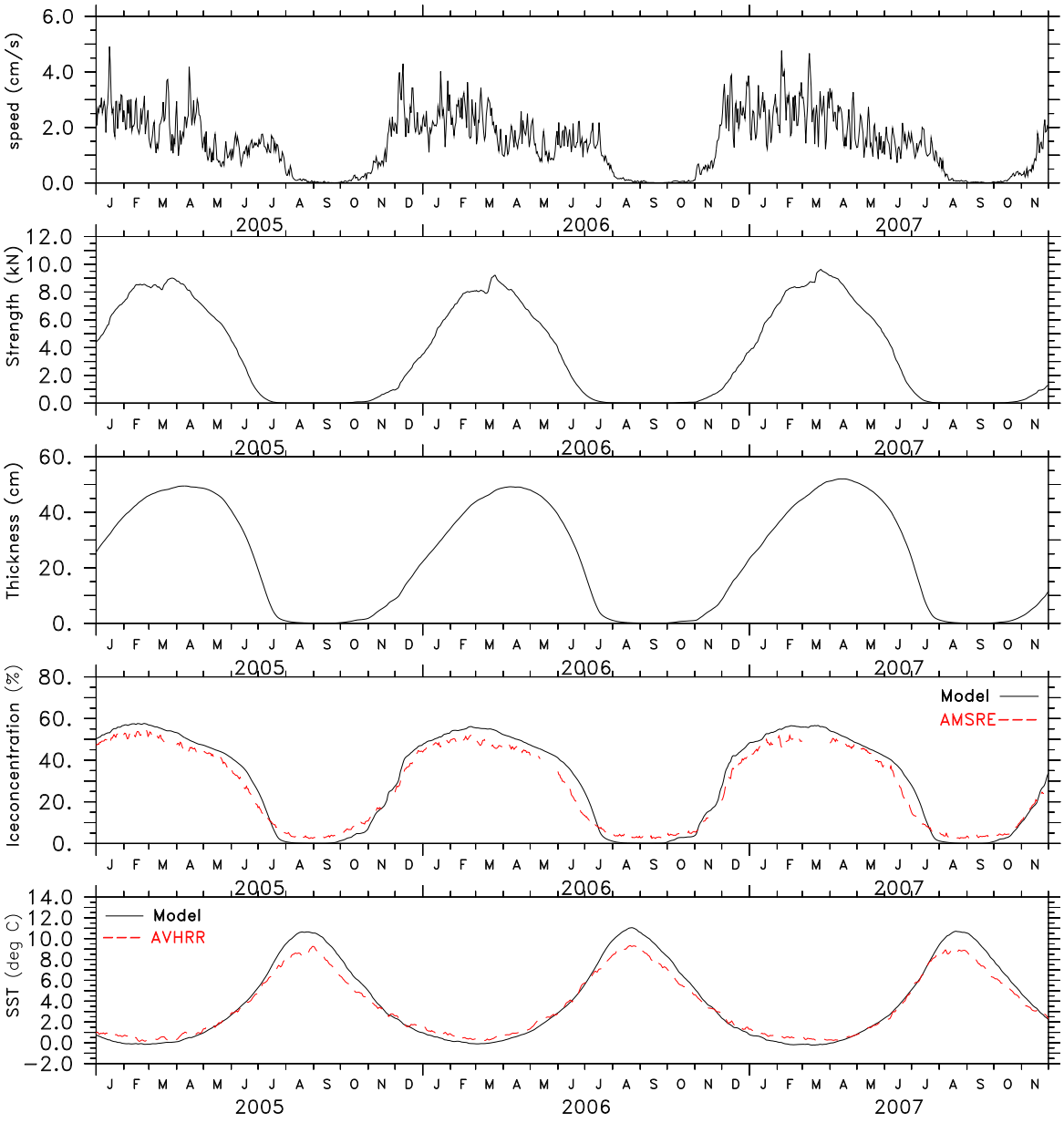

Figure 3.3: The average ice speed, strength, thickness, and concentration in the domain of interest.

concentration except during May, June, and July and RMSE are below 1° for SST except during June, July, and August. The error in SST was due to the assumption of zero mixed layer heat flux. When ice is formed, the mixed layer heat flux melts the ice from below thus constraining the ice growth. The absence of the mixed layer heat flux contributes to the error in the ice concentration. The model tends to accumulate errors after certain period of time due to the averaging of forcing data. When ice starts to melt the error was increasing even more because melting processes depend on particular weather and ocean parameters which were not considered during modeling due to the complexity and unavailability.

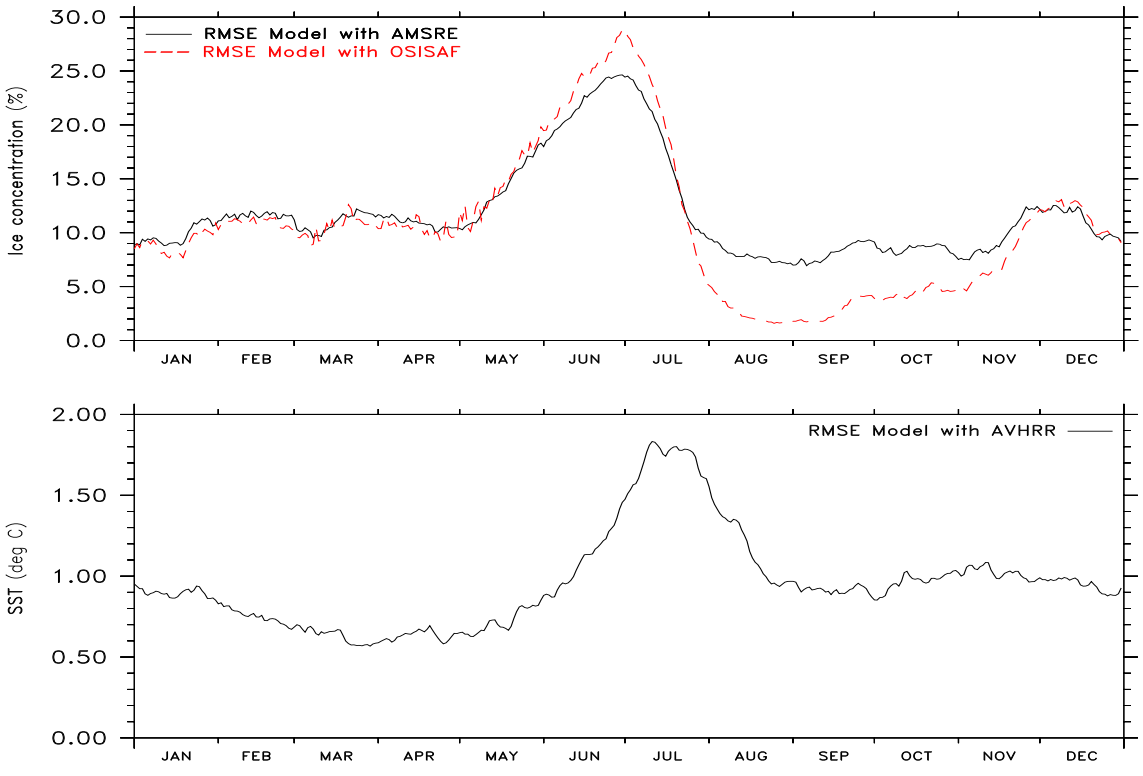

Figure 3.4: Root mean square error, ice concentration and SST.

The monthly anomaly of the ice concentration from the model and AMSR-E observation is shown in Figure 3.5 and the monthly anomaly of the ice concentration from the model and OSI SAF observation are shown in Figure 3.6. The ice concentration anomalies from both the model and observation lie between -10% and 6%. The monthly anomaly of the SST from the model and AVHRR observation are shown in Figure 3.7. SST anomalies lie between $-0.8°$C and $1°$C. The reason for variation of ice concentration anomaly during 2006, 2009, 2014 may be attributed due to the anomaly observed in the SST and also the snow thickness estimated from the model. The ocean sub-mixed layer heat flux, Q_{mix} (see equation (3.2)) was assumed zero in the model configuration. The mixed layer heat flux is usually negative during winter and positive during summer months, thus maintaining a summer warmer layer below the mixed layer during winter which would hinder the growth of ice; and winter cold layer below the mixed layer during summer which delays the melt. Since this heat flux is absent, it contributes to the anomaly variation. Moreover, the model also shows lower snow depth and high thickness during the years 2006, 2009, and 2014 of anomaly variations, see Figures 3.8, 3.9. The lower snow depth would lead to higher ice thickness and the mixed layer heat flux, if present, would be acting to reduce the thickness and area. Also, the contribution of errors from the observations may not be neglected in these variations.

The seasonal average of the model and the observation were used to compute the absolute error; see Figure 3.10 for the absolute error of the ice concentration between the model and AMSR-E. From December to May, the model errors were high along the Davis Strait where the Greenland currents turn westward and form the Labrador currents. The exchange of hot and cold waters in the region was not well represented

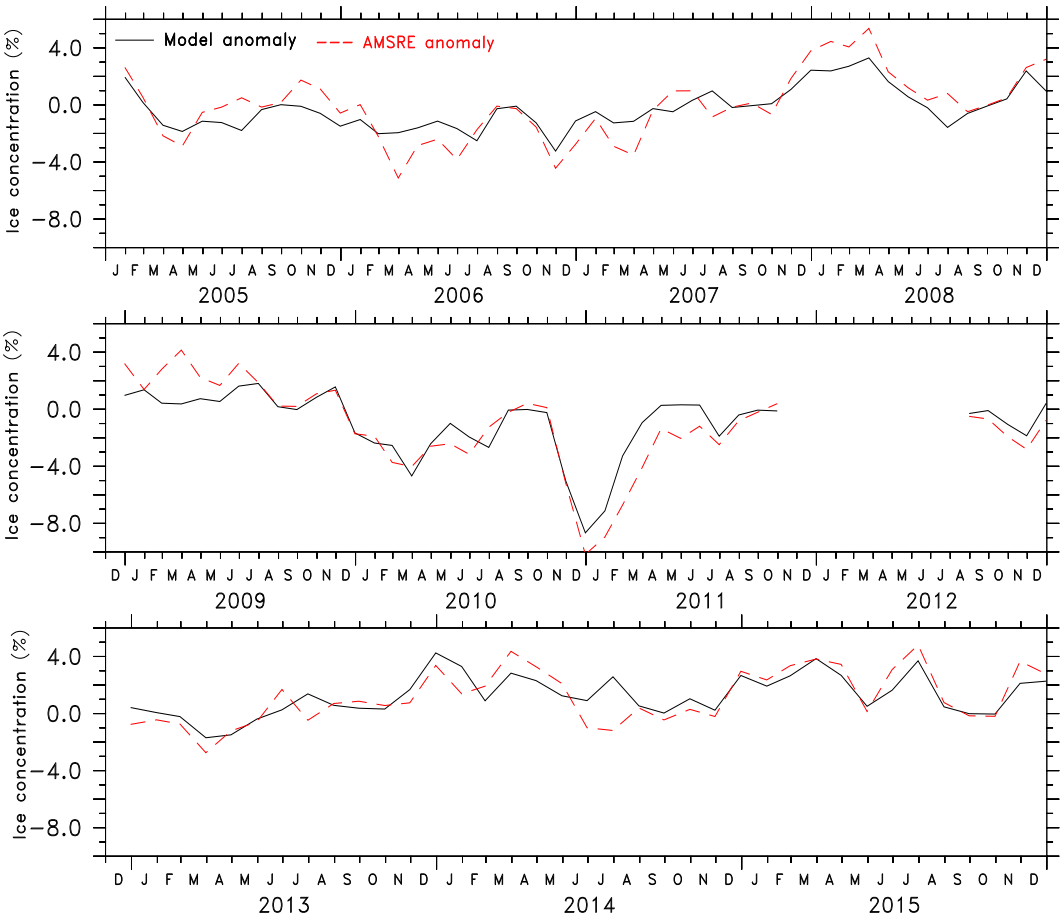

Figure 3.5: Anomaly of Model ice concentration and AMSR-E.

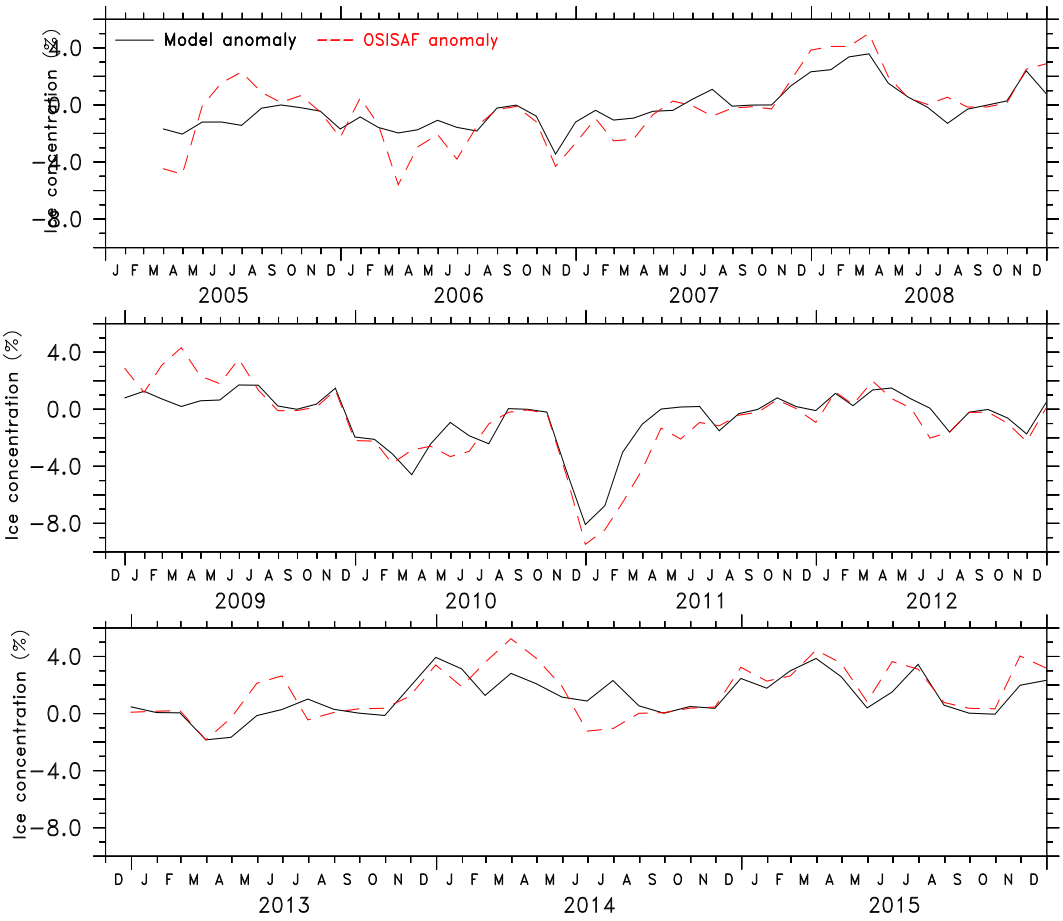

Figure 3.6: Anomaly of Model ice concentration and OSI SAF.

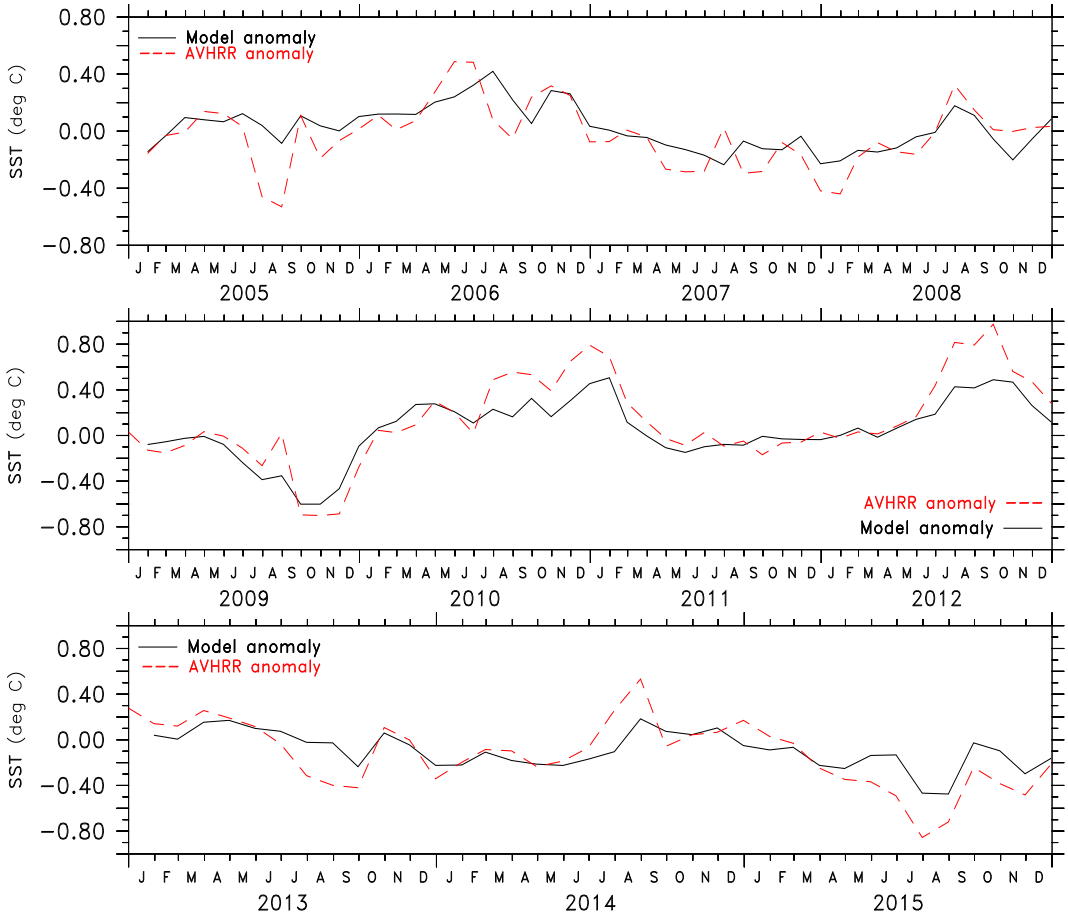

Figure 3.7: Anomaly of Model SST and AVHRR.

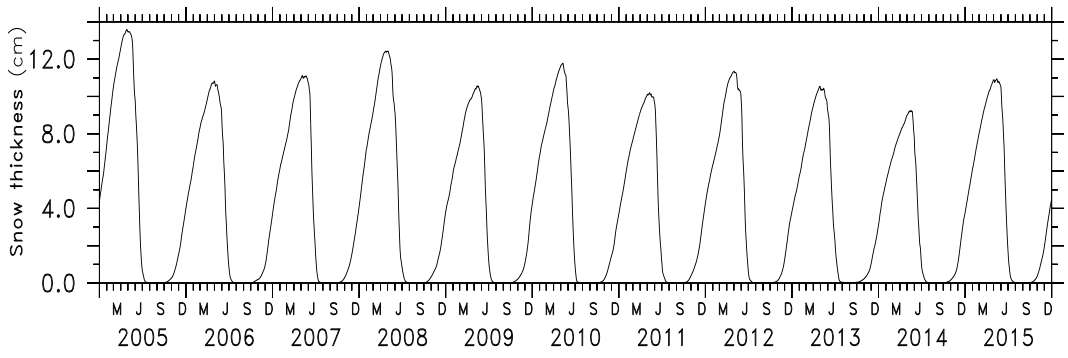

Figure 3.8: Snow thickness (cm) from the model.

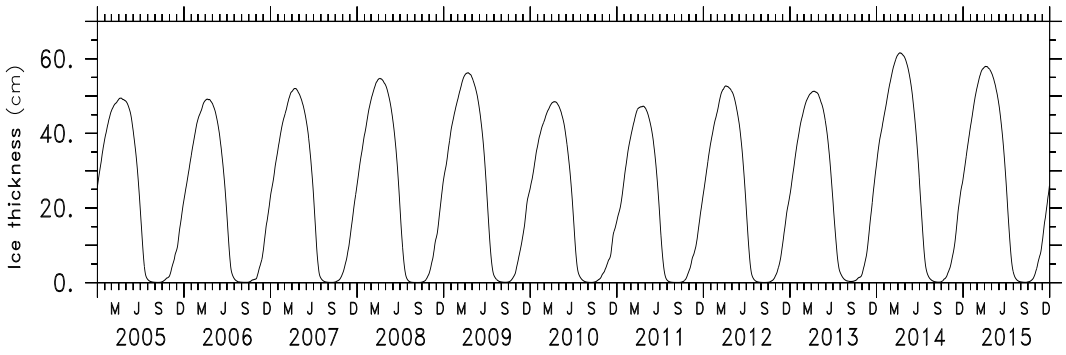

Figure 3.9: Ice thickness (cm) from the model.

in the model. The error in the North Water polynya is also due to the lack of heat flux contribution and also from the CFSR currents that are of low resolution and are not well presented in the Nares Strait, Fury and Hecla Strait (Figure 3.12). From June to August, the error is high in Baffin Bay and Hudson Bay. A similar result is shown by the absolute error between the model and OSI SAF data except that from December to May the error distribution is below 15% in Hudson Bay (Figure 3.11).

3.7.2 Ice thickness

Figure 3.13 shows the simulation result for ice thickness in cm. Only the results from the northern part of the domain that includes the Baffin Bay is shown in Figure 3.13. The first column in the figure illustrates the ice concentration from AMSR-E. The second column shows the ice thickness from the model and the third column shows the thickness estimates from SMOS. The ice thickness retrieval algorithm from SMOS assumes 100% ice concentration which leads to an underestimation of ice thickness for the grid cells with ice concentration less than 100%. The thickness estimates in

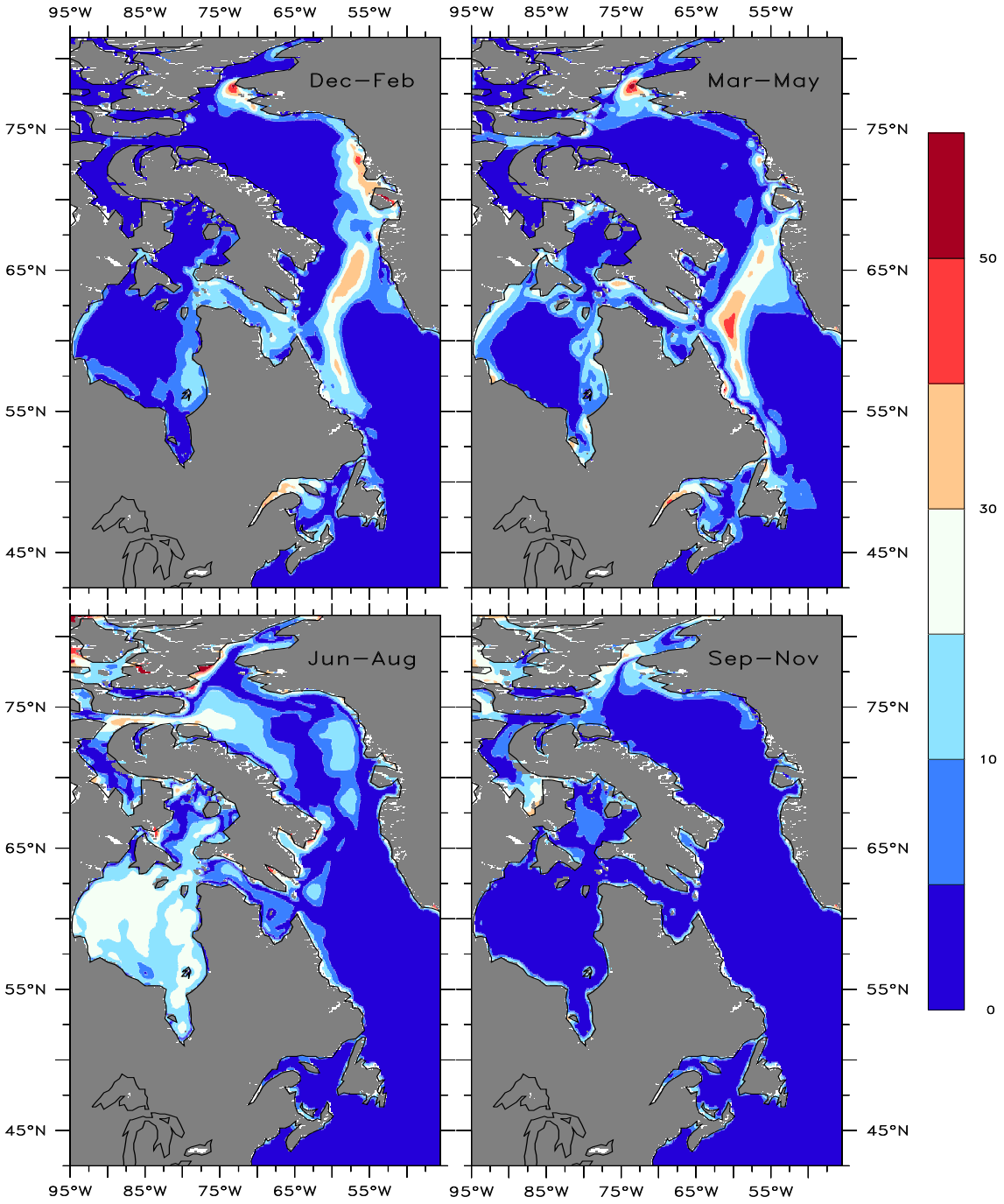

Figure 3.10: Absolute error of ice concentration from Model and AMSR-E (%).

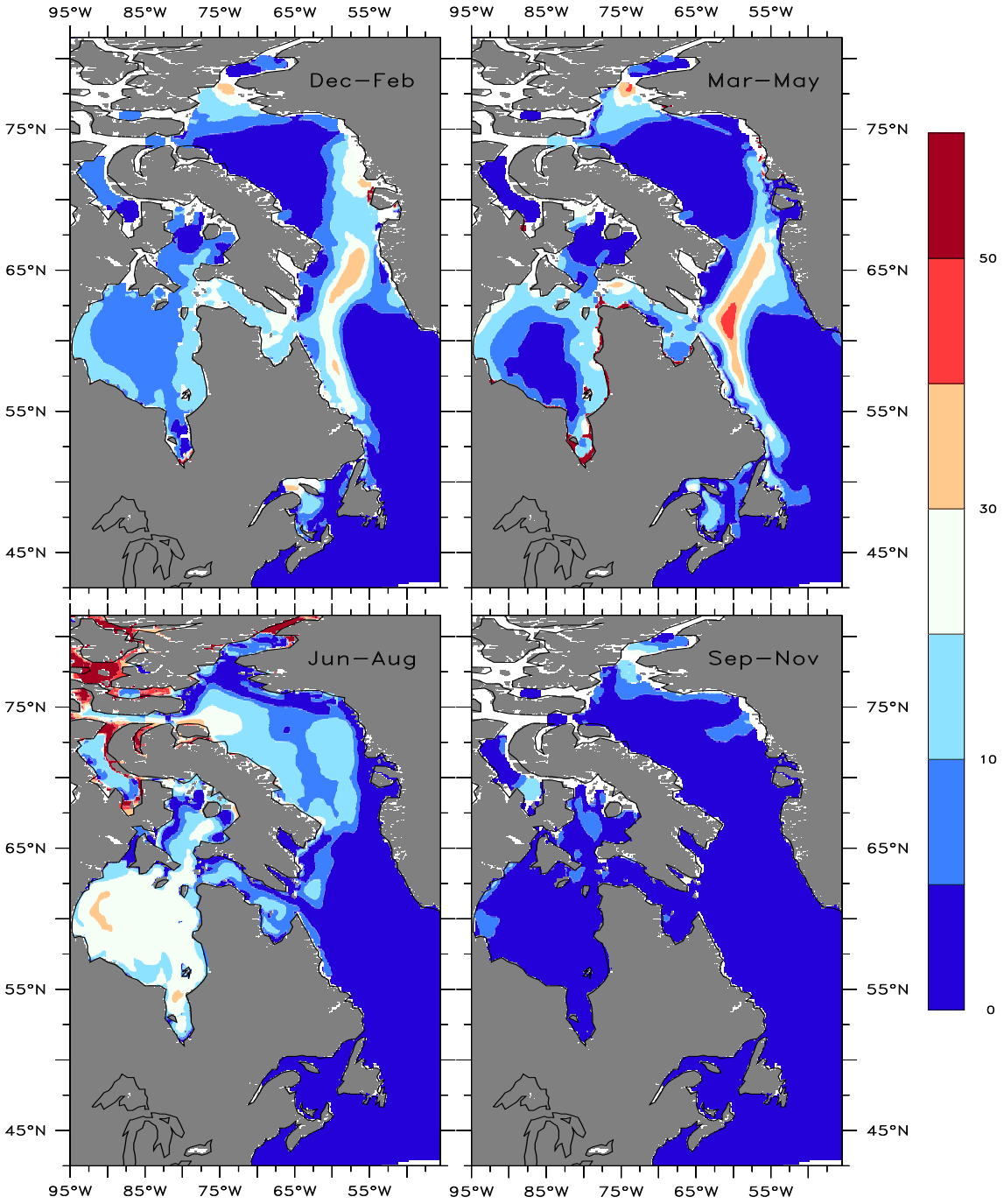

Figure 3.11: Absolute error of ice concentration from Model and OSI SAF (%).

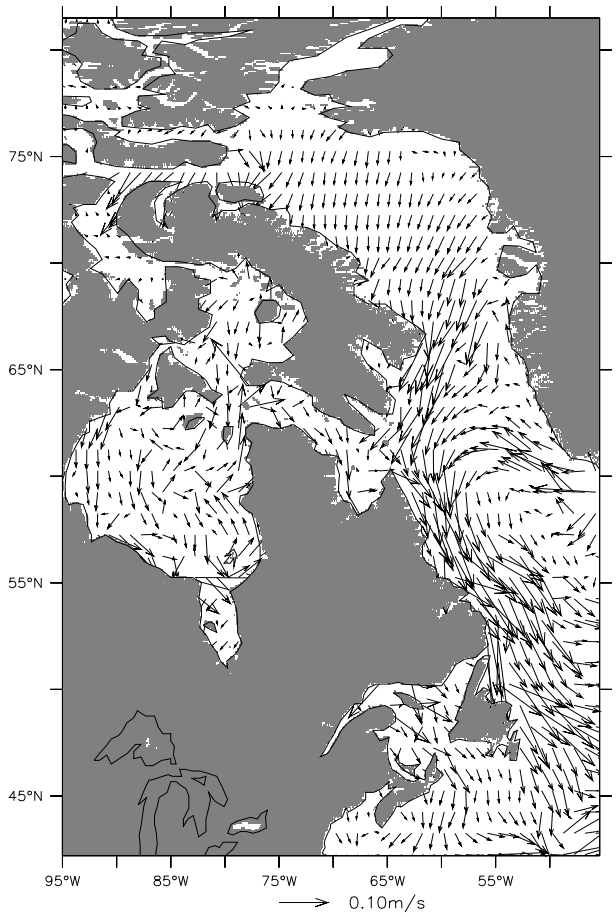

Figure 3.12: Multi-year mean of currents from CFSR.

the Baffin region are overlaid with contour levels for a better understanding of the pattern. During October and December the contours of 30 cm ice thickness from model and SMOS shows a good match. During February the the contour level of 70 cm ice thickness from model shows a good match with the ice thickness retrieved from SMOS. The thickness error for observed data is smaller for thin ice and may go up to 100% for thickness greater than half a meter, see Table3.4 [13]. Considering the uncertainty levels in SMOS derived measures the modeled ice thickness is a good estimate of the observation.

3.8 Conclusions

The high-resolution, regional-scale CICE model was implemented for the Baffin Bay, Hudson Bay, Labrador Sea and Gulf of St. Lawrence in a stand-alone mode with NARR high-resolution atmospheric forcing (reanalysis) data and ocean parameters derived from CFSR and WOA 2013. The model CICE is typically implemented on a tripolar or dipole grid configurations and with cyclic/closed boundaries for global ice-ocean framework. For the configuration on a regional domain, the model was implemented on a curvilinear B-grid with open boundaries achieved via restoring the boundary values to the initial values. Also, the model is generally forced using the ocean parameters derived from CCSM simulations or coupled with other ocean models such as NEMO. Here in this work a density based criteria is used for the slab-ocean mixed layer model for stand-alone simulation. The model was initiated from a no ice state condition and evolved over time, simulating sea ice parameters such as ice concentration. The model stability was tested to ensure that the configuration

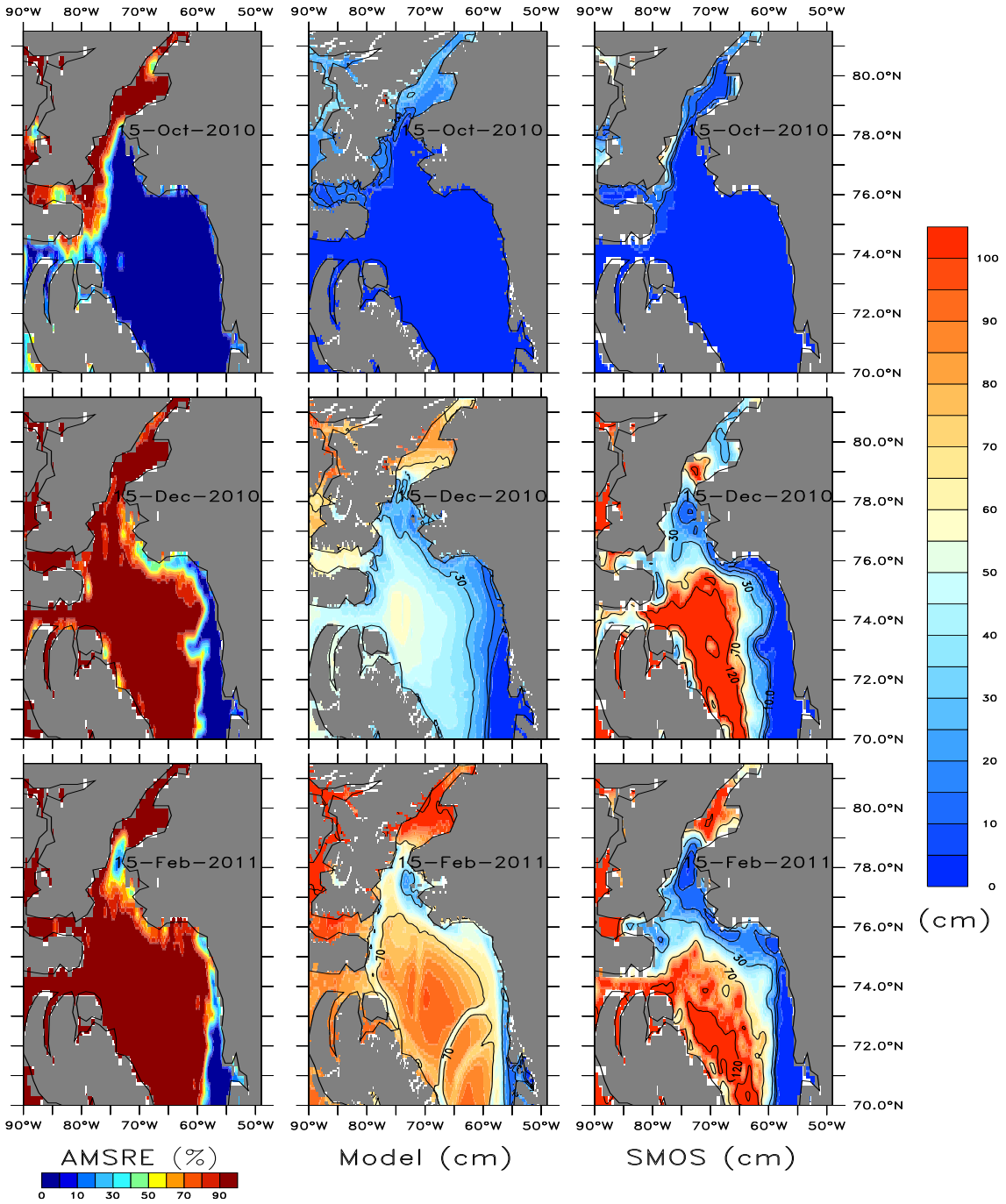

Figure 3.13: Column 1 shows the ice concentration from AMSR-E with the color bar in column 1 showing values of ice concentration in percentage, Column 2 shows the ice thickness from the model and Column 3 shows the ice thickness from SMOS. The color bar on the right represents the ice thickness values in cm.

produces physically realistic values of the sea ice parameters. The advantage of the implemented stand alone model includes the estimation of other sea ice parameters such as thickness, freeboard (discussed in Chapter 4), sail height and keel depth (discussed in Chapter 5) without any additional complexities associated with tuning parameters in a coupled ocean model.

The comparison of the model with the observation data show that the ice concentration spatial RMSE is below 15% except during May, June and July and SST spatial RMSE are below 1°C except during June, and July and August. The monthly anomalies of ice concentration from both the model and observation lie between -10% and 6% and SST anomalies from both the observation and model lie between -0.8°C and 1°C for the entire domain. The absolute error analysis shows that the ice-concentration errors tend to be higher around the North Water Polynya, and the Davis Strait from December to May. During June to August, the large errors were found in the Baffin Bay and Hudson Bay region, with the errors mostly below 30%. The large errors were due to the absence of a mixed layer heat flux in the model, assumptions of constant salinity profile and low-resolution ocean currents. An investigation into options for assimilating SST data to reduce the model error and inclusion of variable salinity, MLD is suggested. The visual comparison of the ice thickness estimates with the SMOS derived values shows good match considering the uncertainty levels of the observed ice thickness.

Bibliography

[1] E. L. Andreas, R. E. Jordan, and A. P. Makshtas. Simulations of snow, ice, and near-surface atmospheric processes on Ice Station Weddell. *Journal of Hydrometeorology*, 5(4):611–624, 2004.

[2] A. Arakawa and V. R. Lamb. Methods of computational physics. *Academic Press*, 17:174–265, 1977.

[3] H. M. Barré, B. Duesmann, and Y. H. Kerr. SMOS: The mission and the system. *IEEE Transactions on Geoscience and Remote Sensing*, 46(3):587–593, 2008.

[4] W. Bell. A preprocessor for SSMIS radiances scientific description. *Met Office, UK*, 2006.

[5] C. M. Bitz and W. H. Lipscomb. An energy-conserving thermodynamic model of sea ice. *Journal of Geophysical Research: Oceans*, 104(C7):15669–15677, 1999.

[6] B. Briegleb and B. Light. A Delta-Eddington multiple scattering parameterization for solar radiation in the sea ice component of the Community Climate System Model. *NCAR Tech. Note NCAR/TN-472+ STR*, pages 1–108, 2007.

[7] L. Dzierzbicka-Glowacka, M. Janecki, A. Nowicki, and J. Jakacki. A new marine ecosystem 3D CEMBS model (version 2) for the Baltic Sea. In *Complex Systems (ICCS), 2012 International Conference on*, pages 1–6. IEEE, 2012.

[8] Environment Canada. Sea ice trends in canada, 2011.

[9] W. Hibler Iii. Modeling a variable thickness sea ice cover. *Monthly weather review*, 108(12):1943–1973, 1980.

[10] E. Hunke and J. Dukowicz. An elastic–viscous–plastic model for sea ice dynamics. *Journal of Physical Oceanography*, 27(9):1849–1867, 1997.

[11] E. C. Hunke, W. H. Lipscomb, A. K. Turner, N. Jeffery, and S. Elliott. CICE: the Los Alamos Sea Ice Model Documentation and Software Users Manual Version 5.1 LA-CC-06-012. *T-3 Fluid Dynamics Group, Los Alamos National Laboratory*, 675, 2015.

[12] R. Ingram and S. Prinsenberg. Coastal oceanography of Hudson Bay and surrounding eastern Canadian Arctic waters. *The Sea*, 11(29):835–859, 1998.

[13] L. Kaleschke, X. Tian-Kunze, N. Maaß, G. Heygster, M. Huntemann, H. Wang, and C. Haas. SMOS Sea Ice Retrieval Study (SMOSIce), ESA Support To Science Element (STSE), Final Report ESA ESTEC contract no. Technical report, 4000101476/10/NL/CT, 2013.

[14] L. Kaleschke, X. Tian-Kunze, N. Maaß, M. Mäkynen, and M. Drusch. Sea ice thickness retrieval from SMOS brightness temperatures during the Arctic freeze-up period. *Geophysical Research Letters*, 39(5), 2012.

[15] Y. H. Kerr, P. Waldteufel, J.-P. Wigneron, J. Martinuzzi, J. Font, and M. Berger. Soil moisture retrieval from space: The Soil Moisture and Ocean Salinity (SMOS) mission. *IEEE transactions on Geoscience and remote sensing*, 39(8):1729–1735, 2001.

[16] R. Kwok. Exchange of sea ice between the Arctic Ocean and the Canadian Arctic Archipelago. *Geophysical Research Letters*, 33(16), 2006.

[17] S. Levitus et al. The world ocean database. *Data Science Journal*, 12:WDS229–WDS234, 2013.

[18] W. H. Lipscomb. Remapping the thickness distribution in sea ice models. *Journal of Geophysical Research: Oceans*, 106(C7):13989–14000, 2001.

[19] W. H. Lipscomb and E. C. Hunke. Modeling sea ice transport using incremental remapping. *Monthly Weather Review*, 132(6):1341–1354, 2004.

[20] W. H. Lipscomb, E. C. Hunke, W. Maslowski, and J. Jakacki. Ridging, strength, and stability in high-resolution sea ice models. *Journal of Geophysical Research: Oceans*, 112(C3), 2007.

[21] P. Lu, Z. Li, B. Cheng, and M. Leppäranta. A parameterization of the ice-ocean drag coefficient. *Journal of Geophysical Research: Oceans*, 116(C7), 2011.

[22] C. Lüpkes, V. M. Gryanik, J. Hartmann, and E. L. Andreas. A parametrization, based on sea ice morphology, of the neutral atmospheric drag coefficients for weather prediction and climate models. *Journal of Geophysical Research: Atmospheres*, 117(D13), 2012.

[23] G. A. Maykut. Large-scale heat exchange and ice production in the central Arctic. *Journal of Geophysical Research: Oceans*, 87(C10):7971–7984, 1982.

[24] F. Mesinger, G. DiMego, E. Kalnay, K. Mitchell, P. C. Shafran, W. Ebisuzaki, D. Jović, J. Woollen, E. Rogers, E. H. Berbery, et al. North American regional reanalysis. *Bulletin of the American Meteorological Society*, 87(3):343–360, 2006.

[25] D. Pringle, H. Eicken, H. Trodahl, and L. Backstrom. Thermal conductivity of landfast Antarctic and Arctic sea ice. *Journal of Geophysical Research: Oceans*, 112(C4), 2007.

[26] R. W. Reynolds, T. M. Smith, C. Liu, D. B. Chelton, K. S. Casey, and M. G. Schlax. Daily high-resolution-blended analyses for sea surface temperature. *Journal of Climate*, 20(22):5473–5496, 2007.

[27] R. Ricker, S. Hendricks, L. Kaleschke, and X. Tian-Kunze. CS2SMOS: Weekly Arctic Sea-Ice Thickness Data Record, 2016.

[28] T. M. Smith. A long-term record of blended satellite and in situ sea-surface temperature for climate monitoring, modeling and environmental studies. *Earth System Science Data*, 8(1):165, 2016.

[29] G. Spreen, L. Kaleschke, and G. Heygster. Sea ice remote sensing using AMSR-E 89-GHz channels. *Journal of Geophysical Research: Oceans*, 113(C2), 2008.

[30] A. Thorndike, D. Rothrock, G. Maykut, and R. Colony. The thickness distribution of sea ice. *Journal of Geophysical Research*, 80(33):4501–4513, 1975.

[31] X. Tian-Kunze, L. Kaleschke, N. Maaß, M. Mäkynen, N. Serra, M. Drusch, and T. Krumpen. SMOS-derived thin sea ice thickness: algorithm baseline, product specifications and initial verification. *Cryosphere*, 8(3):997–1018, 2014.

[32] S. Tietsche, M. Alonso-Balmaseda, P. Rosnay, H. Zuo, X. Tian-Kunze, and L. Kaleschke. Thin sea ice in the arctic: comparing l-band radiometry retrievals with an ocean reanalysis.

[33] S. Tietsche, M. Balmaseda, H. Zuo, and P. de Rosnay. *Comparing Arctic Winter Sea-ice Thickness from SMOS and ORAS5*. European Centre for Medium-Range Weather Forecasts, 2017.

[34] R. Tonboe, J. Lavelle, R.-H. Pfeiffer, and E. Howe. Product User Manual for OSI SAF Global Sea Ice Concentration. 2016.

[35] M. Tsamados, D. L. Feltham, D. Schroeder, D. Flocco, S. L. Farrell, N. Kurtz, S. W. Laxon, and S. Bacon. Impact of variable atmospheric and oceanic form drag on simulations of Arctic sea ice. *Journal of Physical Oceanography*, 44(5):1329–1353, 2014.

Chapter 4

Estimation of Sea Ice Characteristics in the Region of Baffin Bay and Labrador Sea Using High-Resolution Model with the Assimilation of Ice Concentration and SST

4.1 Overview

In the previous chapter (Chapter 3) the model implementation and validation on a regional scale were discussed. Long-term simulations could deviate from true values

due to inherent uncertainties in the model. These uncertainties may arise due to the lack of accurate parameterizations and assumptions in the model. Data assimilation techniques bring model values closer to observation by minimizing the error between model and observation. In order to make forecasts of the future state of a system, initial conditions need to be closer to the observed state. In numerical models, this is achieved via data assimilation. In this chapter, we explore data assimilation methodologies to retrieve sea ice parameters and also improve the accuracy of the model.

4.2 Introduction

Sea ice estimation and forecasting are important for ship navigation and regional climate and ocean ecosystem studies. Sea ice is a heterogeneous media, which makes it practically difficult for microwave satellite imagery [3] to estimate ice thickness, freeboard, and ridge parameters. Climate forecast researchers depend on numerical modeling techniques that implement the physical processes of the atmosphere and the ocean on large-scale computational platforms along with assimilation methods to retrieve information on sea ice parameters. Data assimilation methods also give us better initial conditions for forecasting. Due to the high inter-annual variability of sea ice in the region of Baffin Bay and the Labrador Sea [8], estimating sea ice parameters is a significant challenge in this region.

Previous sea ice modeling and assimilation studies at the Canadian Ice Service (CIS) [16] provided an overview of an operational ice model coupled with atmospheric and ocean modules. The research [18] compared the evolution of ice thickness distributions and later by the development of an operational ice dynamics model for

CIS [17]. These modeling works were also improved by data assimilation methods [5, 4]. The CIOM included the Princeton Ocean Model for the simulation of ocean parameters and a multi-category ice model. The total ice fraction retrieved from the Special Sensor Microwave/Imager (SSM/I) was assimilated into the CIOM model using a 3D-VAR technique [5] to estimate the ice concentration. The assimilation was further improved by using both daily ice charts and RADARSAT image analysis using a 3D-VAR technique for sea ice concentration forecasts. The 3D-VAR assimilation technique can also be used to combine multiple sources of observational data with a sophisticated forecast model to analyze and forecast sea ice conditions.

An Assimilation study by Lindsay et al. [12] showed significant improvements in assimilated ice concentration but with a large bias in the ice thickness pattern. Cheng et al. [6] presented a method for ice concentration and thickness analysis that combined sea ice thermodynamics modeling and ice motion detection by space-borne SAR data. The method showed promising results for sea ice concentration and ice thickness estimates compared to CIS ice charts. In another study, OSI SAF data were assimilated into the Regional Ocean Modeling System for simulating sea ice concentration, and this produced better results than the simulation without assimilated OSI SAF data. Ice concentration and extent were overestimated, possibly due to the bias in atmospheric forcing and underestimation of heat flux and over/under estimation of sea ice growth/melt processes [24].

Most sea ice models are coupled with ocean models. The advantage of the CICE model is its standalone capability. Here, we use a combination of modeling using the standalone sea ice model, CICE [9] and the assimilation method suggested by Lindsay et al. [12] and Wang et al. [24] for SST and ice concentration. The simulated

sea ice parameters were then validated with the observations in the region of Baffin Bay and the Labrador Sea. This work uses a high-resolution model configuration, which was previously described in Chapter 3. Further, the effect and reliability of the assimilation of ice concentration on the estimation of ice thickness and freeboard measures were compared.

4.3 Model domain and forcing data

The sea ice model was implemented on a regional scale of about 10 km with a slab ocean mixed layer parameterization. Density-based criteria were used [14] to compute the mixed-layer depth and thereby compute the SST and the potential to grow or melt sea ice. The analysis of the non-assimilated model for the sea ice concentration and its seasonal means showed that the error associated with the model mostly spread across the area of the North Water polynya and the Davis Strait where the interaction of cold and warm water is frequent. In the present study, a data assimilation module is also introduced.

The surface atmospheric forcing is from high-resolution NARR data. The ocean forcing is from various sources: currents from CFSR, salinity from WOA-2013 and MLD computed from WOA-2013 [14]. Atmospheric and ocean forcing were used as inputs to the model. For SST, the climatology data derived from high-resolution NOAA reanalysis products were used as an input for the initial conditions and open boundaries. For the ice concentration and thickness, the initial condition is assumed as a no-ice state at the beginning of September. The assimilation starts from January 2005 and whenever remote sensing data are missing the model is not assimilated, see

Table 4.1 for temporal gaps.

4.4 Remote sensing data for assimilation and validation

The daily data used for the ice concentration assimilation in the model were derived from AMSR-E and AMSR2. See Table 4.1 for the time period of the availability of data. The assimilated model results were then compared with the OSI SAF data. Only reliable (standard deviation (SD) of $20\% - 30\%$), good (SD of $10\% - 20\%$) and excellent (SD of $0\% - 10\%$) data from OSI SAF were used for comparison. The details of the sensors were given in Section 3.6 and Table 3.2. For SST assimilation of the measurements derived from AVHRR were used, see Section 3.6.

The model ice thickness has been compared with the estimates derived from SMOS-MIRAS. The estimated uncertainties of SMOS ice thickness retrieval were about 20% for ice thicknesses less than 30 cm and up to 100% for ice thicknesses more than 50 cm, showing a large underestimation/overestimation of thick ice; see Section 3.6 and Table 3.3 for details on the SMOS-MIRAS instrument. The uncertainty of SMOS ice thickness (observation) includes the error contributions caused by the brightness temperature, ice salinity, and ice temperature. Insufficient knowledge of snow cover also introduces a large uncertainty in the thickness estimates from SMOS. In addition, large errors occur during the melting period. In general, the uncertainty of thickness observation increases with increasing ice thickness, snow cover,

Table 4.1: Time period when AMSR-E/AMSR2 data were available

From	To
24-MAR-2005	31-MAR-2005
17-NOV-2005	30-NOV-2005
13-MAY-2006	31-MAY-2006
17-NOV-2006	30-NOV-2006
02-MAR-2007	31-MAR-2007
27-NOV-2007	02-DEC-2007
13-AUG-2008	31-AUG-2008
02-FEB-2010	28-FEB-2010
04-OCT-2011	31-JUL-2012
11-MAY-2013	31-MAY-2013

and onset of melt [10].

The model freeboard had been compared with the measures derived from CryoSat-2. The CryoSat-2 altimeter operating in the SAR mode has an accuracy of about 1 cm with a spatial sampling of about 45 cm [2]. The pulse limit footprint width in the across-track direction is about 1.65 km and beam limited footprint width in the along-track direction is about 305 m [19], which corresponds to an along-track resolution of about 401 m (assuming a flat-Earth approximation). Therefore, the pulse-Doppler-limited footprint for the SAR mode is about 0.6 km^2. CryoSat-2 freeboard and ice concentration products were generated at the Alfred Wegener Institute (AWI) [15]. The products were available in a spherical Lambert azimuthal equal-area projection with 25 km resolution. The uncertainty in freeboard measurements can arise from speckle noise, a lack of leads which cause the estimation of sea surface height to be unreliable, and snow cover. The uncertainty of up to 40 cm can be observed in the region of Baffin Bay and the Labrador Sea [15]. Freeboard data were not available from May to September due to the high error in the retrieved parameter.

4.5 Data Assimilation

The assimilation module uses the combined optimal interpolation and nudging technique for ice concentration [12, 24]. The method can be represented generally [7, 12] as

$$X_a = X_b + dt\frac{K}{\tau}(X_o - X_b), \tag{4.1}$$

where X_a is the final analysis of the variable, X_o is the observed quantity (for ice concentration this is AMSR-E/AMSR2, for SST this is AVHRR), X_b is the background estimate of the variable (for ice concentration and SST this is model estimate), dt is the model time step, τ is the basic nudging time scale as in [24], and K is the nudging weight with the optimal interpolation value. K is computed as

$$K = \frac{\sigma_b^\alpha}{\sigma_b^\alpha + \sigma_o^2}, \tag{4.2}$$

where σ_b and σ_o are the error standard deviation of the model estimate [7] and the observations [7], respectively. The parameters in the weighing factor given in equation (4.2) is defined according to [12] as $\sigma_b = |X_o - X_b|$, $\sigma_o = 0.08$ (parameter may vary spatially), and $\alpha = 6$.

When assimilation of ice concentration, $\sigma_o = 0.08$ was calculated from a long-term standard deviation to 0.08 since the AMSR-E/AMSR2 ice concentration error was unknown for values less than 65% [20]. The parameter $\alpha = 6$, was used for the present study to ensure that the coefficients for assimilation were heavily weighted only when there was large variation between the model and the observation [12], see Appendix B.1 for the significance of the parameter α.

SST is also assimilated using the nudging and optimal interpolation scheme. For SST assimilation, σ_o was fixed as 0.05°C to compensate for the assumption of zero mixed layer heat flux. A value α equals to 6 [12] was also used for the assimilation of SST to ensure that only large differences between the model and observation were weighted heavily, see Appendix B.1 for the significance of the parameter α.

The assimilation of ice concentration was then followed by a re-computation of the estimated sea ice volume. The ice volume was subtracted or added by including the

increment with specified ice thickness or decreased at current thickness. The model flow chart with the assimilation module is shown in Figure 4.1. For updates on the tracers such as level ice and melt ponds see Appendix B.2

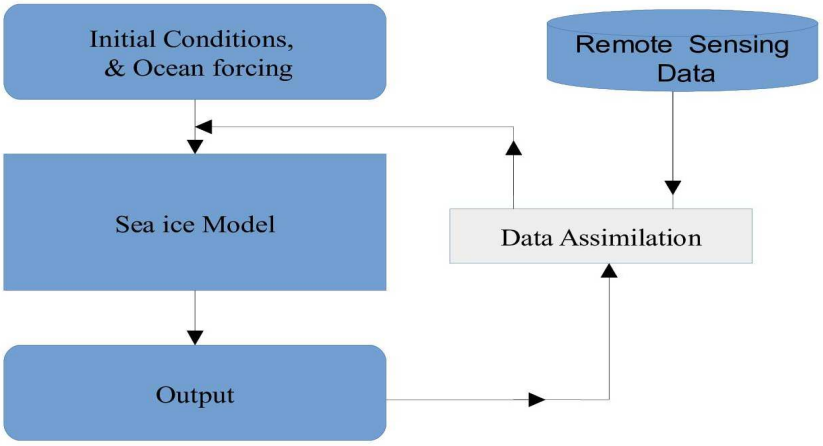

Figure 4.1: The model flow chart.

4.6 Results and validation

Three model results are discussed here: model 'M0', the non-assimilated model; 'M1', the model assimilated with ice concentration from AMSR-E/AMSR2; and 'M2', the model assimilated with ice concentration from AMSR-E/AMSR2 and SST from AVHRR. 'M2'assimilates only SST whenever there is a data gap in ice concentration from AMSR-E e.g. from 24 March 2005 to 31 March 2005 AMSR-E data were not available and, in that case, M2 assimilates only SST.

4.6.1 Ice concentration

Figure 4.2 column 1 shows the absolute error between the non-assimilated model and the OSI SAF (M0), column 2 shows the absolute error of the model assimilated only with ice concentration and OSI SAF (M1), and column 3 shows the absolute error of the model assimilated with both ice concentration and SST and OSI SAF (M2). Model M2 shows improvement in the ice concentration for January and March, but the results do not improve much during May.

Figure 4.3 shows the absolute error of the model and OSI SAF: row 1 showing the absolute error from January 2010 to September 2011 and row 2 showing the absolute error from August 2012 to December 2015. The assimilation of SST and ice concentration decreases the error between the model and the OSI SAF ice concentration. In 2010, the non-assimilated model error of 4.624% was reduced to 1.939% by assimilating ice concentration. The assimilation of SST and ice concentration decreased the error to about 1.118% in 2010.

From October 2011 to July 2012, AMSR-E data were not available for a more extended period, and model M2 was assimilated only with SST, see Figure 4.4. During this period, the SST assimilation decreased the error between the model and the observation by almost 3%. The assimilation of ice concentration along with the assimilation of SST decreased the error in the ice concentration and reduced the summer errors the most.

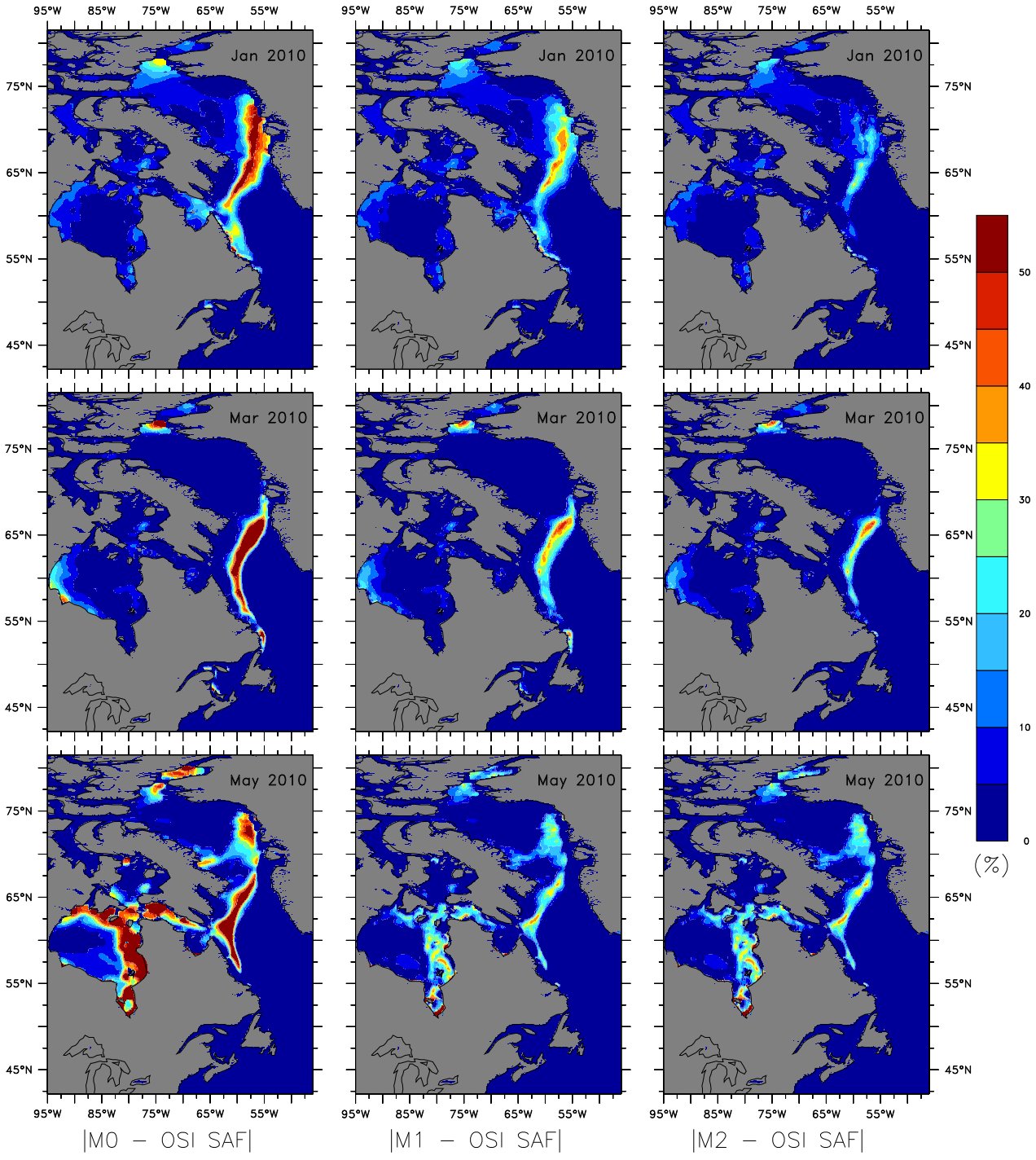

Figure 4.2: The absolute error between the model and OSI SAF column1: M0 and OSI SAF, column 2: M1 and OSI SAF and column3: M2 and OSI SAF.

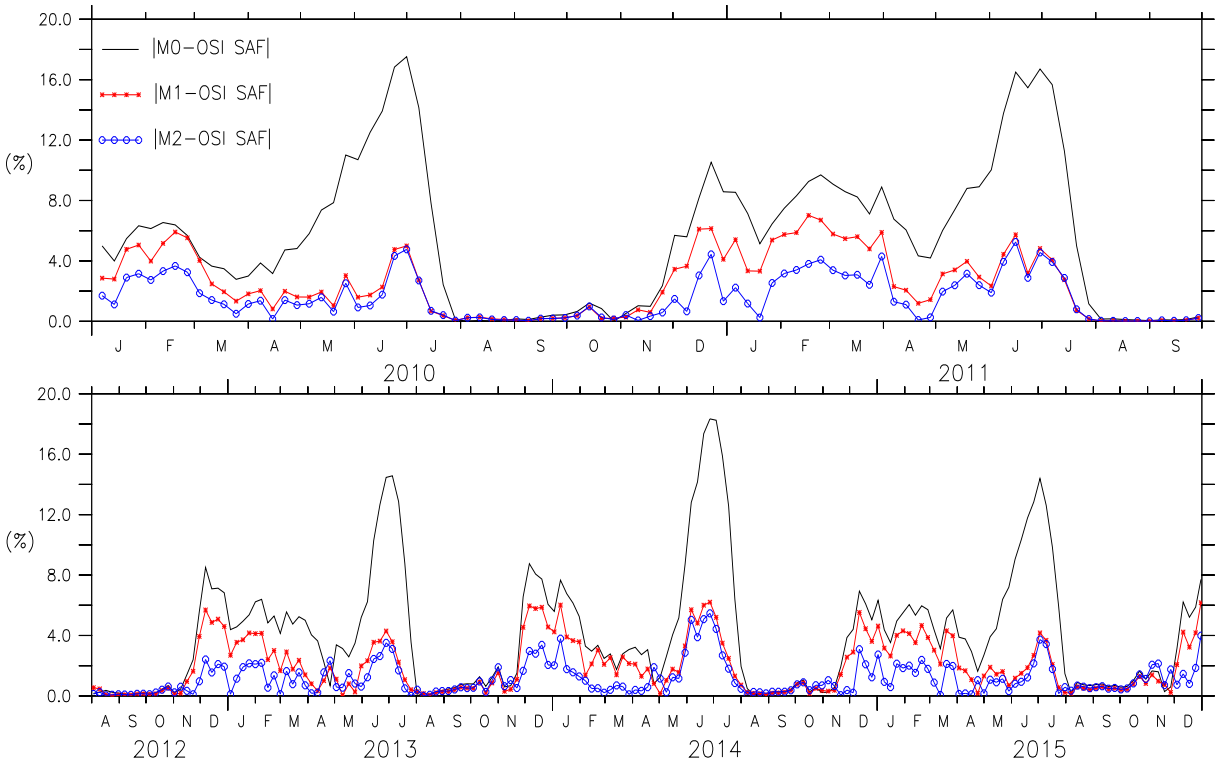

Figure 4.3: The absolute errors between model and OSI SAF from January 2010 to September 2011 is shown in row 1 and absolute error between model and OSI SAF from August 2012 to December 2015 is shown in row 2.

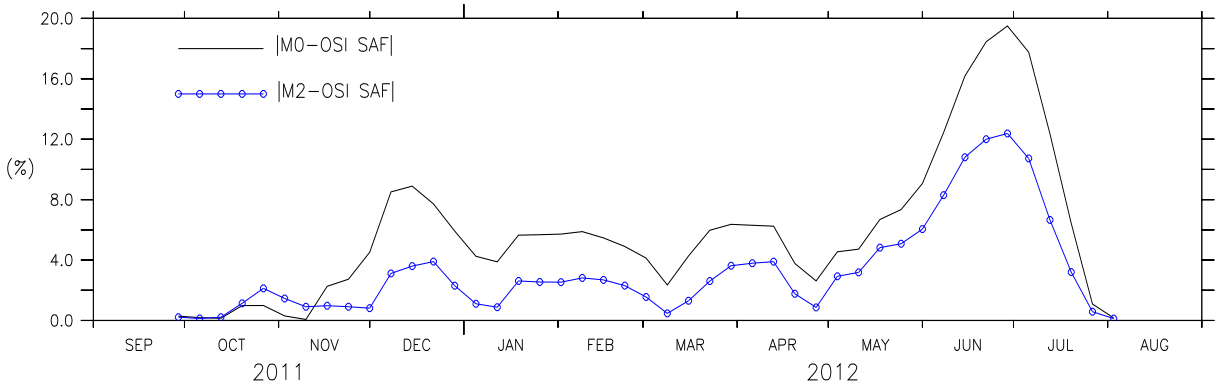

Figure 4.4: The absolute errors between model and OSI SAF from October 2011 to July 2012, SST only is assimilated during the time period.

4.6.2 Ice thickness

Due to the high uncertainity levels of SMOS thickness data during the melt season the data from April until October were not available for the region of interest [11, 1]. The large unacceptable uncertainties in SMOS derived ice thickness creates difficulties for the analysis. For comparison and validation, ice thickness data from both the model and SMOS, where the SMOS ice thickness was greater than zero and the uncertainty values of SMOS were below 30 cm were used. The thickness errors were lower for thin ice (below 20 cm) and increased as the thickness increased [22].

Figure 4.5 shows the absolute error between the model M0, M1, M2 and SMOS ice thickness. The model error was within the chosen uncertainty limits of the SMOS until late February, after which the model error exceeds the chosen uncertainty limits. A significant deviation was observed at the end of January 2014. The SMOS data were influenced by the presence of snow and the onset of the melt season, which made the data unreliable from March/April. The results for the period 2011-2012 when there was only the assimilation of SST are shown in Figure 4.6.

The Model M2 thickness, SMOS derived ice thickness, and the uncertainty of the SMOS-derived measurement for 15 December, 15 January, and 15 March for the years 2010-2011 are shown in Figure 4.7. See Appendix B.3 for more figures that show ice thickness for 15 December, 15 January, and 15 March for years 2011-2015.

Data derived using remote sensing measurements may sometimes result in unacceptable values. Data that exceed a certain uncertainty threshold are not used for practical applications. It was strictly recommended not to use data retrieved from SMOS with an uncertainty greater than 1 m [21]. For comparison and validation,

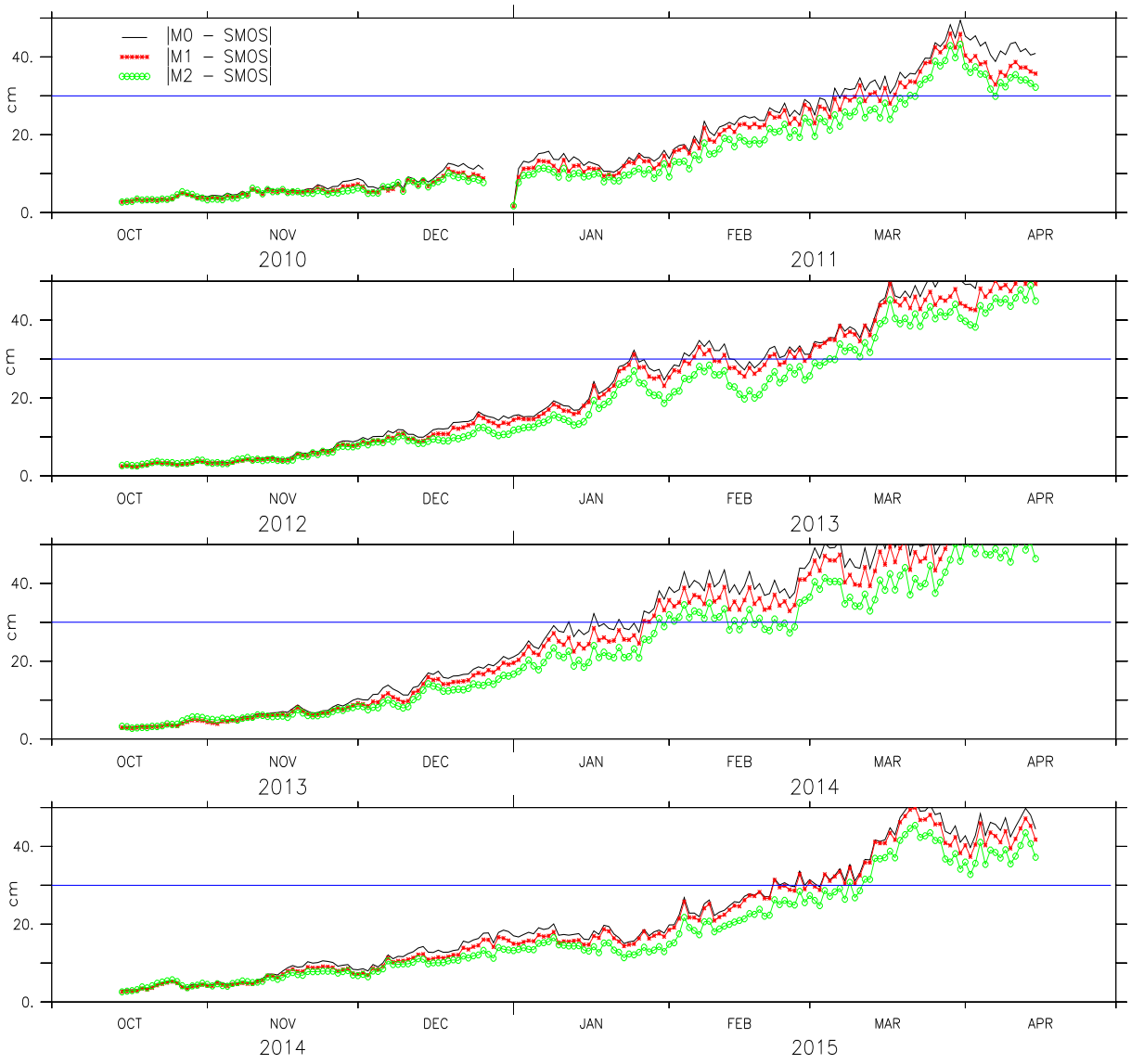

Figure 4.5: The absolute errors between the model and SMOS ice thickness. The blue straight line denotes the chosen uncertainty level for ice thickness from observation.

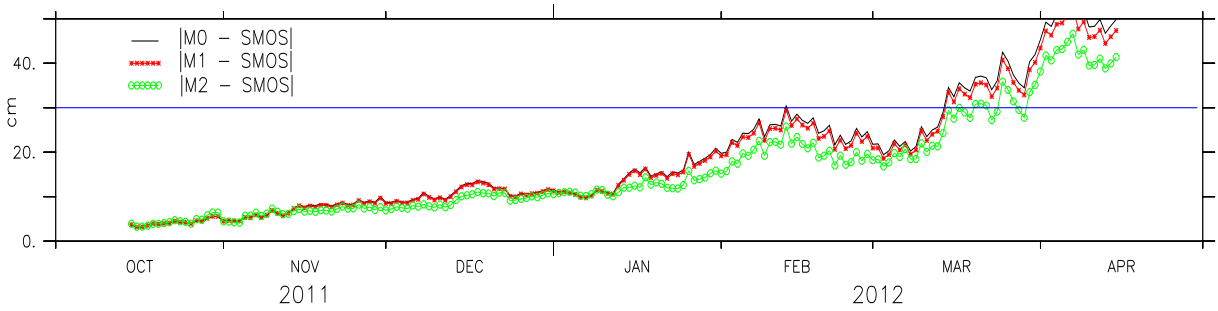

Figure 4.6: The absolute errors between the models M0, M1, M2 and SMOS ice thickness. The blue straight line denotes the chosen uncertainty level for ice thickness from SMOS.

ice thickness data from both the model and SMOS were selected when the observed ice thickness is greater than zero and uncertainty was less than or equal to 100 cm. The SMOS thickness has less uncertainty for thinner ice and higher uncertainty for thicker ice, see Table 3.4 for the uncertainty of SMOS ice thickness. Figures 4.8, 4.9, and 4.10 shows the mean values of the thickness estimated from models M0, M1, M2 and SMOS with the uncertainty limits of the SMOS ice thickness (shaded gray). The values of Model M2 are within the uncertainty limits of SMOS ice thickness until the end of February (except for 2014) end. In the case of SMOS derived thickness, the uncertainties would increase with the snow accumulation and melt onset. From the comparison, during March, the model results exceed the uncertainty limits. Compared with the uncertainty values, these results are in the acceptable range from October to the end of February. Figure 4.10 shows the results for the period October 2011 to April 2012 when AMSR-E data were absent during which M1 was not assimilated with ice concentration but used the initial conditions from the assimilated result. Model M2 used the initial conditions assimilated with both ice concentration

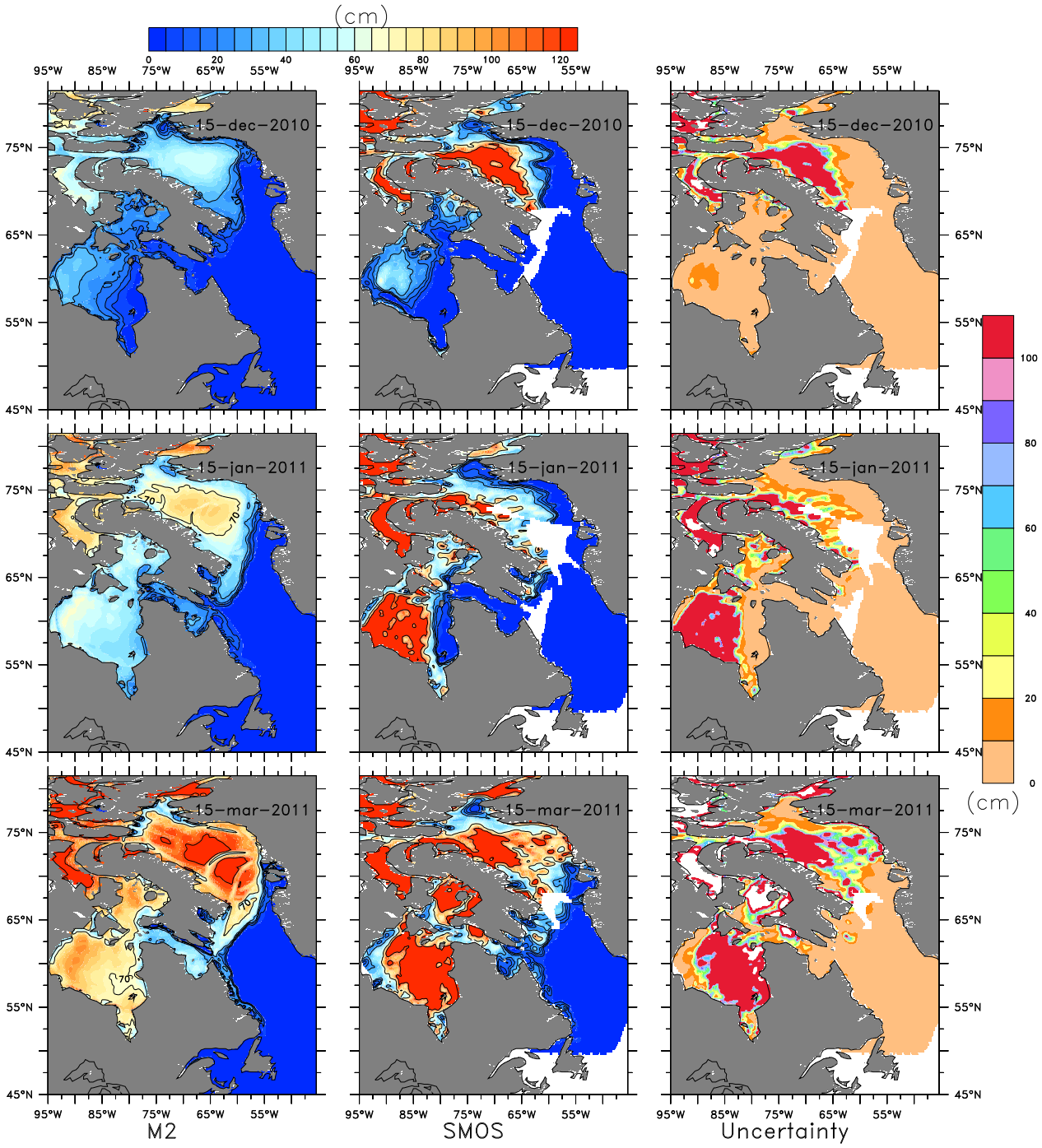

Figure 4.7: The model M2 estimated ice thickness, ice thickness estimated from SMOS, and the SMOS uncertainty for 2010-2011.

and SST, but assimilates only SST during the period. Both models, M1 and M2, with the improved initial conditions show better forecasts in the long-term analysis. One of the reasons why the model values exceed the uncertainty limits during March is the choice of $\alpha = 6$, which considers only large differences while weighing the coefficient K. Also, the assumptions of zero mixed layer heat flux, constant salinity and mixed layer profile contributes to the error. Since the assimilation shows improvement in ice thickness, using a value of $\alpha = 2$, it is expected to impose the model values within the uncertainty limits.

Figure 4.11, shows the observed SST from AVHRR with the shaded regions representing the observation uncertainty, SST from models M0, M1 and M2. The SST assimilation improves the ice concentration and ice thickness results for the model M2. The assimilated model M2 still has outliers observed during the winter period. The model results can be improved by decreasing α ($\alpha = 6$ selected for simulations presented here) and by reducing the nudging time scale (SST nudging scale was set to 30 days for simulations discussed here). Decreasing the nudging time scale can result in the late formation and early melt of ice (not shown here). The results can be improved by choosing the nudging time scale to be less frequent during ice growth and more frequent during the winter till beginning or mid of March. Frequent nudging of SST causes instability in the thermodynamic model. The parameters in the assimilation should be selected so that a balance is maintained for the timing of ice formation and melt onset and to maintain the stability of the model thermodynamics and dynamics. For M0, the non-assimilated model results may be improved by including the mixed layer heat flux with a parametrization similar to [13]. Also, note that the model still assumes a fixed ocean salinity and MLD.

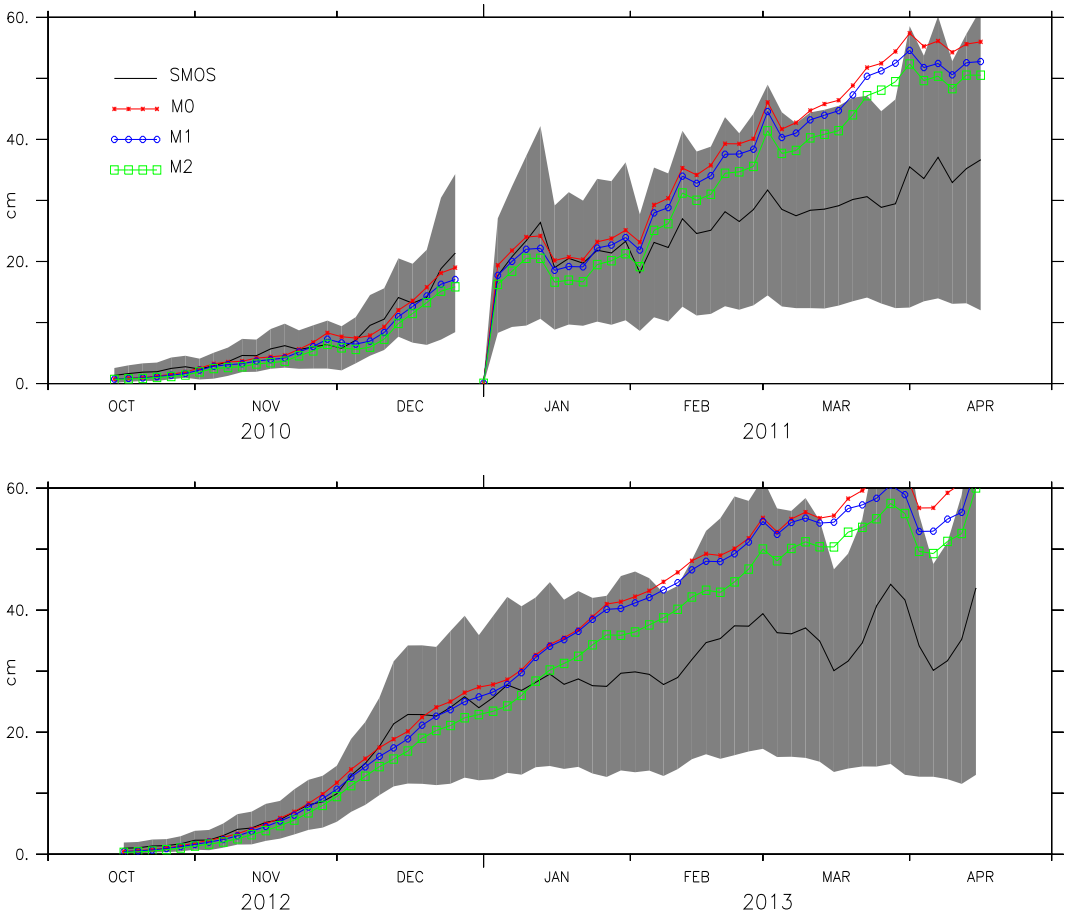

Figure 4.8: The ice thickness from the models M0, M1, M2, and SMOS from October 2010 to April 2011 and October 2012 to April 2013. The uncertainty of SMOS ice thickness is shaded in gray.

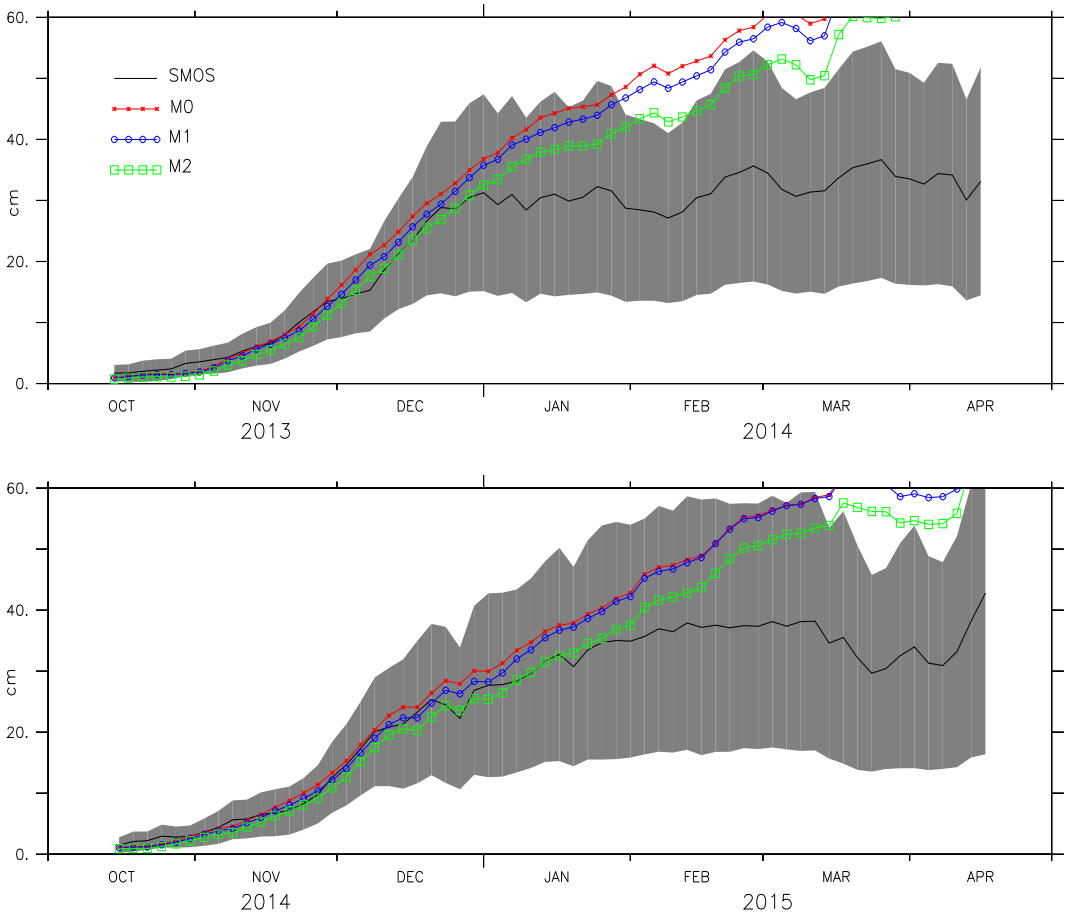

Figure 4.9: The ice thickness from the models M0, M1, M2, and SMOS from October 2013 to April 2014 and October 2014 to April 2015. The uncertainty of SMOS ice thickness is shaded in gray.

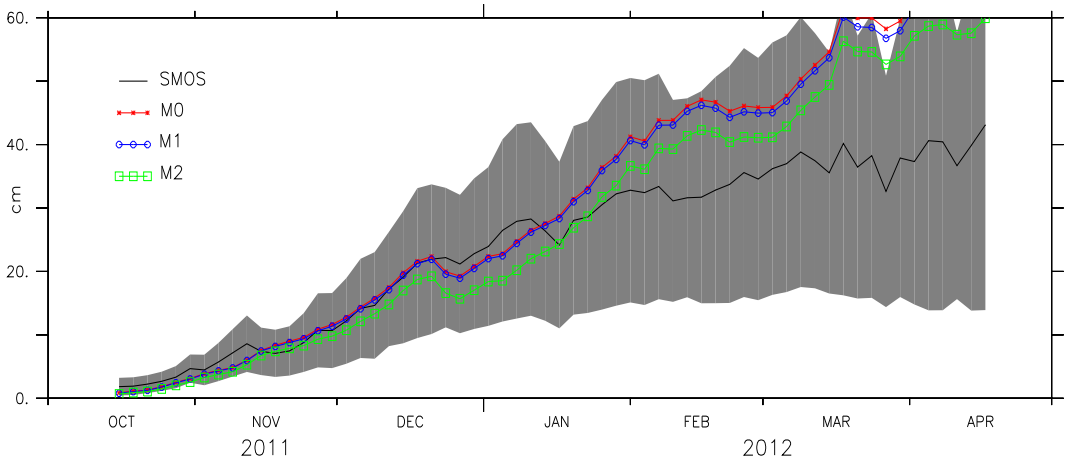

Figure 4.10: The ice thickness from models M0, M1(non-assimilated but used the initial conditions from the model assimilated with ice concentration), M2 (assimilated only with SST and used model initial conditions derived from assimilating both ice concentration and SST) and SMOS from October 2011 to April 2012. The uncertainty of SMOS ice thickness is shaded in gray.

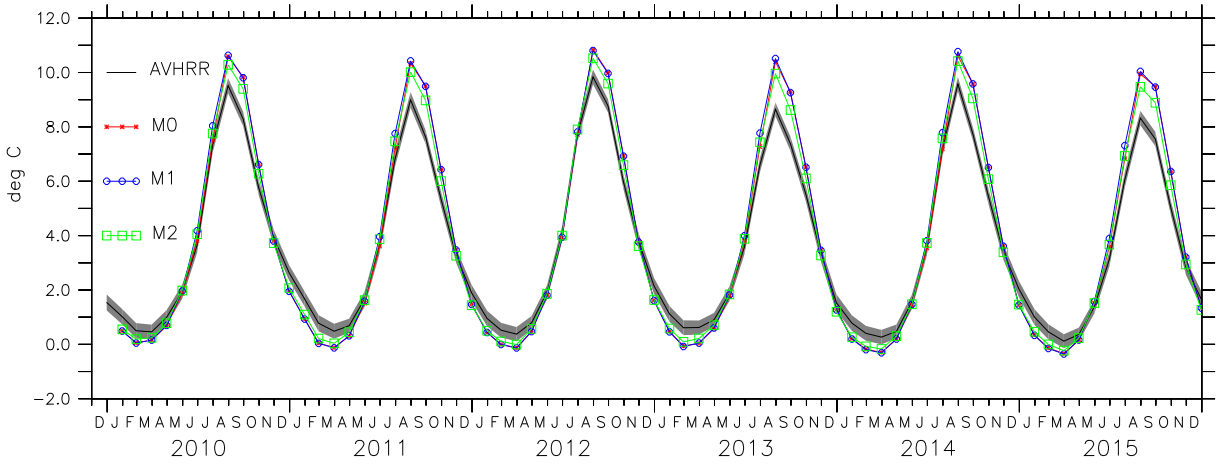

Figure 4.11: The SST from AVHRR with the shaded region represents the uncertainty of AVHRR SST, and SST from models M0, M1, M2.

4.6.3 Freeboard

The observation uncertainty of freeboard measurements can arise due to lack of leads. The presence of leads had been ensured by selecting regions where the lead fraction derived from CryoSat-2 was greater than zero. In the model, freeboard was computed using equation (4.3) [23]. For the region, the uncertainty of the measurements is below 40 cm [15].

$$D_f = (v_{ice} + v_{sno})/A - D, \tag{4.3}$$

where v_{ice} is the volume of ice, v_{sno} is the volume of snow, A is the ice concentration, D is the Draft, computed as in

$$D = (\rho_i v_{ice} + \rho_s v_{sno})/(A\rho_w), \tag{4.4}$$

where $\rho_i = 917kg/m^3$ is the density of ice, $\rho_s = 330.0kg/m^3$ is the density of snow and $\rho_w = 1026kg/m^3$.

The absolute difference between the model and the CryoSat-2 for January, February and March 2011 is shown in the Figure 4.12. M2 freeboard measures are close to the observed freeboard. See Appendix B.4 for more figures that show the difference between the model and CryoSat-2 for years 2012-2015.

Figure 4.13 shows the RMSE of freeboard from model M2 and CryoSat-2 in the areas where the lead fraction was greater than zero. The RMSE is below the maximum uncertainty of 40 cm for the region of interest.

Figure 4.14 shows the freeboard estimates from Model M2, CryoSat-2 and the uncertainty of the freeboard estimates from CryoSat. Appendix B.5 for more figures

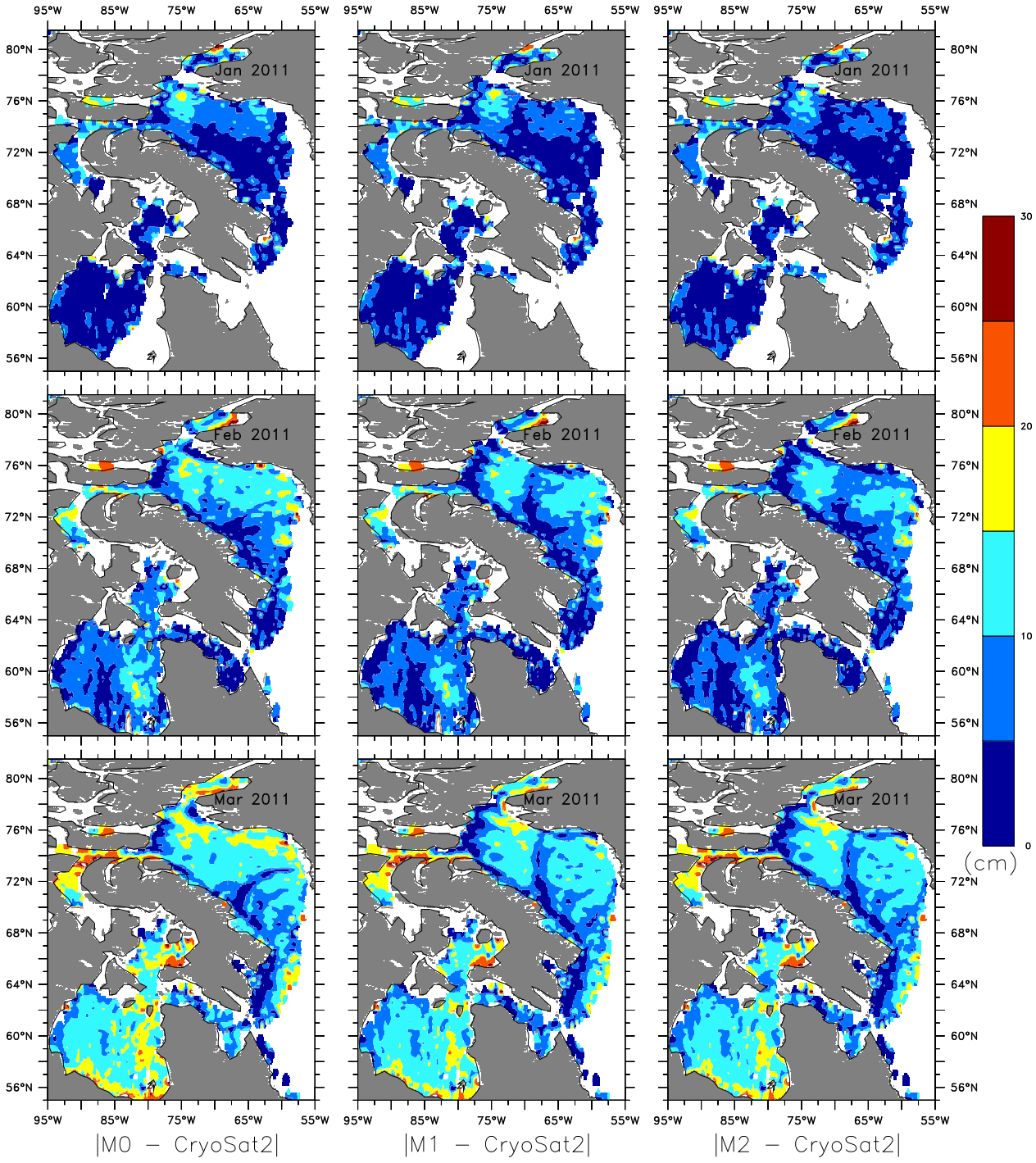

Figure 4.12: Absolute error between the model freeboard and CryoSat-2 for 2011.

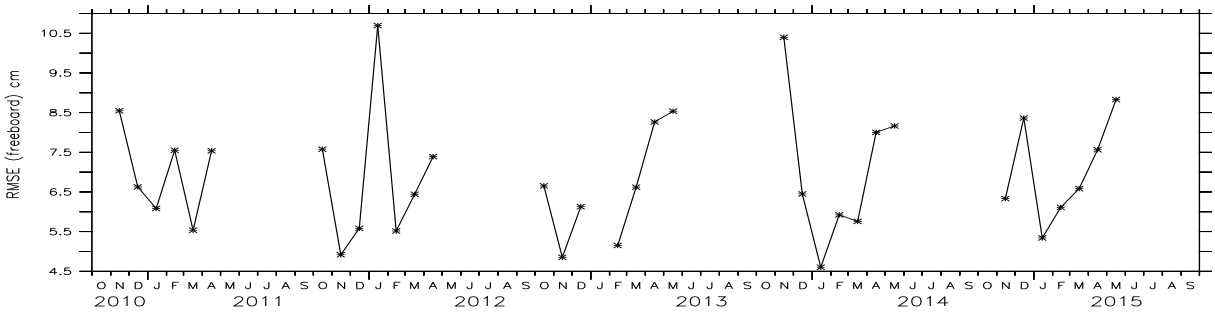

Figure 4.13: The RMSE of freeboard measure for the regions where the lead fraction is above 0%.

that show the M2 freeboard estimate, CryoSat-2 estimate and uncertainty of CryoSat-2 estimate for years 2012-2015.

Figure 4.15 shows spatial average of the freeboard estimates from the model M2, CryoSat-2 and the spatial averaged uncertainty of CryoSat-2 measurements. Only the model results from M2 were shown since there are only slight deviations for M0 and M1 from the CryoSat-2 estimates. Moreover, we were interested in the results of the assimilated model and how well it performs in the estimation of freeboard. The model values are within the uncertainty limits of the CryoSat-2 estimates. Also, note that the model results were monthly averaged, while CryoSat-2 was a mosaic.

4.7 Conclusions

The assimilated models that exists in the literature, and those that were implemented in forecasting centres uses a constant drag formulation and lacks the details on deriving the parameters other than ice concentration, and ice thickness [24, 12, 4]. In this work a variable drag formulation was used for the friction associated with an

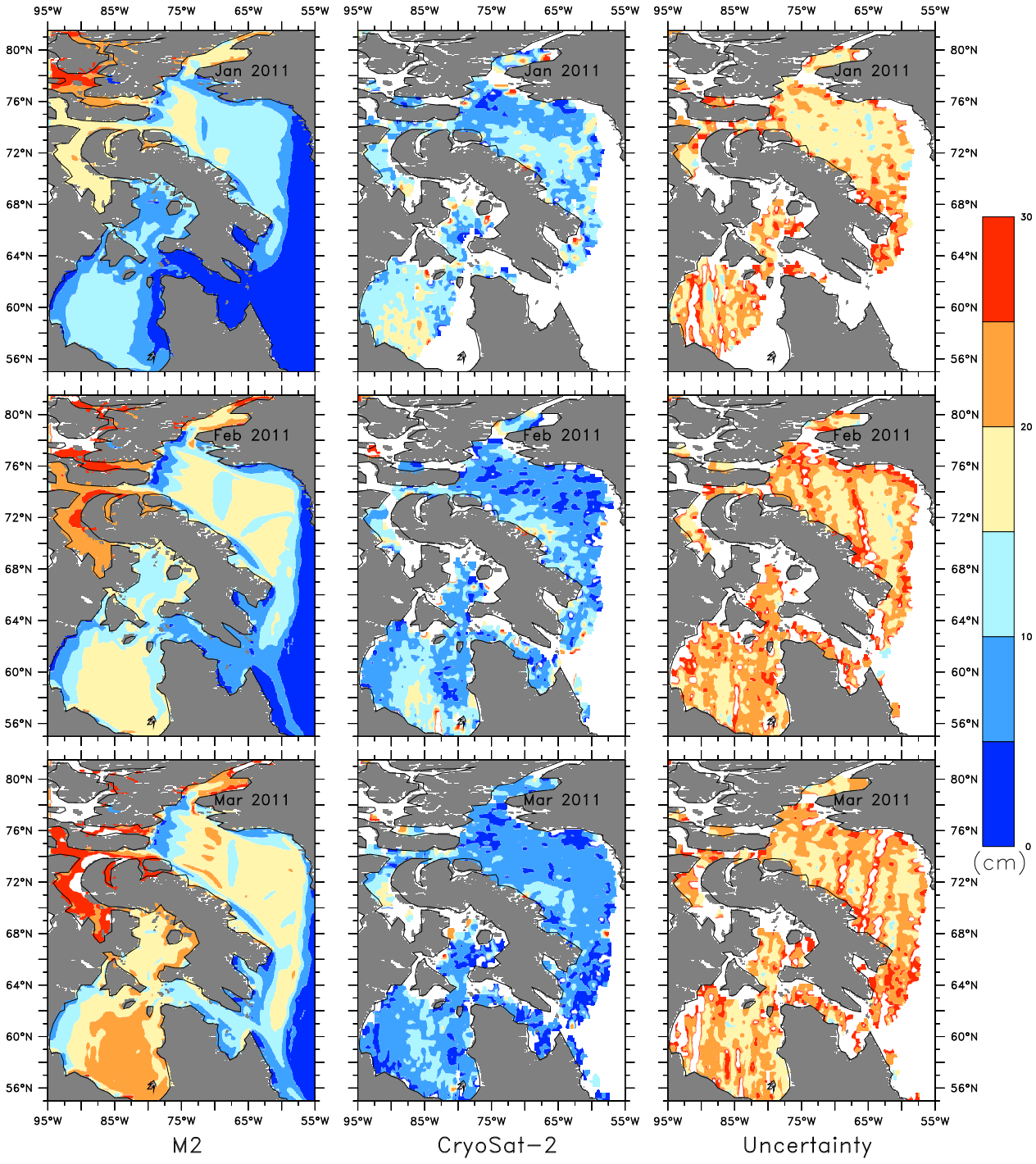

Figure 4.14: Freeboard from model M2, CryoSat-2 and the uncertainty of CryoSat-2 freeboard estimates for 2011.

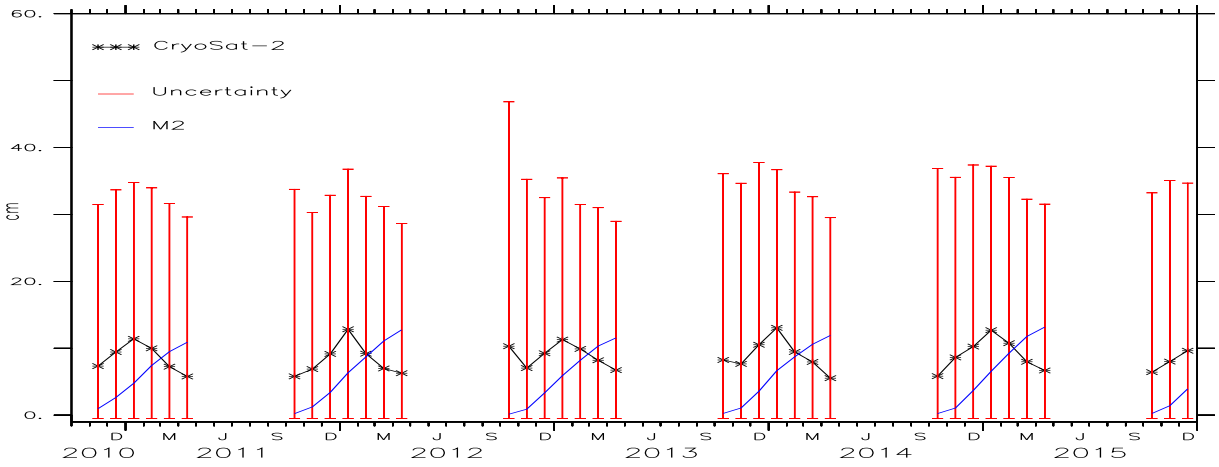

Figure 4.15: Freeboard from model M2, CryoSat-2 and the uncertainty of the CryoSat-2 freeboard estimates for 2011.

effective sea ice surface roughness at the ice-atmosphere and ice-ocean interfaces and to compute the ice to ocean heat transfer. The inclusion of the variable drag formulation required assimilation updates on variables such as ice thickness, level ice tracer and melt-ponds, which were discussed. The results of the updated model estimates were then compared with satellite derived measurements to validate the assimilation strategy. Moreover, the assimilated model results includes ice thickness, freeboard, and sail height, keel depth (discussed in Chapter 5) in addition to ice concentration.

The non-assimilated model presented in Chapter 3 was extended by assimilating with ice concentration observations from AMSR-E data, which showed improvements in ice concentration, thickness, and freeboard estimates. The model-estimated parameters improved further by assimilating SST from AVHRR.

The modeled ice thickness demonstrated a good correspondence with the estimates from SMOS-MIRAS, except during the period of maximum ice extent. The model estimates of freeboard were compared with estimates from CryoSat-2, and the

RMSE was found to range between 4.5 cm and 11 cm. The estimates of freeboard from the model were within the uncertainty values of the CryoSat-2 (below 40 cm). The deviation in the results of ice thickness during March have to be further explored by tuning the parameters that contribute to the ice thickness in the non assimilated model as well as the assimilation parameters. Also, the SMOS estimates were influenced by the presence of snow and also during the melt seasons the uncertainties of SMOS estimated ice thickness might increase in which case comparison with more reliable data would be required.

The assimilation methodology can be further improved by tuning the parameters, refining the error estimates derived from the observation data and combining data from several sources.

Bibliography

[1] H. M. Barré, B. Duesmann, and Y. H. Kerr. SMOS: The mission and the system. *IEEE Transactions on Geoscience and Remote Sensing*, 46(3):587–593, 2008.

[2] C. Bouzinac. CryoSat product handbook. *ESA User Manual, ESA, ESRIN, Italy*, 4121:4123, 2014.

[3] F. D. Carsey. *Microwave remote sensing of sea ice*. American Geophysical Union, 1992.

[4] A. Caya, M. Buehner, and T. Carrieres. Analysis and forecasting of sea ice conditions with three-dimensional variational data assimilation and a coupled ice–ocean model. *Journal of Atmospheric and Oceanic Technology*, 27(2):353–369, 2010.

[5] A. Caya, M. Buehner, M. Shokr, and T. Carrieres. A first attempt of data assimilation for operational sea ice monitoring in Canada. In *Geoscience and Remote Sensing Symposium, 2006. IGARSS 2006. IEEE International Conference on*, pages 1705–1708. IEEE, 2006.

[6] B. Cheng, T. Vihma, M. Arkett, T. Carrieres, et al. A method for sea ice thickness and concentration analysis based on SAR data and a thermodynamic model. *Cryosphere*, 6(6):1507, 2012.

[7] R. Deutch. Estimation theory. 1965.

[8] I. Fenty and P. Heimbach. Coupled sea ice–ocean-state estimation in the Labrador Sea and Baffin Bay. *Journal of Physical Oceanography*, 43(5):884–904, 2013.

[9] E. C. Hunke, W. H. Lipscomb, A. K. Turner, N. Jeffery, and S. Elliott. CICE: the Los Alamos Sea Ice Model Documentation and Software Users Manual Version 5.1 LA-CC-06-012. *T-3 Fluid Dynamics Group, Los Alamos National Laboratory*, 675, 2015.

[10] L. Kaleschke, X. Tian-Kunze, N. Maaß, G. Heygster, M. Huntemann, H. Wang, and C. Haas. SMOS Sea Ice Retrieval Study (SMOSIce), ESA Support To Science Element (STSE), Final Report ESA ESTEC contract no. Technical report, 4000101476/10/NL/CT, 2013.

[11] Y. H. Kerr, P. Waldteufel, J.-P. Wigneron, J. Martinuzzi, J. Font, and M. Berger. Soil moisture retrieval from space: The Soil Moisture and Ocean Salinity (SMOS) mission. *IEEE transactions on Geoscience and remote sensing*, 39(8):1729–1735, 2001.

[12] Lindsay, RW and Zhang, J. Assimilation of ice concentration in an ice–ocean model. *Journal of Atmospheric and Oceanic Technology*, 23(5):742–749, 2006.

[13] A. A. Petty, P. R. Holland, and D. L. Feltham. Sea ice and the ocean mixed layer over the Antarctic shelf seas. *Cryosphere*, 8(2):761–783, 2014.

[14] S. Prasad, I. Zakharov, P. Bobby, and P. McGuire. The implementation of sea ice model on a regional high-resolution scale. *Ocean Dynamics*, 65(9-10):1353–1366, 2015.

[15] R. Ricker, S. Hendricks, V. Helm, H. Skourup, and M. Davidson. Sensitivity of CryoSat-2 Arctic sea-ice freeboard and thickness on radar-waveform interpretation. *Cryosphere*, 8(4):1607–1622, 2014.

[16] M. Sayed, T. Carrieres, et al. Overview of a new operational ice model. In *The Ninth International Offshore and Polar Engineering Conference*. International Society of Offshore and Polar Engineers, 1999.

[17] M. Sayed, T. Carrieres, H. Tran, S. B. Savage, et al. Development of an operational ice dynamics model for the Canadian Ice Service. In *The Twelfth International Offshore and Polar Engineering Conference*. International Society of Offshore and Polar Engineers, 2002.

[18] M. Sayed, S. Savage, and T. Carrieres. Examination of Ice Ridging Methods Using Discrete Particles. In *Proceedings 16th International Conference on Port and Ocean Engineering under Arctic Conditions (POAC'01)*, pages 1087–1096, 2001.

[19] M. Scagliola. CryoSat footprints Aresys technical note. *SAR-CRY2-TEN-6331, Aresys/ESA, Italy*, 2013.

[20] G. Spreen, L. Kaleschke, and G. Heygster. Sea ice remote sensing using AMSR-E 89-GHz channels. *Journal of Geophysical Research: Oceans*, 113(C2), 2008.

[21] X. Tian-Kunze and L. Kaleschke. *Read-me-first note for the release of the SMOS Level 3 ice thickness data product*. University of Hamburg, 2016.

[22] X. Tian-Kunze, L. Kaleschke, N. Maaß, M. Mäkynen, N. Serra, M. Drusch, and T. Krumpen. SMOS-derived thin sea ice thickness: algorithm baseline, product specifications and initial verification. *Cryosphere*, 8(3):997–1018, 2014.

[23] M. Tsamados, D. L. Feltham, D. Schroeder, D. Flocco, S. L. Farrell, N. Kurtz, S. W. Laxon, and S. Bacon. Impact of variable atmospheric and oceanic form drag on simulations of Arctic sea ice. *Journal of Physical Oceanography*, 44(5):1329–1353, 2014.

[24] K. Wang, J. Debernard, A. K. Sperrevik, P. E. Isachsen, and T. Lavergne. A combined optimal interpolation and nudging scheme to assimilate OSISAF sea-ice concentration into ROMS. *Annals of Glaciology*, 54(62):8–12, 2013.

Chapter 5

Model Comparison with In-situ Measurements

5.1 Overview

The model in Chapter 4 can be used to determine relations between ice parameters. Here, the draft retrieved from ULS and the model results were used to determine the coefficients that relate the keel depth and sail height. The CIS ice chart and image/videos collected during a field campaign were used to determine the ice concentration, which was further used to compare with the model results.

5.2 Introduction

Along with the measurements derived from satellite data, the information on sea ice concentration, thickness and draft can also be derived from from sources such as submarines, ships or instruments like ULS located at various stations. The only

drawback is that the measurements of ice concentration, thickness and draft from the above-mentioned sources provide only localized values. Information such as field estimates may be useful to tune the model parameters. The draft derived from ULS was used to extract the level ice draft and keel depth, the estimates are then compared with the model to determine the relationship between sail and keel. The ice concentration retrieved from airborne reconnaissance data and CIS ice charts were compared with the model estimated values.

5.3 Airborne and in situ data

The ice draft measurements from the ULS instrument which was located on the Makkovik Bank (Figure 5.1) at 58 W and 54 N) [7] were used to analyze the keel depth and the level ice draft in the region. The ULS data collected data at an interval of approximately 5.5 seconds and were available from the beginning of January to end of May during 2005, 2007 and 2009 [7].

The images and the videos obtained during Labrador Iceberg survey fieldwork by Provincial Aerospace Ltd. were used to estimate the ice concentration. The objective of the survey was to evaluate the capabilities of multi-frequency and multi-polarization SAR for the detection of icebergs in sea ice [1]. The surveys were conducted on 2 March 2009, 5 March 2009, and 17 March 2009, and the area of the survey included the Labrador shelf, north of Groswater Bay. Along with the SAR acquisitions from RADARSAT-2 and TerraSAR-X an areal survey was also conducted. The videos and images that were obtained from this areal survey had been used for the present study to determine the ice concentration and further compare it with the model estimates.

The photographs/videos were recorded using a Nikon D100 camera with a 28 to 200-mm lens, and were valuable in showing the sea ice conditions in the vicinity. The planned altitude for the survey was 600 m, which gives a maximum field of view of 300 m for the video. But to void turbulence and to fly below the clouds the altitude were often adjusted and hence some of the recorded data suffered from flicker and dropouts.

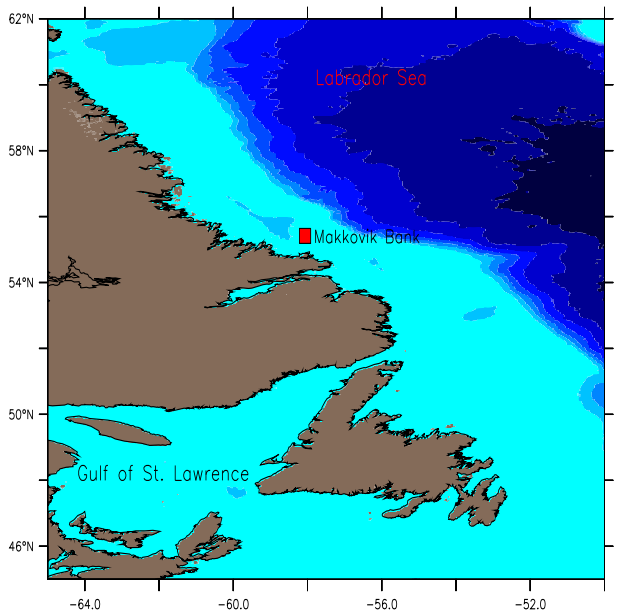

Figure 5.1: The location of ULS instrument.

The ice charts incorporate information from several sources such as NOAA AVHRR, Geostationary Operational Environmental Satellite system (GOES), SSMI, QuikSCAT, ENVISAT and particularly RADARSAT-2 [8]. Also, the field observation charts from ships, helicopter and aircraft provide ground truths. The ice charts are very detailed and have a higher spatial resolution than many other sources of ice information [8]. The ice concentration from the Canadian Ice Service ice chart was used for compari-

son with the model estimated values of ice concentration. The representation of basic data such as ice concentrations, stages of development (age) and form (floe size) of ice are known as egg codes [8, 2]. The egg codes are easy to understand and maximum of three ice types are described in the code. Figure 5.2 shows a sample CIS chart with egg codes. The colour code for ice concentration range is also shown at the bottom of the figure. Please refer to Canadian Ice Service publications on Interpreting ice charts for more details on interpretation of egg codes [8, 2].

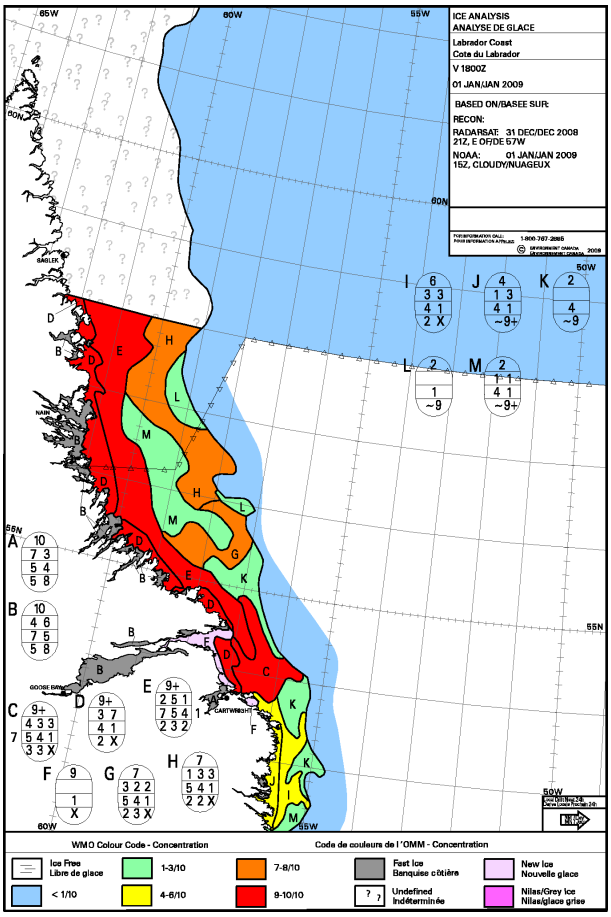

Figure 5.2: CIS ice chart.

5.3.1 ULS data analysis

The erroneous data during the calibration of the instrument were not used for the analysis. Data from ULS was then used to separate out the level ice draft and the keel measurements. For this filtering, the histograms for each day were used, e.g., see Figure 5.3 for the histogram from the ULS data for 01 March 2009. The first mode in the histogram corresponded to the level ice draft and the second mode of the histogram corresponded to the keel measurement. The first mode of the histogram was selected by finding a minimum between two peaks of the histogram. The separated values from the histogram (first mode and second mode) were then averaged daily for the comparison with the model. Figure 5.4 shows the hourly values of level ice draft derived from ULS for 01 Mar 2009 along with the average for the day. Figure 5.5 shows the hourly keel values derived from the ULS for 01 Mar 2009 [6] along with the average value for the day.

5.3.2 Video/Image analysis

The videos were converted to images and then used for computing ice concentration. There were thousands of images derived from the videos and only clear images and images with fewer shadows that were cast by icebergs, and pressure ridges were used for the analysis. The video footage shows the location and date when the data were derived. A sample image from the video is shown in Figure, 5.6.

Global Otsu's method was used to segment the image [4]. The Otsu's method maximizes the between-class variance. The well-thresholded classes would be distinct with respect to the intensity values of their pixels, and conversely, a threshold giving

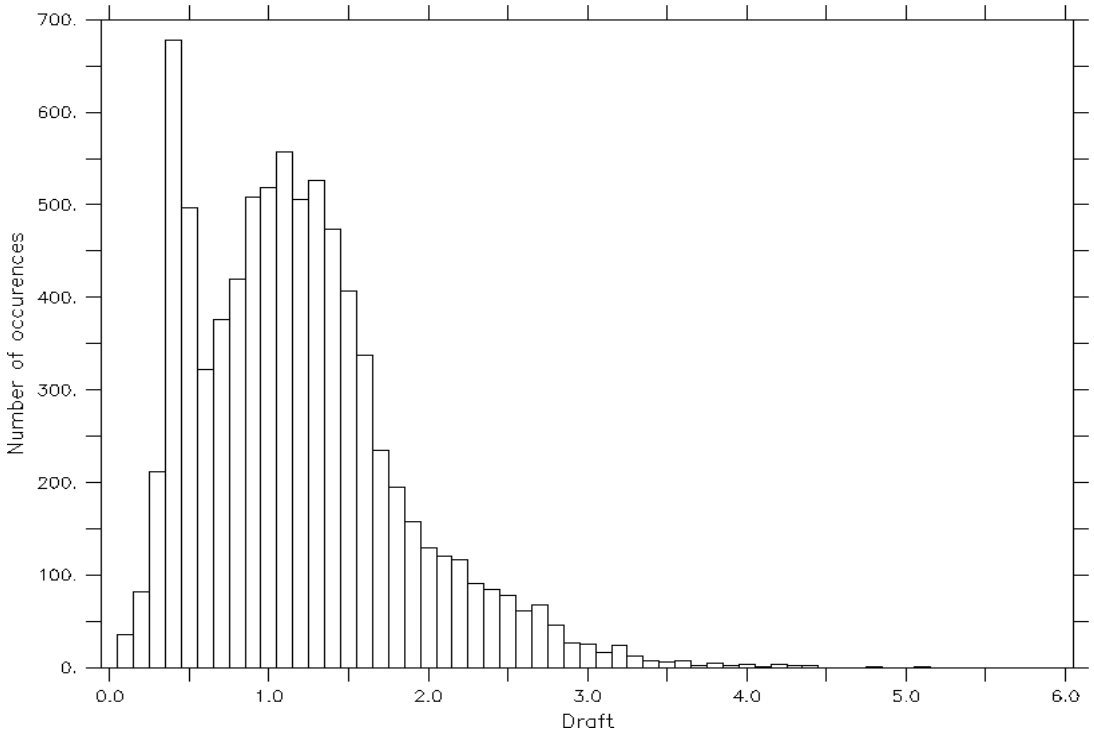

Figure 5.3: Histogram from ULS data for 01 March 2009.

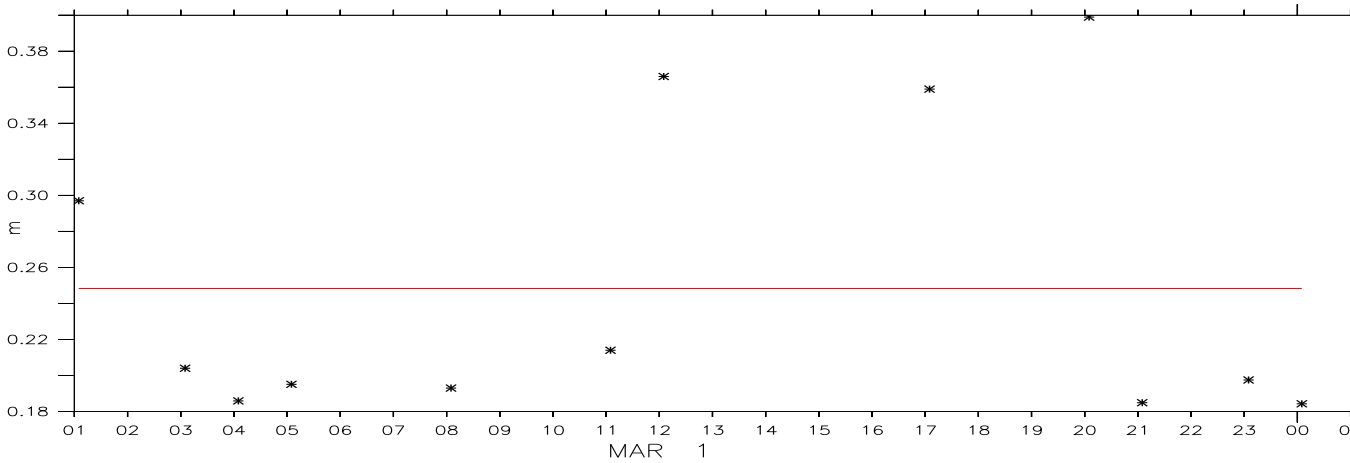

Figure 5.4: Level ice draft extracted from the histogram for 01 March 2009. The red line is the average value of the draft.

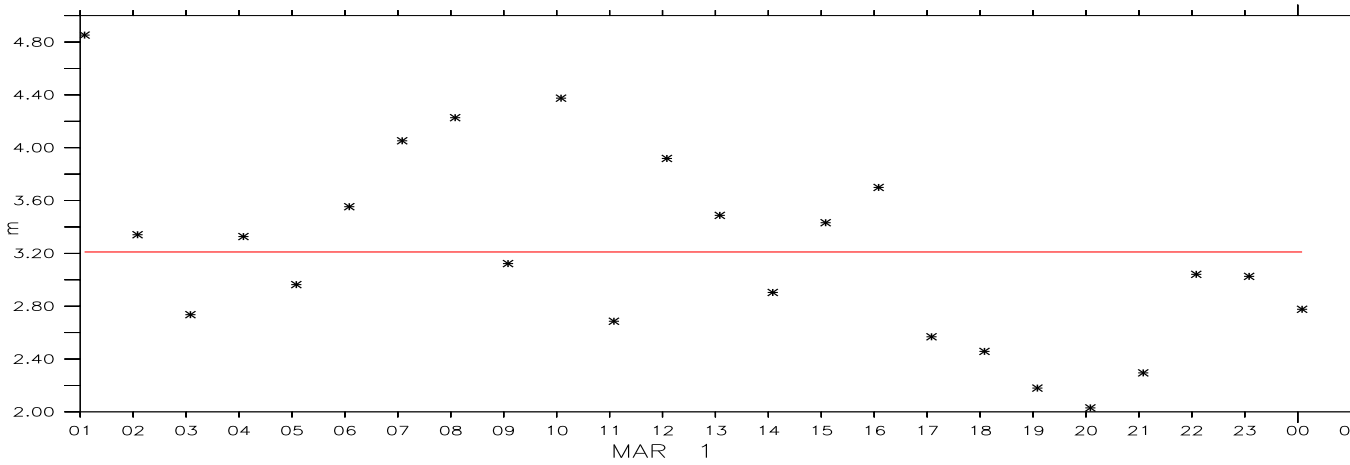

Figure 5.5: Keel extracted from the histogram for 01 March 2009. The red line is the average value of the keel.

the best separation between classes in terms of their intensity values would be the optimum threshold. Suppose the image is to be divided into two classes, C_1 and C_2, where C_1 consists of all the pixels in the image with intensity values in the range $[0, k]$ and C_2 consists of all the pixels in the image with intensity values in the range $[k+1, L-1]$ where there are L distinct intensity levels in the image. The optimum threshold is the value k^* is given by

$$\sigma_B^2(k^*) = \max_{0 \leq k \leq L-1} \sigma_B^2(k) \tag{5.1}$$

where $\sigma_B^2(k)$ is given by

$$\sigma_B^2(k) = \frac{(m_G P_1(k) - m(k))^2}{P_1(k)(1 - P_1(k))} \tag{5.2}$$

where P_1 is the probability of class C1, m is the average intensity up to level k, m_G is the average intensity of the entire image. Once k^* is obtained, the input image

$f(x, y)$ the input image is segmented as

$$g(x, y) = \begin{cases} 1 & f(x, y) > k^*, \\ 0 & f(x, y) \leq k^*, \end{cases} \tag{5.3}$$

and then the ice concentration is determined for the whole image as the ratio of the number of white pixels with the total number of image pixels. See Figure 5.7 for the thresholded image with an ice concentration of 0.7043. Several images are analyzed and then averaged to derive the ice concentration. Since some images had icebergs or shadows that resulted in reduced ice concentration, only images that had few shadows were used.

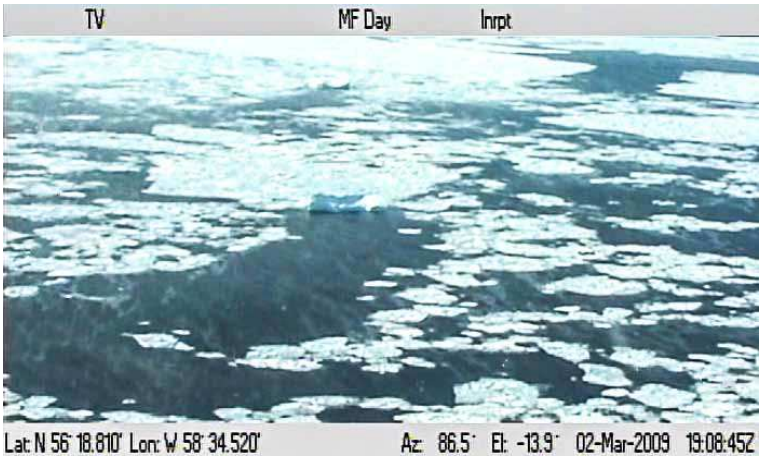

Figure 5.6: The sample image from the video.

5.4 Results and validation

The ULS measurements were separated into level ice draft and keel measurements as described in Section 5.3. The model values of level ice draft was computed using

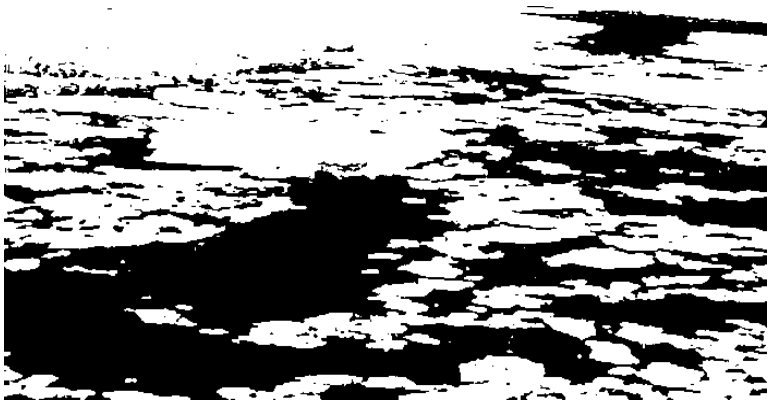

Figure 5.7: Thresholded image of the sample using Otsu's method.

equation (4.4) [12]. The results are shown in Figure 5.8.

Though substantial deviations were observed at some temporal points, the temporal averaged absolute error between model and ULS values were within 10 cm. The discrepancy may be caused due to the fact that ULS provides measurements at a particular location with a high resolution (within the footprint of several meters), while the model is of a 10-km resolution and gives an averaged result close to the location of the ULS.

The keel was computed using idealized sea ice floe comprising a system of two ridges and a single melt pond [12]. The geometry of sails and keels were considered to have triangular cross sections, which represent younger ridges [12]. The older sails and keels have a Gaussian shape [12] which was neglected here, i.e., all the sails and keels were considered to be younger ridged ice. The sail height is given by the equation (5.4) and the relation between the sail height and keel depth is given by

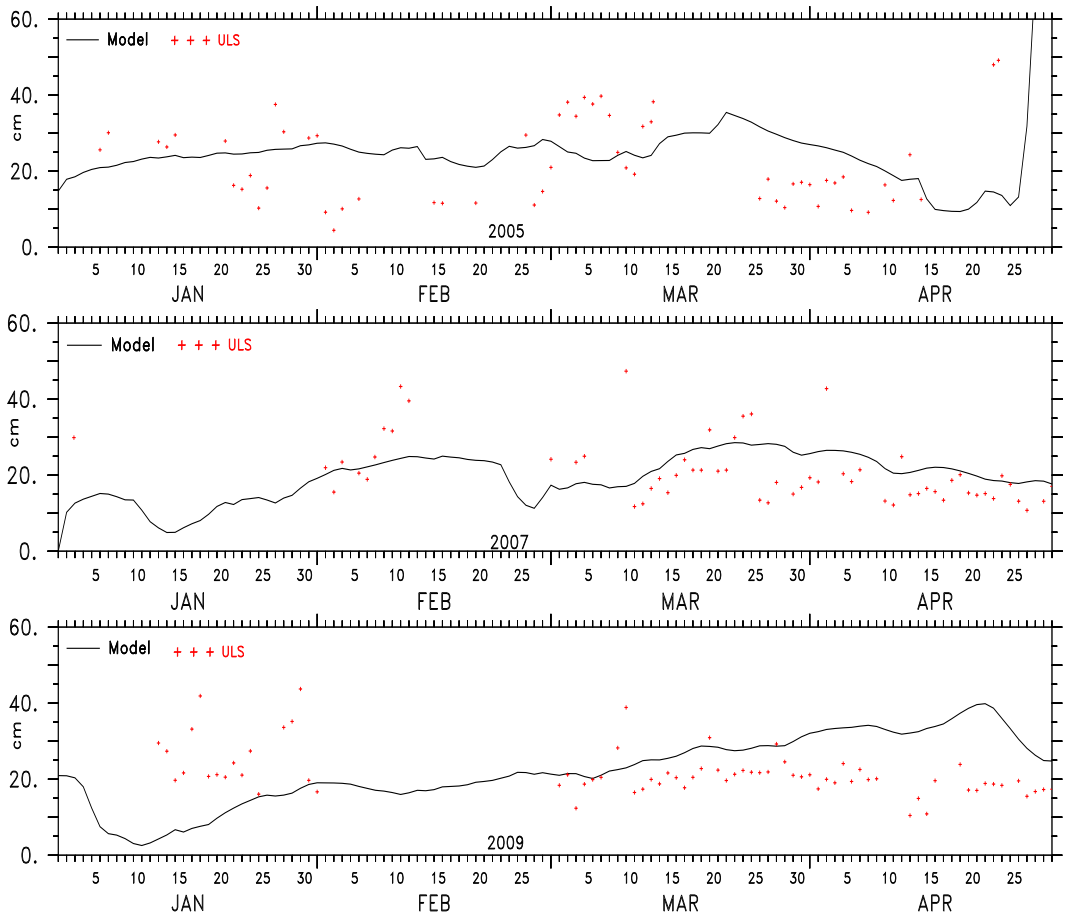

Figure 5.8: Level ice draft computed from the ULS measurement and the model estimated values in cm for 2005, 2007 and 2009.

equation (5.5).

$$H_s = 2\frac{V_r}{A_r}\frac{(\alpha D_k m_k + \beta C m_s)}{(\phi_s m_k D_k + \phi_k m_s C^2)} \tag{5.4}$$

where H_s is the sail height, $m_s = 0.4$ (21.8°) and $m_k = 0.5$ (26.5°) are the slopes of the sail and the keel, respectively, ϕ_s is the porosity of the sails, and $\phi_k = 0.7240$ is the porosity of the keels. $D_k = 5$ is the ratio distance between the keels to the distance between the sails. V_r is the volume of the ridged ice, A_r is the ridged ice area fraction, α and β are the weight functions for the area of ridged ice, C is the coefficient that relates sail to keel and

$$H_k = CH_s \tag{5.5}$$

gives the keel depth. The Makkovik Bank where the keel measurements were estimated from ULS has high variability of ice thickness, and the frequency of the formation of keels is high due to the combined effect of the Labrador currents and winds, and because rafted ice is common in this region. Here, the model and the observation were used to estimate C.

A typical value for C estimated from field observation is 4.5 by [5] and 4.0 by [12]). A study conducted in the Laptev-Sea by [3] showed that C varies between 3.4 and 9. Another parametric study illustrated in [9] shows a different set of parametrizations for the relationship between sail and keel of first year and multi-year ice. The studies [9, 11] were presented from profiles of 184 ridges reported in 22 different studies. An exponential relationship, $H_k = a{H_s}^b$, was used to fit the data points, the values of a and b depends on the ice type. Please refer to [9, 11] for more information

about the parameters a and b. The model equation (5.5) and the observation were used to estimate C. Data collected in 2005, 2007 and 2009 show that a value of C between 3.00 and 4.50 gives a good estimate of keel measurement for January and February, while a value between 7.00 and 8.00 gives a good estimate for keel during March, April, and May. In Figure 5.9 the values C that relate the sail to keel for January and February are 3 and $C = 7.00$ for March, April and May. These values are derived under the assumptions in equation (5.4). The sensitivity of parameters in equation (5.4) has to be further explored to determine the effect on the sail-keel relationship, which may result in a different conclusion. Moreover, since a variable drag coefficient has been used in the model, the parameters that control the drag contribution from the ridges, floes and skin affect the bottom heat flux, which in turn affects the thickness distribution.

The CIS ice charts show the presence of new(< 10cm), grey($10 - 15$cm), grey-white($15 - 30$ cm), thin first year ($30 - 70$ cm), medium first year ($70 - 120$ cm) ice in the region during January-February while the region is mostly composed of thin, medium and thick first-year ice (> 120 cm) during March, April, and May. See Figure 5.10 for the ice types from CIS ice chart for 09 January 2009 and 09 April 2009, respectively. The change in the ice type may be the reason for the large values of the keel depth estimated from the ULS. Increasing ice thickness is expected to strongly affect the ridging process by impeding the progress of thin ice. A parameter estimation along with the activation of ice age tracers would be required to tune the model and to understand further about the formation of ridges and the sensitivity/optimization of parameters that control ridge and keel formation. Only results from M2 are presented to show the relationship from the assimilated model.

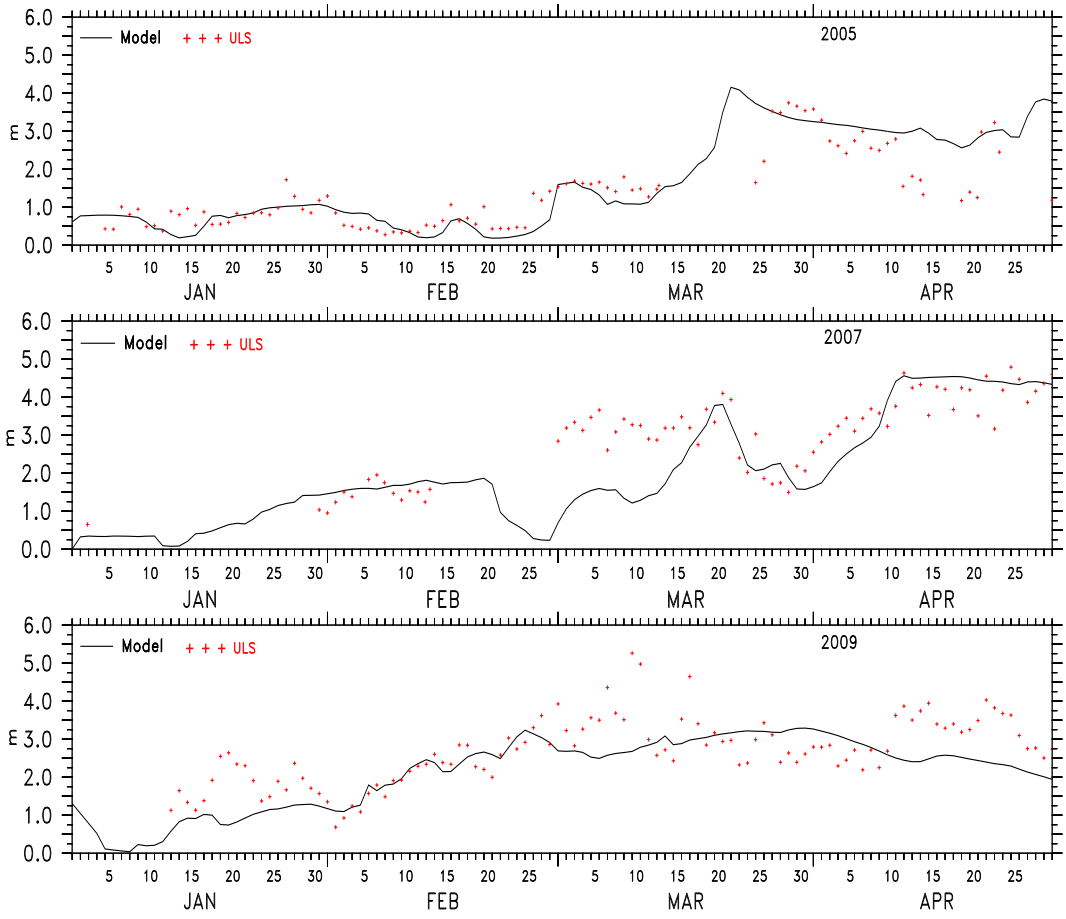

Figure 5.9: The keel depth estimated from the ULS measurement and the model estimated values in m for 2005, 2007 and 2009.

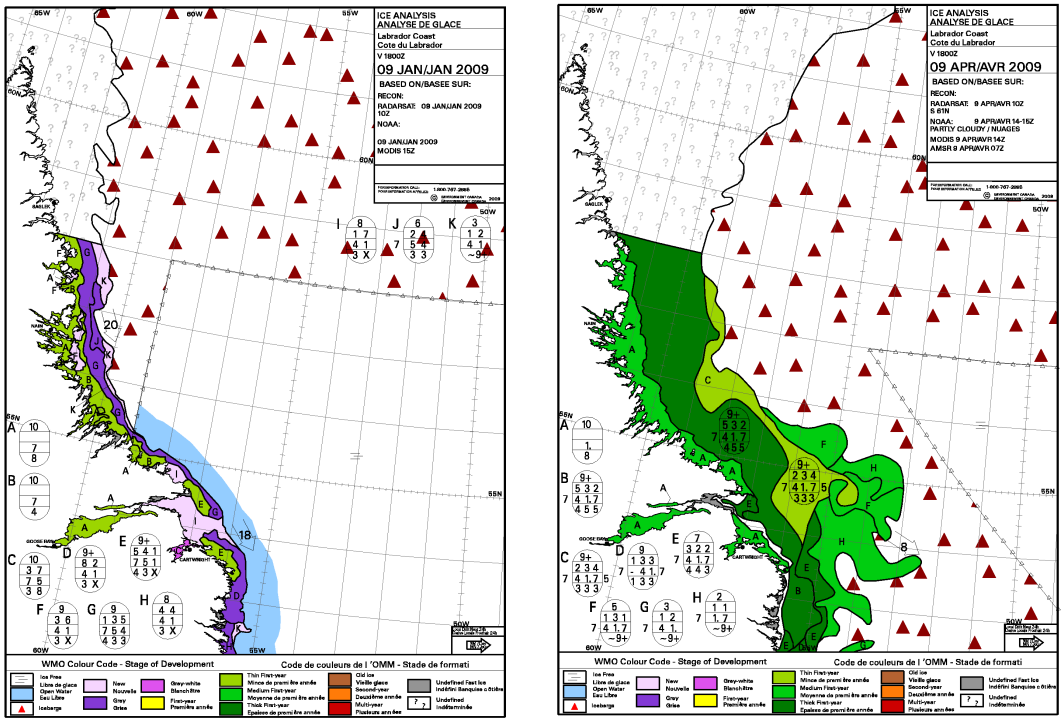

Figure 5.10: CIS ice chart: ice types for 09 January 2009 and 09 April 2009.

The video images on 02 March 2009 were analyzed and the results of ice concentration estimates from images, model, ice chart and AMSR-E are presented in the Table 5.1. Ice concentration estimates from images, model, and AMSR-E are also represented in the histogram of Figure 5.11. The model values remain in the range of $0 - 10\%$ error in ice concentration when compared with the ice chart. The values derived from the videos also remain in the range of $0 - 10\%$ error in ice concentration when compared with the ice chart. AMSR-E has an error of 10% in the areas where ice concentration is greater than 65% (see Section 3.6)[10]. At some stations, the model values are within the range of error of the AMSR-E. The deviations of model with AMSR-E at some stations may be due to the fact that AMSR-E is only assimilated at the ice edge.

Table 5.1: Ice concentration from images, model, ice chart and AMSR-E.

Lat	Lon	No. images	Image	Model	Ice chart	AMSR-E
54.8N	57.6W	9	94.81	85.57	90+	97
54.8N	57.5W	48	90.13	83.08	90+	96.33
54.8N	57.4W	45	85.08	83.64	90+	97.19
54.9N	57.4W	27	86.91	87.32	90+	99.28
54.9N	57.5W	26	89.27	83.84	90+	99.28
54.9N	57.6W	41	90.91	91.59	90+	99.64
55.9N	58.5W	46	79.69	86.86	90+	95.70
55.9N	58.4W	35	89.16	85.74	90+	92.73
56.0N	58.4W	43	90.21	83.11	90+	89.21

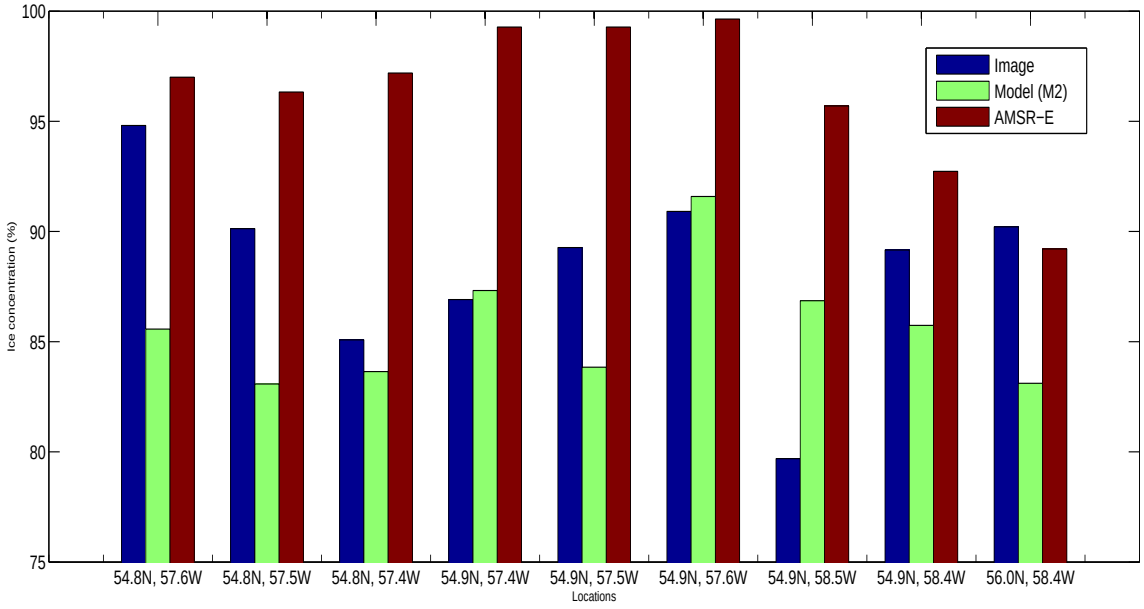

Figure 5.11: Ice concentration from images, model, and AMSR-E.

5.5 Conclusions

As mentioned in Chapter 4, the existing literature on assimilation uses a constant drag formulation and rarely discuss the effect of assimilating ice concentration on other parameters other than ice thickness. In this work the assimilated model results were compared with in situ measurements to derive and validate the parameters such as level ice draft and keel depth.

The level ice draft and keel values derived from ULS were compared with the modeled values. The coefficient that related the sail height and keel depth for the Makkovick region lies in a range $3-8$ depending on the period of the year. The ULS data and model results were in agreement, except for some differences which can be explained by the difference in spatial resolution of the model and ULS data. The ice concentration derived from video/image files obtained from fieldwork were compared

with the model data. Except in the case when shadows cast by icebergs/pressure ridges resulted in reduced ice concentration estimates, the results correlated well with ice concentration from the CIS ice chart. The model values lie in an error range of $0 - 10\%$ when compared with the values derived from the ice chart.

The assimilated model can be fine tuned to be used for deriving several of sea ice parameters such as ice concentration, thickness, freeboard, sail height and keel depth.

Bibliography

[1] P. f. C. C-CORE. Labrador Iceberg Survey-Field Report (R-08-087-678). 2009.

[2] G. Crocker and T. Carrieres. Documentation for the canadian ice service digital sea ice database. *Ballicater Consulting Ltd., Kingston, ON, Canada, Contract Rep. 00-02*, 2000.

[3] K. Evers and P. Jochmann. Determination of the topography of pressure ice ridges in the Laptev-Sea. *Peninsula*, 105(150):165, 1995.

[4] R. C. Gonzalez and R. E. Woods. Digital Image Processing, 2002.

[5] A. Palmer. *Arctic offshore engineering*. World Scientific, 2013.

[6] S. Prasad, I. Zakharov, P. Bobby, D. Power, P. McGuire, et al. Model Based Estimation of Sea Ice Parameters. In *Arctic Technology Conference*. Offshore Technology Conference, 2016.

[7] E. Ross, D. Fissel, G. Wyatt, N. Milutinovic, and J. Lawrence. Project report: Data processing and analysis of the ice draft and ice velocity, Makkovik Bank. 2014.

[8] C. I. Service. Manual of ice (manice), 2005.

[9] M. Shokr and N. Sinha. *Sea ice: physics and remote sensing.* John Wiley & Sons, 2015.

[10] G. Spreen, L. Kaleschke, and G. Heygster. Sea ice remote sensing using AMSR-E 89-GHz channels. *Journal of Geophysical Research: Oceans*, 113(C2), 2008.

[11] G. Timco, K. Croasdale, and B. Wright. An overview of first-year sea ice ridges. *PERD/CHC report*, pages 5–112, 2000.

[12] M. Tsamados, D. L. Feltham, D. Schroeder, D. Flocco, S. L. Farrell, N. Kurtz, S. W. Laxon, and S. Bacon. Impact of variable atmospheric and oceanic form drag on simulations of Arctic sea ice. *Journal of Physical Oceanography*, 44(5):1329–1353, 2014.

Chapter 6

Summary

6.1 Conclusions

The primary objective of this thesis was to retrieve sea ice parameters through the fusion of high resolution model data and remote sensing data, see Section 1.4. The objective has been successfully fulfilled, leading to the development of a data assimilated sea ice model for the Baffin Bay and Labrador region. The model can also be successfully configured to fit other regions of interest.

Chapter 1 discussed the relevance of sea ice information for various applications such as climate studies, transportation, marine biology, and offshore constructions. The Chapter also provided fundamental information on the physics of sea ice processes, observation of sea ice and a brief description of general equations that were used for modeling the process of sea ice ablation and growth.

Chapter 2 conducted a review of the remote sensing of sea ice, modeling of sea ice processes, data assimilation methods, and grid generation methods that were used in

the ice-ocean framework. Some of the methodologies and data resources discussed in the review section were applied to achieve the aforementioned research objective.

Chapter 3 described the implementation of a standalone sea ice model. The sea ice model, CICE that was used for the present study typically came with global grids and cyclic/periodic boundary conditions. The work illustrated the implementation of open boundaries for a regional configuration that includes Baffin Bay, Labrador Sea, Hudson Bay and Gulf of St. Lawrence. Usually, the ocean forcing for the model were derived from CCSM simulation results or coupled ocean models. For regional implementations, the study suggested a density-based mixed layer criteria for mixed layer slab ocean model. The standalone model results were validated using ice concentration data derived from AMSR-E/AMSR2 and OSI SAF. The RMSE of model estimated ice concentration and SST with the observation were high during the melt season mainly due to two factors, the assumption of zero mixed-layer heat flux and no-ice initial conditions. The spatial distribution of modeled ice concentration error were also discussed in the Chapter. The significance of work were the implementation of open boundaries for the regional configuration and use of density-based mixed layer criteria.

Chapter 4 described the implementation of combined optimal interpolation and nudging method to assimilate ice concentration and SST into the model. The assimilation of ice concentration required changes in ice volume and dependent tracers. The retrieved parameters such as ice concentration, thickness, and freeboard were compared with OSI SAF ice concentration products, ice thickness retrievals from SMOS, and freeboard retrievals CryoSat-2. The retrieved ice concentration results were found to improve with the assimilation. Other dependent parameters such as thickness, and

freeboard were compared with the SMOS and CryoSat-2 data respectively. The thin ice estimates from the model and SMOS data showed a good match between October and February. The deviations during March has to be further explored. The freeboard estimates from the model compared well with the freeboard estimates from CryoSat-2. The significance of the work included the direct assimilation of SST to correct the values of SST estimated by the mixed layer slab ocean models. Usually, SST is assimilated into the ocean model, and the information is passed on to the sea ice model. The assimilation of ice concentration includes the update of ice volume as well as dependent tracers.

Chapter 5 discussed a method to extract the level draft and keel measures from ULS data. The chapter also discussed the analysis of video image files to estimate ice concentration. The results derived from the ULS instrument combined with the model estimates were used to derive the coefficient that relates the sail and keel. With the present configuration of the model, the estimates was found to vary seasonally. The ice concentration estimated from the video image files compared well with the model except when there was the least shadow cast by the ridges or icebergs. The significance of the work was the comparison of the updates of level draft and keel of model estimates with the ULS measurements. The study has to be extended further by a sensitivity analysis of the parameters that affect the variable drag coefficient.

The objectives of the research were achieved in Chapters 3, 4 and 5. The model has been implemented on a regional scale with open boundaries and suggested density-based mixed layer criteria to implement the model in standalone mode. The previous literature on the model implementation uses the parameters that were derived from ocean models passed on to the sea ice model. Moreover, the use of variable drag

coefficients required adjustments to the tracers such as ice volume, melt ponds, level ice that depend on sea ice concentration. The present study is a variation from the use of constant drag coefficients in the previous literature on assimilation studies. Also, direct assimilation of SST in the sea ice model seems to improve the model results. The previous studies assimilate the SST in the ocean model and then passes the information to the sea ice model. The model estimated ice concentration, thickness, and freeboard shows improvement by assimilating ice concentration and SST. The current estimates can be tuned to achieve better results by doing a sensitivity analysis on the parameters related to computation of variable drag such as melt ponds and ridges and also, by fine-tuning of the assimilation parameters.

6.2 Future work

There are many areas that can be the focus of future work.

Sea ice modeling

The modeling part still lacks the consideration of salinity variation and mixed-layer heat flux. A methodology similar to that used by Petty et al. [5] or the methodology suggested by Kraus and Turner [2] or Niiler and Kraus [4] can be used to improve the mixed-layer model used to estimate the formation/ablation of sea ice. Another area of interest would be a parametrization to include thermal conductivity of snow that depends on the thermal conductivity of ice instead of considering a constant value [3].

Data assimilation

The data assimilation methodology can be improved through combined information

from multiple sensors and extending the optimal interpolation method used in the present work [1], or by direct assimilation of brightness values in the model [6], or by including a fusion of data from various sources and using the same methodology as described in Chapter 4. Possibilities also lie in exploring methodologies to assimilate thickness data [7] and dependent tracers.

Bibliography

[1] R. Daley. Atmospheric data analysis, Cambridge atmospheric and space science series. *Cambridge University Press*, 6966:25, 1991.

[2] E. B. Kraus and J. S. Turner. A one-dimensional model of the seasonal thermocline II. The general theory and its consequences. *Tellus*, 19(1):98–106, 1967.

[3] O. Lecomte, T. Fichefet, M. Vancoppenolle, F. Domine, F. Massonnet, P. Mathiot, S. Morin, and P.-Y. Barriat. On the formulation of snow thermal conductivity in large-scale sea ice models. *Journal of Advances in Modeling Earth Systems*, 5(3):542–557, 2013.

[4] P. Niiler. One-dimensional models of the upper ocean, Modelling and Prediction of the Upper Layers of the Ocean EB Kraus, 1977.

[5] A. A. Petty, P. R. Holland, and D. L. Feltham. Sea ice and the ocean mixed layer over the Antarctic shelf seas. *Cryosphere*, 8(2):761–783, 2014.

[6] K. A. Scott, M. Buehner, A. Caya, and T. Carrieres. Direct assimilation of AMSR-E brightness temperatures for estimating sea ice concentration. *Monthly Weather Review*, 140(3):997–1013, 2012.

[7] Q. Yang, S. N. Losa, M. Losch, X. Tian-Kunze, L. Nerger, J. Liu, L. Kaleschke, and Z. Zhang. Assimilating SMOS sea ice thickness into a coupled ice-ocean model using a local SEIK filter. *Journal of Geophysical Research: Oceans*, 119(10):6680–6692, 2014.

Bibliography

[1] *The Los Angeles Times September*. 2012.

[2] A. Adcroft, J. Campin, S. Dutkiewicz, C. Evangelinos, D. Ferreira, G. Forget, B. Fox-Kemper, P. Heimbach, C. Hill, E. Hill, et al. MITgcm user manual, 2008.

[3] T. Afifi and J. Jäger. *Environment, forced migration and social vulnerability*. Springer, 2010.

[4] E. L. Andreas, R. E. Jordan, and A. P. Makshtas. Simulations of snow, ice, and near-surface atmospheric processes on Ice Station Weddell. *Journal of Hydrometeorology*, 5(4):611–624, 2004.

[5] A. Arakawa and V. R. Lamb. Methods of computational physics. *Academic Press*, 17:174–265, 1977.

[6] M. Arkett, D. Flett, and R. De Abreu. C-band multiple polarization SAR for ice monitoring–What can it do for the Canadian ice service. 2003.

[7] M. Arkett, D. Flett, R. De Abreu, P. Clemente-Colón, J. Woods, and B. Melchior. Evaluating ALOS-PALSAR for ice monitoring-what can L-band do for

the North American ice service? In *Geoscience and Remote Sensing Symposium, 2008. IGARSS 2008. IEEE International*, volume 5, pages V–188. IEEE, 2008.

[8] K. R. Arrigo, D. K. Perovich, R. S. Pickart, Z. W. Brown, G. L. Van Dijken, K. E. Lowry, M. M. Mills, M. A. Palmer, W. M. Balch, F. Bahr, et al. Massive phytoplankton blooms under Arctic sea ice. *Science*, 336(6087):1408–1408, 2012.

[9] M. Asch, M. Bocquet, and M. Nodet. *Data assimilation: methods, algorithms, and applications*. SIAM, 2016.

[10] J. Askne, A. Carlstrom, W. Dierking, and L. Ulander. ERS-1 SAR backscatter modeling and interpretation of sea ice signatures. In *Geoscience and Remote Sensing Symposium, 1994. IGARSS'94. Surface and Atmospheric Remote Sensing: Technologies, Data Analysis and Interpretation., International*, volume 1, pages 162–164. IEEE, 1994.

[11] E. Bailey, D. Feltham, and P. Sammonds. A model for the consolidation of rafted sea ice. *Journal of Geophysical Research: Oceans*, 115(C4), 2010.

[12] H. M. Barré, B. Duesmann, and Y. H. Kerr. SMOS: The mission and the system. *IEEE Transactions on Geoscience and Remote Sensing*, 46(3):587–593, 2008.

[13] W. Bell. A preprocessor for SSMIS radiances scientific description. *Met Office, UK*, 2006.

[14] C. M. Bitz. Numerical modeling of sea ice in the climate system, 2008.

[15] C. M. Bitz and W. H. Lipscomb. An energy-conserving thermodynamic model of sea ice. *Journal of Geophysical Research: Oceans*, 104(C7):15669–15677, 1999.

[16] E. Bjørgo, O. M. Johannessen, and M. W. Miles. Analysis of merged SMMR-SSMI time series of Arctic and Antarctic sea ice parameters 1978–1995. *Geophysical Research Letters*, 24(4):413–416, 1997.

[17] F. Bouttier and P. Courtier. Data assimilation concepts and methods March 1999. *Meteorological Training Course Lecture Series. ECMWF*, page 59, 2002.

[18] C. Bouzinac. CryoSat product handbook. *ESA User Manual, ESA, ESRIN, Italy*, 4121:4123, 2014.

[19] B. Briegleb and B. Light. A Delta-Eddington multiple scattering parameterization for solar radiation in the sea ice component of the Community Climate System Model. *NCAR Tech. Note NCAR/TN-472+ STR*, pages 1–108, 2007.

[20] P. f. C. C-CORE. Labrador Iceberg Survey-Field Report (R-08-087-678). 2009.

[21] W. J. Campbell. The wind-driven circulation of ice and water in a polar ocean. *Journal of Geophysical Research*, 70(14):3279–3301, 1965.

[22] F. D. Carsey. *Microwave remote sensing of sea ice*. American Geophysical Union, 1992.

[23] A. Caya, M. Buehner, and T. Carrieres. Analysis and forecasting of sea ice conditions with three-dimensional variational data assimilation and a coupled

ice–ocean model. *Journal of Atmospheric and Oceanic Technology*, 27(2):353–369, 2010.

[24] A. Caya, M. Buehner, M. Shokr, and T. Carrieres. A first attempt of data assimilation for operational sea ice monitoring in Canada. In *Geoscience and Remote Sensing Symposium, 2006. IGARSS 2006. IEEE International Conference on*, pages 1705–1708. IEEE, 2006.

[25] B. Cheng, T. Vihma, M. Arkett, T. Carrieres, et al. A method for sea ice thickness and concentration analysis based on SAR data and a thermodynamic model. *Cryosphere*, 6(6):1507, 2012.

[26] P. Christie and M. Sommerkorn. RACER: Rapid assessment of circum-Arctic ecosystem resilience. *Ottawa, Canada: WWF Global Arctic Programme*, 2012.

[27] A. Ciappa and L. Pietranera. High resolution observations of the Terra Nova Bay polynya using COSMO-SkyMed X-SAR and other satellite imagery. *Journal of Marine Systems*, 113:42–51, 2013.

[28] M. Coon, G. Maykut, and R. Pritchard. Modeling the pack ice as an elastic-plastic material. 1974.

[29] G. Cox and W. Weeks. Numerical simulations of the profile properties of undeformed first-year sea ice during the growth season. *Journal of Geophysical Research: Oceans*, 93(C10):12449–12460, 1988.

[30] G. Crocker and T. Carrieres. Documentation for the canadian ice service digital sea ice database. *Ballicater Consulting Ltd., Kingston, ON, Canada, Contract Rep. 00-02*, 2000.

[31] J. A. Curry, J. L. Schramm, and E. E. Ebert. Sea ice-albedo climate feedback mechanism. *Journal of Climate*, 8(2):240–247, 1995.

[32] R. Daley. Atmospheric data analysis, Cambridge atmospheric and space science series. *Cambridge University Press*, 6966:25, 1991.

[33] R. De Abreu, D. Flett, B. Scheuchl, and B. Ramsay. Operational sea ice monitoring with RADARSAT-2-a glimpse into the future. In *Geoscience and Remote Sensing Symposium, 2003. IGARSS'03. Proceedings. 2003 IEEE International*, volume 2, pages 1308–1310. IEEE, 2003.

[34] T. L. Delworth and M. E. Mann. Observed and simulated multidecadal variability in the northern hemisphere. *Climate Dynamics*, 16(9):661–676, 2000.

[35] R. Deutch. Estimation theory. 1965.

[36] S. T. Dokken, P. Winsor, T. Markus, J. Askne, and G. Björk. ERS SAR characterization of coastal polynyas in the Arctic and comparison with SSM/I and numerical model investigations. *Remote Sensing of Environment*, 80(2):321–335, 2002.

[37] R. Drucker, S. Martin, and R. Moritz. Observations of ice thickness and frazil ice in the St. Lawrence Island polynya from satellite imagery, upward looking

sonar, and salinity/temperature moorings. *Journal of Geophysical Research: Oceans*, 108(C5), 2003.

[38] L. Dzierzbicka-Glowacka, M. Janecki, A. Nowicki, and J. Jakacki. A new marine ecosystem 3D CEMBS model (version 2) for the Baltic Sea. In *Complex Systems (ICCS), 2012 International Conference on*, pages 1–6. IEEE, 2012.

[39] E. E. Ebert and J. A. Curry. An intermediate one-dimensional thermodynamic sea ice model for investigating ice–atmosphere interactions. *Journal of Geophysical Research: Oceans*, 98(C6):10085–10109, 1993.

[40] W. Emery, M. Radebaugh, C. Fowler, D. Cavalieri, and K. Steffen. A comparison of sea ice parameters computed from advanced very high resolution radiometer and Landsat satellite imagery and from airborne passive microwave radiometry. *Journal of Geophysical Research: Oceans*, 96(C12):22075–22085, 1991.

[41] Environment Canada. Sea ice trends in canada, 2011.

[42] K. Evers and P. Jochmann. Determination of the topography of pressure ice ridges in the Laptev-Sea. *Peninsula*, 105(150):165, 1995.

[43] R. Ezraty, F. Girard-Ardhuin, and D. Croizé-Fillon. Sea ice drift in the central Arctic using the 89 GHz brightness temperatures of the Advanced Microwave Scanning Radiometer. *Users Manual, IFREMER, Brest, France*, 2007.

[44] D. Feltham, N. Untersteiner, J. Wettlaufer, and M. Worster. Sea ice is a mushy layer. *Geophysical Research Letters*, 33(14), 2006.

[45] I. Fenty and P. Heimbach. Coupled sea ice–ocean-state estimation in the Labrador Sea and Baffin Bay. *Journal of Physical Oceanography*, 43(5):884–904, 2013.

[46] M. Fily and D. Rothrock. Sea ice tracking by nested correlations. *IEEE Transactions on Geoscience and Remote Sensing*, (5):570–580, 1987.

[47] R. C. Gonzalez and R. E. Woods. Digital Image Processing, 2002.

[48] S. Häkkinen. An arctic source for the great salinity anomaly: A simulation of the arctic ice-ocean system for 1955–1975. *Journal of Geophysical Research: Oceans*, 98(C9):16397–16410, 1993.

[49] M. Hallikainen and D. P. Winebrenner. The physical basis for sea ice remote sensing. *Microwave Remote Sensing of Sea ice*, pages 29–46, 1992.

[50] D. Haverkamp, L. K. Soh, and C. Tsatsoulis. A comprehensive, automated approach to determining sea ice thickness from SAR data. *IEEE Transactions on Geoscience and Remote Sensing*, 33(1):46–57, 1995.

[51] K. S. Hedström. *Technical manual for a coupled sea-ice/ocean circulation model (version 3)*. Citeseer, 2009.

[52] S. Hendricks, R. Ricker, and V. Helm. AWI CryoSat-2 Sea Ice Thickness Data Product. *Data product manual, Alfred-Wegener-Institut*, 2013.

[53] W. Hibler. Differential sea-ice drift. II. Comparison of mesoscale strain measurements to linear drift theory predictions. *Journal of Glaciology*, 13(69):457–471, 1974.

[54] W. Hibler III. A dynamic thermodynamic sea ice model. *Journal of Physical Oceanography*, 9(4):815–846, 1979.

[55] W. Hibler Iii. Modeling a variable thickness sea ice cover. *Monthly weather review*, 108(12):1943–1973, 1980.

[56] W. Hibler III and K. Bryan. A diagnostic ice–ocean model. *Journal of Physical Oceanography*, 17(7):987–1015, 1987.

[57] J. E. Hoke and R. A. Anthes. The initialization of numerical models by a dynamic-initialization technique. *Monthly Weather Review*, 104(12):1551–1556, 1976.

[58] M. M. Holland and C. M. Bitz. Polar amplification of climate change in coupled models. *Climate Dynamics*, 21(3-4):221–232, 2003.

[59] T. Hollands, V. Haid, W. Dierking, R. Timmermann, and L. Ebner. Sea ice motion and open water area at the Ronne Polynia, Antarctica: Synthetic aperture radar observations versus model results. *Journal of Geophysical Research: Oceans*, 118(4):1940–1954, 2013.

[60] P. L. Houtekamer and H. L. Mitchell. Data assimilation using an ensemble Kalman filter technique. *Monthly Weather Review*, 126(3):796–811, 1998.

[61] E. Hunke and J. Dukowicz. An elastic–viscous–plastic model for sea ice dynamics. *Journal of Physical Oceanography*, 27(9):1849–1867, 1997.

[62] E. C. Hunke. Thickness sensitivities in the CICE sea ice model. *Ocean Modelling*, 34(3):137–149, 2010.

[63] E. C. Hunke, W. H. Lipscomb, and A. K. Turner. Sea-ice models for climate study: retrospective and new directions. *Journal of Glaciology*, 56(200):1162–1172, 2010.

[64] E. C. Hunke, W. H. Lipscomb, A. K. Turner, N. Jeffery, and S. Elliott. CICE: the Los Alamos Sea Ice Model Documentation and Software Users Manual Version 5.1 LA-CC-06-012. *T-3 Fluid Dynamics Group, Los Alamos National Laboratory*, 675, 2015.

[65] K. Imaoka, M. Kachi, M. Kasahara, N. Ito, K. Nakagawa, and T. Oki. Instrument performance and calibration of AMSR-E and AMSR2. *International Archives of the Photogrammetry, Remote Sensing and Spatial Information Science*, 38(8):13–18, 2010.

[66] R. Ingram and S. Prinsenberg. Coastal oceanography of Hudson Bay and surrounding eastern Canadian Arctic waters. *The Sea*, 11(29):835–859, 1998.

[67] B. Ip, W. Hibler, and G. Flato. The Effect Of Rheology On Seasonal Sea-Ice Simulations. *Annals of Glaciology*, 14:340–340, 1990.

[68] A. Jazwinski. Stochastic Process and Filtering Theory, Academic Press. *A subsidiary of Harcourt Brace Jovanovich Publishers*, 1970.

[69] O. M. Johannessen, V. Alexandrov, I. Y. Frolov, S. Sandven, L. H. Pettersson, L. P. Bobylev, K. Kloster, V. G. Smirnov, Y. U. Mironov, and N. G. Babich. *Remote sensing of sea ice in the Northern Sea Route: studies and applications*. Springer Science & Business Media, 2006.

[70] M. Johnson, A. Proshutinsky, Y. Aksenov, A. T. Nguyen, R. Lindsay, C. Haas, J. Zhang, N. Diansky, R. Kwok, W. Maslowski, et al. Evaluation of Arctic sea ice thickness simulated by Arctic Ocean Model Intercomparison Project models. *Journal of Geophysical Research: Oceans*, 117(C8), 2012.

[71] L. Kaleschke, X. Tian-Kunze, N. Maaß, G. Heygster, M. Huntemann, H. Wang, and C. Haas. SMOS Sea Ice Retrieval Study (SMOSIce), ESA Support To Science Element (STSE), Final Report ESA ESTEC contract no. Technical report, 4000101476/10/NL/CT, 2013.

[72] L. Kaleschke, X. Tian-Kunze, N. Maaß, M. Mäkynen, and M. Drusch. Sea ice thickness retrieval from SMOS brightness temperatures during the Arctic freeze-up period. *Geophysical Research Letters*, 39(5), 2012.

[73] E. Kalnay. *Atmospheric modeling, data assimilation and predictability*. Cambridge University Press, 2003.

[74] Y. H. Kerr, P. Waldteufel, J.-P. Wigneron, J. Martinuzzi, J. Font, and M. Berger. Soil moisture retrieval from space: The Soil Moisture and Ocean Salinity (SMOS) mission. *IEEE transactions on Geoscience and remote sensing*, 39(8):1729–1735, 2001.

[75] J.-W. Kim, D.-j. Kim, and B. J. Hwang. Characterization of Arctic sea ice thickness using high-resolution spaceborne polarimetric SAR data. *IEEE Transactions on Geoscience and Remote Sensing*, 50(1):13–22, 2012.

[76] R. E. Kistler. *A study of data assimilation techniques in an autobarotropic, primitive equation, channel model*. PhD thesis, Pennsylvania State University, 1974.

[77] A. S. Komarov and D. G. Barber. Sea ice motion tracking from sequential dual-polarization RADARSAT-2 images. *IEEE Transactions on Geoscience and Remote Sensing*, 52(1):121–136, 2014.

[78] E. B. Kraus and J. S. Turner. A one-dimensional model of the seasonal thermocline II. The general theory and its consequences. *Tellus*, 19(1):98–106, 1967.

[79] N. Kurtz, S. Farrell, M. Studinger, N. Galin, J. Harbeck, R. Lindsay, V. Onana, B. Panzer, and J. Sonntag. Sea ice thickness, freeboard, and snow depth products from Operation IceBridge airborne data. 2013.

[80] R. Kwok. Exchange of sea ice between the Arctic Ocean and the Canadian Arctic Archipelago. *Geophysical Research Letters*, 33(16), 2006.

[81] R. Kwok and G. Cunningham. ICESat over Arctic sea ice: Estimation of snow depth and ice thickness. *Journal of Geophysical Research: Oceans*, 113(C8), 2008.

[82] S. Lakshmivarahan and J. M. Lewis. Nudging methods: a critical overview. In *Data Assimilation for Atmospheric, Oceanic and Hydrologic Applications (Vol. II)*, pages 27–57. Springer, 2013.

[83] K. Law, A. Stuart, and K. Zygalakis. *Data assimilation: a mathematical introduction*, volume 62. Springer, 2015.

[84] S. Laxon, N. Peacock, and D. Smith. High interannual variability of sea ice thickness in the Arctic region. *Nature*, 425(6961):947–950, 2003.

[85] F.-X. Le Dimet, I. M. Navon, and R. Ştefănescu. Variational data assimilation: optimization and optimal control. In *Data Assimilation for Atmospheric, Oceanic and Hydrologic Applications (Vol. III)*, pages 1–53. Springer, 2017.

[86] O. Lecomte, T. Fichefet, M. Vancoppenolle, F. Domine, F. Massonnet, P. Mathiot, S. Morin, and P.-Y. Barriat. On the formulation of snow thermal conductivity in large-scale sea ice models. *Journal of Advances in Modeling Earth Systems*, 5(3):542–557, 2013.

[87] S. Levitus et al. The world ocean database. *Data Science Journal*, 12:WDS229–WDS234, 2013.

[88] Lindsay, RW and Zhang, J. Assimilation of ice concentration in an ice–ocean model. *Journal of Atmospheric and Oceanic Technology*, 23(5):742–749, 2006.

[89] W. H. Lipscomb. Remapping the thickness distribution in sea ice models. *Journal of Geophysical Research: Oceans*, 106(C7):13989–14000, 2001.

[90] W. H. Lipscomb and E. C. Hunke. Modeling sea ice transport using incremental remapping. *Monthly Weather Review*, 132(6):1341–1354, 2004.

[91] W. H. Lipscomb, E. C. Hunke, W. Maslowski, and J. Jakacki. Ridging, strength, and stability in high-resolution sea ice models. *Journal of Geophysical Research: Oceans*, 112(C3), 2007.

[92] P. Lu, Z. Li, B. Cheng, and M. Leppäranta. A parameterization of the ice-ocean drag coefficient. *Journal of Geophysical Research: Oceans*, 116(C7), 2011.

[93] C. Lüpkes, V. M. Gryanik, J. Hartmann, and E. L. Andreas. A parametrization, based on sea ice morphology, of the neutral atmospheric drag coefficients for weather prediction and climate models. *Journal of Geophysical Research: Atmospheres*, 117(D13), 2012.

[94] G. Madec and M. Imbard. A global ocean mesh to overcome the North Pole singularity. *Climate Dynamics*, 12(6):381–388, 1996.

[95] J. Maslanik, C. Fowler, J. Key, T. Scambos, T. Hutchinson, and W. Emery. AVHRR-based Polar Pathfinder products for modeling applications. *Annals of Glaciology*, 25:388–392, 1997.

[96] F. Massonnet, T. Fichefet, H. Goosse, M. Vancoppenolle, P. Mathiot, and C. K. Beatty. On the influence of model physics on simulations of Arctic and Antarctic sea ice. *Cryosphere*, 5(3):687, 2011.

[97] G. A. Maykut. Large-scale heat exchange and ice production in the central Arctic. *Journal of Geophysical Research: Oceans*, 87(C10):7971–7984, 1982.

[98] G. A. Maykut and N. Untersteiner. Some results from a time-dependent thermodynamic model of sea ice. *Journal of Geophysical Research*, 76(6):1550–1575, 1971.

[99] G. L. Mellor and S. Häkkinen. A review of coupled ice-ocean models. *The Polar Oceans and Their Role in Shaping the Global Environment*, pages 21–31, 1994.

[100] G. Mertz and R. Myers. The ecological impact of the Great Salinity Anomaly in the northern North-west Atlantic. *Fisheries Oceanography*, 3(1):1–14, 1994.

[101] F. Mesinger, G. DiMego, E. Kalnay, K. Mitchell, P. C. Shafran, W. Ebisuzaki, D. Jović, J. Woollen, E. Rogers, E. H. Berbery, et al. North American regional reanalysis. *Bulletin of the American Meteorological Society*, 87(3):343–360, 2006.

[102] P. A. Miller, S. W. Laxon, and D. L. Feltham. Improving the spatial distribution of modeled Arctic sea ice thickness. *Geophysical Research Letters*, 32(18), 2005.

[103] S. Muckenhuber and S. Sandven. Open-source sea ice drift algorithm for Sentinel-1 SAR imagery using a combination of feature tracking and pattern matching. *Cryosphere*, 11(4):1835, 2017.

[104] R. J. Murray. Explicit generation of orthogonal grids for ocean models. *Journal of Computational Physics*, 126(2):251–273, 1996.

[105] S. Nghiem and C. Bertoia. Study of multi-polarization C-band backscatter signatures for Arctic sea ice mapping with future satellite SAR. *Canadian Journal of Remote Sensing*, 27(5):387–402, 2001.

[106] P. Niiler. One-dimensional models of the upper ocean, Modelling and Prediction of the Upper Layers of the Ocean EB Kraus, 1977.

[107] R. Ninnis, W. Emery, and M. Collins. Automated extraction of pack ice motion from advanced very high resolution radiometer imagery. *Journal of Geophysical Research: Oceans*, 91(C9):10725–10734, 1986.

[108] NSIDC. "All About Sea Ice." National Snow and Ice Data Center. `https://nsidc.org/cryosphere/seaice/index.html`. Accessed: 2013-10-15.

[109] A. Palmer. *Arctic offshore engineering*. World Scientific, 2013.

[110] S. K. Park and L. Xu. *Data assimilation for atmospheric, oceanic and hydrologic applications*, volume 2. Springer Science & Business Media, 2013.

[111] C. L. Parkinson and W. M. Washington. A large-scale numerical model of sea ice. *Journal of Geophysical Research: Oceans*, 84(C1):311–337, 1979.

[112] L. T. Pedersen. Merging microwave radiometer data and meteorological data for improved sea ice concentrations. *EARSeL Advances in Remote Sensing*, 3(2-XII):81–89, 1994.

[113] L. T. Pedersen and M. D. Coon. A sea ice model for the marginal ice zone with an application to the Greenland Sea. *Journal of Geophysical Research: Oceans*, 109(C3), 2004.

[114] A. A. Petty, P. R. Holland, and D. L. Feltham. Sea ice and the ocean mixed layer over the Antarctic shelf seas. *Cryosphere*, 8(2):761–783, 2014.

[115] D. T. Pham. Stochastic methods for sequential data assimilation in strongly nonlinear systems. *Monthly weather review*, 129(5):1194–1207, 2001.

[116] D. T. Pham, J. Verron, and M. C. Roubaud. A singular evolutive extended Kalman filter for data assimilation in oceanography. *Journal of Marine systems*, 16(3):323–340, 1998.

[117] G. L. Pickard and W. J. Emery. *Descriptive physical oceanography: an introduction*. Elsevier, 2016.

[118] S. Prasad, I. Zakharov, and P. Bobby. Model Based Estimation of Sea Ice Characteristics in the Region of Baffin Bay and the Labrador Sea. *Journal of Ocean Technology*, 11(1):39–47, 2016.

[119] S. Prasad, I. Zakharov, P. Bobby, and P. McGuire. The implementation of sea ice model on a regional high-resolution scale. *Ocean Dynamics*, 65(9-10):1353–1366, 2015.

[120] S. Prasad, I. Zakharov, P. Bobby, D. Power, P. McGuire, et al. Model Based Estimation of Sea Ice Parameters. In *Arctic Technology Conference*. Offshore Technology Conference, 2016.

[121] D. Pringle, H. Eicken, H. Trodahl, and L. Backstrom. Thermal conductivity of landfast Antarctic and Arctic sea ice. *Journal of Geophysical Research: Oceans*, 112(C4), 2007.

[122] R. Pritchard, M. Coon, and M. McPhee. Simulation of sea ice dynamics during AIDJEX. *Journal of Pressure Vessel Technology*, 99(3):491–497, 1977.

[123] J. Rae, H. Hewitt, A. Keen, J. Ridley, A. West, C. Harris, E. Hunke, and D. Walters. Development of the Global Sea Ice 6.0 CICE configuration for the Met Office Global coupled model. *Geoscientific Model Development*, 8(7):2221–2230, 2015.

[124] J. P. Rafferty et al. *Oceans and oceanography*. Britannica Educational Publishing, 2010.

[125] P. Rampal, S. Bouillon, E. Ólason, and M. Morlighem. neXtSIM: a new Lagrangian sea ice model. *Cryosphere*, 10(3), 2016.

[126] R. Ressel, A. Frost, and S. Lehner. A neural network-based classification for sea ice types on X-band SAR images. *IEEE Journal of Selected Topics in Applied Earth Observations and Remote Sensing*, 8(7):3672–3680, 2015.

[127] R. W. Reynolds, T. M. Smith, C. Liu, D. B. Chelton, K. S. Casey, and M. G. Schlax. Daily high-resolution-blended analyses for sea surface temperature. *Journal of Climate*, 20(22):5473–5496, 2007.

[128] R. Ricker, S. Hendricks, V. Helm, H. Skourup, and M. Davidson. Sensitivity of CryoSat-2 Arctic sea-ice freeboard and thickness on radar-waveform interpretation. *Cryosphere*, 8(4):1607–1622, 2014.

[129] R. Ricker, S. Hendricks, L. Kaleschke, and X. Tian-Kunze. CS2SMOS: Weekly Arctic Sea-Ice Thickness Data Record, 2016.

[130] E. Ross, D. Fissel, G. Wyatt, N. Milutinovic, and J. Lawrence. Project report: Data processing and analysis of the ice draft and ice velocity, Makkovik Bank. 2014.

[131] S. Sandven, O. M. Johannessen, and K. Kloster. Sea ice monitoring by remote sensing. *Encyclopedia of Analytical Chemistry*, 2006.

[132] Y. Sasaki. Some basic formalisms in numerical variational analysis. *Monthly Weather Review*, 98(12):875–883, 1970.

[133] M. Sayed, T. Carrieres, et al. Overview of a new operational ice model. In *The Ninth International Offshore and Polar Engineering Conference*. International Society of Offshore and Polar Engineers, 1999.

[134] M. Sayed, T. Carrieres, H. Tran, S. B. Savage, et al. Development of an operational ice dynamics model for the Canadian Ice Service. In *The Twelfth International Offshore and Polar Engineering Conference*. International Society of Offshore and Polar Engineers, 2002.

[135] M. Sayed, S. Savage, and T. Carrieres. Examination of Ice Ridging Methods Using Discrete Particles. In *Proceedings 16th International Conference on Port and Ocean Engineering under Arctic Conditions (POAC'01)*, pages 1087–1096, 2001.

[136] M. Scagliola. CryoSat footprints Aresys technical note. *SAR-CRY2-TEN-6331, Aresys/ESA, Italy*, 2013.

[137] B. Scheuchl, D. Flett, R. Caves, and I. Cumming. Potential of RADARSAT-2 data for operational sea ice monitoring. *Canadian Journal of Remote Sensing*, 30(3):448–461, 2004.

[138] K. A. Scott, M. Buehner, A. Caya, and T. Carrieres. Direct assimilation of AMSR-E brightness temperatures for estimating sea ice concentration. *Monthly Weather Review*, 140(3):997–1013, 2012.

[139] A. J. Semtner Jr. A model for the thermodynamic growth of sea ice in numerical investigations of climate. *Journal of Physical Oceanography*, 6(3):379–389, 1976.

[140] G.-H. Seo, S. Kim, B.-J. Choi, Y.-K. Cho, and Y.-H. Kim. Implementation of the ensemble Kalman filter into a Northwest Pacific Ocean circulation model. *Data Assimilation for Atmospheric, Oceanic and Hydrologic Applications*, pages 341–352, 2009.

[141] C. I. Service. Manual of ice (manice), 2005.

[142] M. Shokr and N. Sinha. *Sea ice: physics and remote sensing*. John Wiley & Sons, 2015.

[143] M. E. Shokr. Evaluation of second-order texture parameters for sea ice classification from radar images. *Journal of Geophysical Research: Oceans*, 96(C6):10625–10640, 1991.

[144] L. H. Smedsrud, W. P. Budgell, A. D. Jenkins, et al. Fine-scale sea-ice modelling of the Storfjorden polynya, Svalbard. *Annals of Glaciology*, 44(1):73–79, 2006.

[145] T. M. Smith. A long-term record of blended satellite and in situ sea-surface temperature for climate monitoring, modeling and environmental studies. *Earth System Science Data*, 8(1):165, 2016.

[146] G. Spreen, L. Kaleschke, and G. Heygster. Sea ice remote sensing using AMSR-E 89-GHz channels. *Journal of Geophysical Research: Oceans*, 113(C2), 2008.

[147] J. D. Stark, J. Ridley, M. Martin, and A. Hines. Sea ice concentration and motion assimilation in a sea ice- ocean model. *Journal of Geophysical Research: Oceans*, 113(C5), 2008.

[148] J. Stefan. Ueber die Theorie der Eisbildung insbesondere uebcr die Eisbildung im Polarmeere. *Ann. Phvs. Chem. NF 42, 269*, 286, 1891.

[149] I. Stirling. The biological importance of polynyas in the Canadian Arctic. *Arctic*, pages 303–315, 1980.

[150] V. H. Strass. Measuring sea ice draft and coverage with moored upward looking sonars. *Deep Sea Research Part I: Oceanographic Research Papers*, 45(4-5):795–818, 1998.

[151] N. Sun and F. Weng. Evaluation of special sensor microwave imager/sounder (SSMIS) environmental data records. *IEEE Transactions on Geoscience and Remote Sensing*, 46(4):1006–1016, 2008.

[152] Y. Sun. Automatic ice motion retrieval from ERS-1 SAR images using the optical flow method. *International Journal of Remote Sensing*, 17(11):2059–2087, 1996.

[153] D. N. Thomas. *Sea ice*. John Wiley & Sons, 2017.

[154] A. Thorndike, D. Rothrock, G. Maykut, and R. Colony. The thickness distribution of sea ice. *Journal of Geophysical Research*, 80(33):4501–4513, 1975.

[155] X. Tian-Kunze and L. Kaleschke. *Read-me-first note for the release of the SMOS Level 3 ice thickness data product*. University of Hamburg, 2016.

[156] X. Tian-Kunze, L. Kaleschke, N. Maaß, M. Mäkynen, N. Serra, M. Drusch, and T. Krumpen. SMOS-derived thin sea ice thickness: algorithm baseline, product specifications and initial verification. *Cryosphere*, 8(3):997–1018, 2014.

[157] S. Tietsche, M. Alonso-Balmaseda, P. Rosnay, H. Zuo, X. Tian-Kunze, and L. Kaleschke. Thin sea ice in the arctic: comparing l-band radiometry retrievals with an ocean reanalysis.

[158] S. Tietsche, M. Balmaseda, H. Zuo, and P. de Rosnay. *Comparing Arctic Winter Sea-ice Thickness from SMOS and ORAS5*. European Centre for Medium-Range Weather Forecasts, 2017.

[159] G. Timco and R. Burden. An analysis of the shapes of sea ice ridges. *Cold Regions Science and Technology*, 25(1):65–77, 1997.

[160] G. Timco, K. Croasdale, and B. Wright. An overview of first-year sea ice ridges. *PERD/CHC report*, pages 5–112, 2000.

[161] R. Tonboe, J. Lavelle, R.-H. Pfeiffer, and E. Howe. Product User Manual for OSI SAF Global Sea Ice Concentration. 2016.

[162] R. Tonboe, L. Pedersen, and C. Haas. Simulation of the satellite radar altimeter sea ice thickness retrieval uncertainty. *The Cryosphere Discussions*, 3(2):513–559, 2009.

[163] M. Tsamados, D. L. Feltham, D. Schroeder, D. Flocco, S. L. Farrell, N. Kurtz, S. W. Laxon, and S. Bacon. Impact of variable atmospheric and oceanic

form drag on simulations of Arctic sea ice. *Journal of Physical Oceanography*, 44(5):1329–1353, 2014.

[164] M. Tsamados, D. L. Feltham, and A. Wilchinsky. Impact of a new anisotropic rheology on simulations of Arctic sea ice. *Journal of Geophysical Research: Oceans*, 118(1):91–107, 2013.

[165] A. K. Turner, E. C. Hunke, and C. M. Bitz. Two modes of sea-ice gravity drainage: A parameterization for large-scale modeling. *Journal of Geophysical Research: Oceans*, 118(5):2279–2294, 2013.

[166] N. Untersteiner. On the mass and heat budget of Arctic sea ice. *Archiv für Meteorologie, Geophysik und Bioklimatologie, Serie A*, 12(2):151–182, 1961.

[167] N. Untersteiner. Calculations of temperature regime and heat budget of sea ice in the central Arctic. *Journal of Geophysical Research*, 69(22):4755–4766, 1964.

[168] M. M. Van Dyne, C. Tsatsoulis, and F. Fetterer. Analyzing lead information from SAR images. *IEEE Transactions on Geoscience and Remote Sensing*, 36(2):647–660, 1998.

[169] M. Vancoppenolle, S. Bouillon, T. Fichefet, H. Goosse, O. Lecomte, M. Morales Maqueda, and G. Madec. The Louvain-la-Neuve sea ice model. *Notes du pole de modélisation, Institut Pierre-Simon Laplace (IPSL), Paris, France*, (31), 2012.

[170] M. Vancoppenolle, T. Fichefet, and C. M. Bitz. On the sensitivity of undeformed Arctic sea ice to its vertical salinity profile. *Geophysical Research Letters*, 32(16), 2005.

[171] K. Wang, J. Debernard, A. K. Sperrevik, P. E. Isachsen, and T. Lavergne. A combined optimal interpolation and nudging scheme to assimilate OSISAF sea-ice concentration into ROMS. *Annals of Glaciology*, 54(62):8–12, 2013.

[172] A. J. Weaver, J. Marotzke, P. F. Cummins, and E. Sarachik. Stability and variability of the thermohaline circulation. *Journal of Physical Oceanography*, 23(1):39–60, 1993.

[173] J. Weiss and E. M. Schulson. Coulombic faulting from the grain scale to the geophysical scale: lessons from ice. *Journal of Physics D: Applied Physics*, 42(21):214017, 2009.

[174] A. V. Wilchinsky and D. L. Feltham. Modelling the rheology of sea ice as a collection of diamond-shaped floes. *Journal of Non-newtonian Fluid Mechanics*, 138(1):22–32, 2006.

[175] J. Xie, F. Counillon, L. Bertino, X. Tian-Kunze, and L. Kaleschke. Benefits of assimilating thin sea ice thickness from SMOS into the TOPAZ system. *Cryosphere*, 10(6):2745, 2016.

[176] Q. Yang, S. N. Losa, M. Losch, X. Tian-Kunze, L. Nerger, J. Liu, L. Kaleschke, and Z. Zhang. Assimilating SMOS sea ice thickness into a coupled ice-ocean model using a local SEIK filter. *Journal of Geophysical Research: Oceans*, 119(10):6680–6692, 2014.

[177] Y. Yu and D. Rothrock. Thin ice thickness from satellite thermal imagery. *Journal of Geophysical Research: Oceans*, 101(C11):25753–25766, 1996.

[178] R. Zhang and G. K. Vallis. Impact of great salinity anomalies on the low-frequency variability of the North Atlantic climate. *Journal of Climate*, 19(3):470–482, 2006.

Appendix A

Appendix A

A.1 Dependent Tracers

Conservation equations for the dependent tracers such as level (non-deformed) ice fraction $a_{lvl}a_n$, pond ice fraction $a_{pnd}a_{lvl}a_n$, pond volume $h_{pnd}a_{pnd}a_{lvl}a_n$, pond ice volume $h_{ipnd}a_{pnd}a_{lvl}a_n$ are simlar to equation 3.9 [1] and is given by

$$\frac{\partial a_{lvl}a_n}{\partial t} + \nabla \cdot (a_{lvl}a_n\mathbf{u}) = 0, \tag{A.1}$$

All new ice growth is considered as level ice and hence the level ice area increases with the new ice formation and decreases with the ridging process. The ridged ice area fraction $a_{rdg} = a - a_{lvl}a$ and volume of ridged ice is $v_{rdg} = v - v_{lvl}v$. The level ice area fraction and volume increase with new ice formation and decrease with the

ridging process.

$$\begin{aligned}
\frac{\partial a_{pnd}a_{lvl}a_i}{\partial t} + \nabla \cdot (a_{pnd}a_{lvl}a_i\mathbf{u}) &= 0, \\
\frac{\partial h_{pnd}a_{pnd}a_{lvl}a_n}{\partial t} + \nabla \cdot (h_{pnd}a_{pnd}a_{lvl}a_n\mathbf{u}) &= 0, \\
\frac{\partial h_{ipnd}a_{pnd}a_{lvl}a_n}{\partial t} + \nabla \cdot (h_{ipnd}a_{pnd}a_{lvl}a_n\mathbf{u}) &= 0,
\end{aligned} \tag{A.2}$$

the melt water produced on a given category is added to the existing melt pond liquid volume by

$$\Delta V = \Delta V_{melt} + \Delta V_perm + \Delta V_{iso} + \Delta V_{ipnd} \tag{A.3}$$

where the terms in ΔV is represented by

$$\begin{aligned}
\Delta V_{melt} &= r(\rho_i \Delta h_i + \rho_s \Delta h_s + f_{rain}\Delta t))a_i, \\
\Delta V_{ipnd} &= -\Delta h_i a_{pnd}a_{lvl}a_i\rho_i/\rho_0, \\
\Delta V_{iso} &= (h_i - d)a_{pnd}a_{lvl}a_i, \\
\Delta V_{perm} &= a_i d_p min(h_pnd)pP\Delta t/\mu hi),
\end{aligned} \tag{A.4}$$

ΔV_{melt} includes changes associated with the accumulation of rain, snow, associated with melt ΔV_{perm} includes pond drainage associated with permeability, ΔV_{iso} includes isostatic adjustment, ΔV_{ipnd} inlcudes phase changes associated with pond ice, r is the fraction of the total melt water available that is added to the ponds, ρ_i and ρ_s are ice and snow densities, f_{rain} is the rainfall rate, $a_{lvl}a_n$ is the level ice fraction, a_{pnd} is a tracer on ice area, h_i is the ice thickness, d is the draft, d_p is a scaling factor, and $\mu = 1.79 \times 10^3 Kgm^{-1}s^{-1}$dynamic viscosity.

When new ice is added to a grid cell, the grid cell total area of melt ponds is preserved within each category gaining ice. Similarly, the total pond areas summed over the categories is also conserved.

$$a'_{pnd}(a_{lvl} + \Delta a_i)(a_i + \Delta a_i) = a_{pnd}a_{lvl}a_i, \tag{A.5}$$

Also, if a_i area of pond is zero in a grid cells thickness category, then all tracers that depend on it also becomes zero (similar is the case for the pond height tracer, h_{pnd}) [1]. The pond area is determined from

$$a_{pnd} = \frac{1}{\delta_p a_i} \sqrt{\frac{\Delta V}{\Delta t}} \tag{A.6}$$

A.2 Data Sources

North American Regional Reanalysis - http://www.esrl.noaa.gov/psd/

Climate Forecast System Reanalysis (CFSR) - https://climatedataguide.ucar.edu/climate-data/climate-forecast-system-reanalysis-cfsr

Sea Surface Temperature (SST) - http://www.esrl.noaa.gov/psd/

World Ocean Atlas (WOA) - https://www.nodc.noaa.gov/OC5/WOD13/

Bibliography

[1] E. C. Hunke, W. H. Lipscomb, A. K. Turner, N. Jeffery, and S. Elliott. CICE: the Los Alamos Sea Ice Model Documentation and Software Users Manual Version 5.1 LA-CC-06-012. *T-3 Fluid Dynamics Group, Los Alamos National Laboratory*, 675, 2015.

Appendix B

Appendix B

B.1 Significance of α

For significance of parameter α in the assimilation scheme in Section 4.5 see Figure

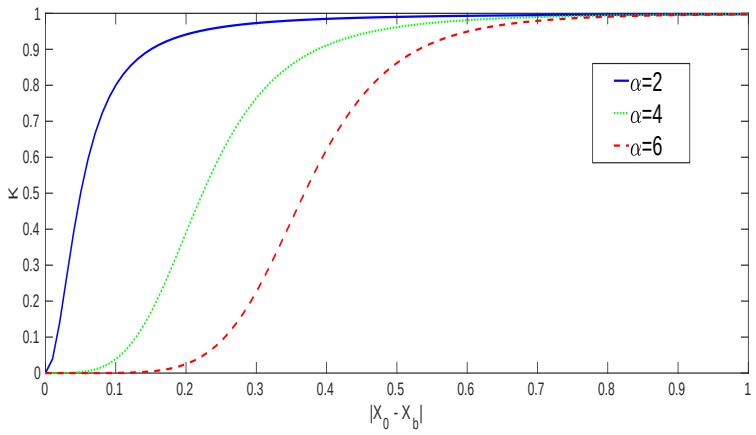

Figure B.1: The weighting factor K in the assimilation of ice concentration for $\alpha = 2, 4$ and 6

B.2 Updates of dependent tracers

To include assimilation of ice concentration to depended tracers level ice and melt ponds assumptions have been made as follows.

$a'_{lvl} = a_a - a_{rdg}$

$v'_{lvl} = v_a - v_{rdg}$

where a_a is the anlysis of ice concentration, v_a is the analysis of ice volume. The ridged ice from the model is preserved while assimilating ensuring that only the level ice areas and volumes are updated. In case there is no level ice then ridged ice area is assumed to be same as the ice area in the cell.

The meltpond areas are updated as

$a'_{pnd} = a_{pnd} a_{lvl} a_i / (a'_{lvl} a_a)$ All new ice areas that is added during assimilation is considered to have no melt ponds.

B.3 Ice thickness

This Appendix has figures of ice thickness form model M2, Observation and observation uncertainty.

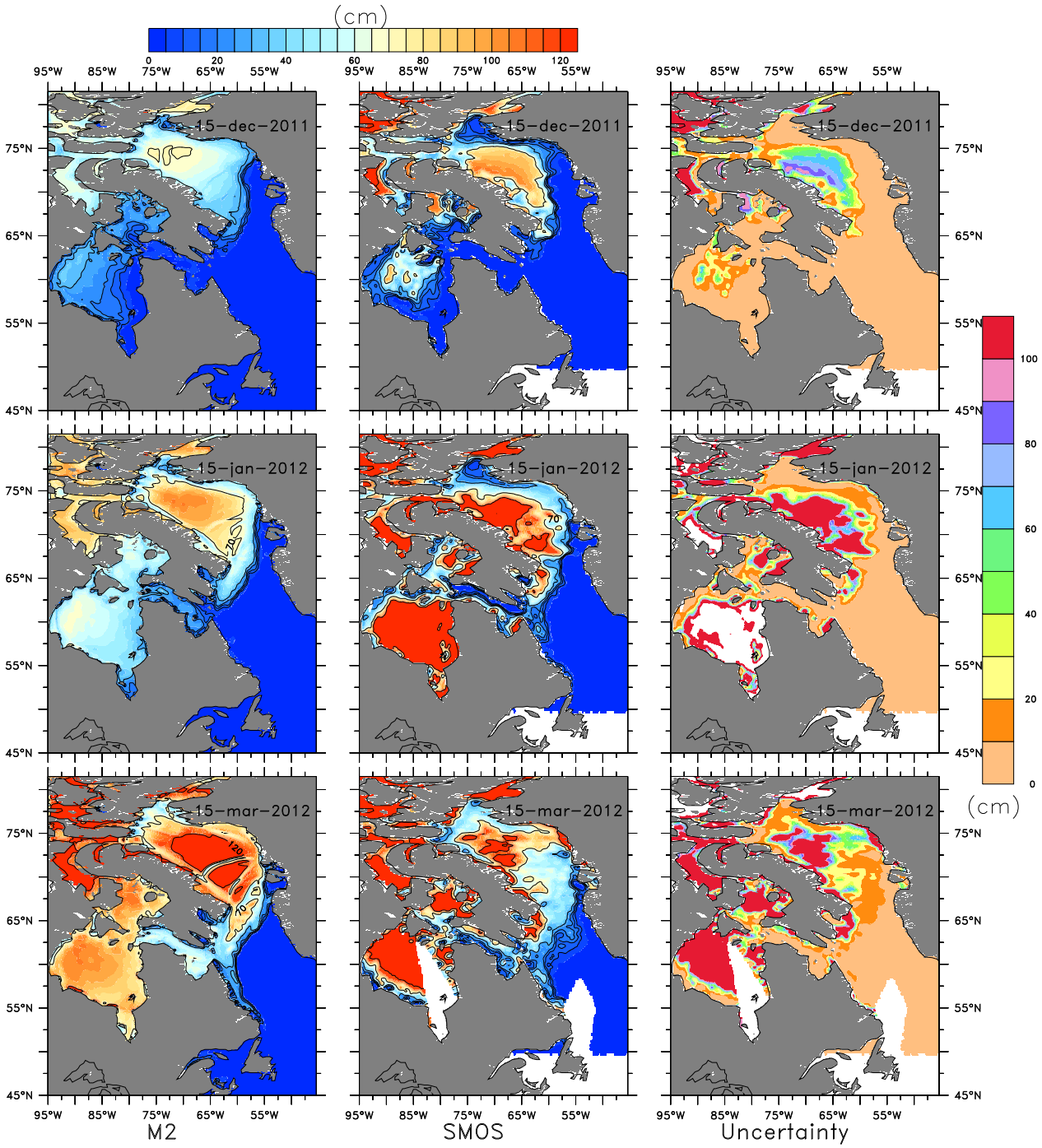

Figure B.2: The model 'M2' estimated ice thickness, ice thickness estimated from SMOS and SMOS uncertainty for 15 December, 15 January and 15 March 2011-2012.

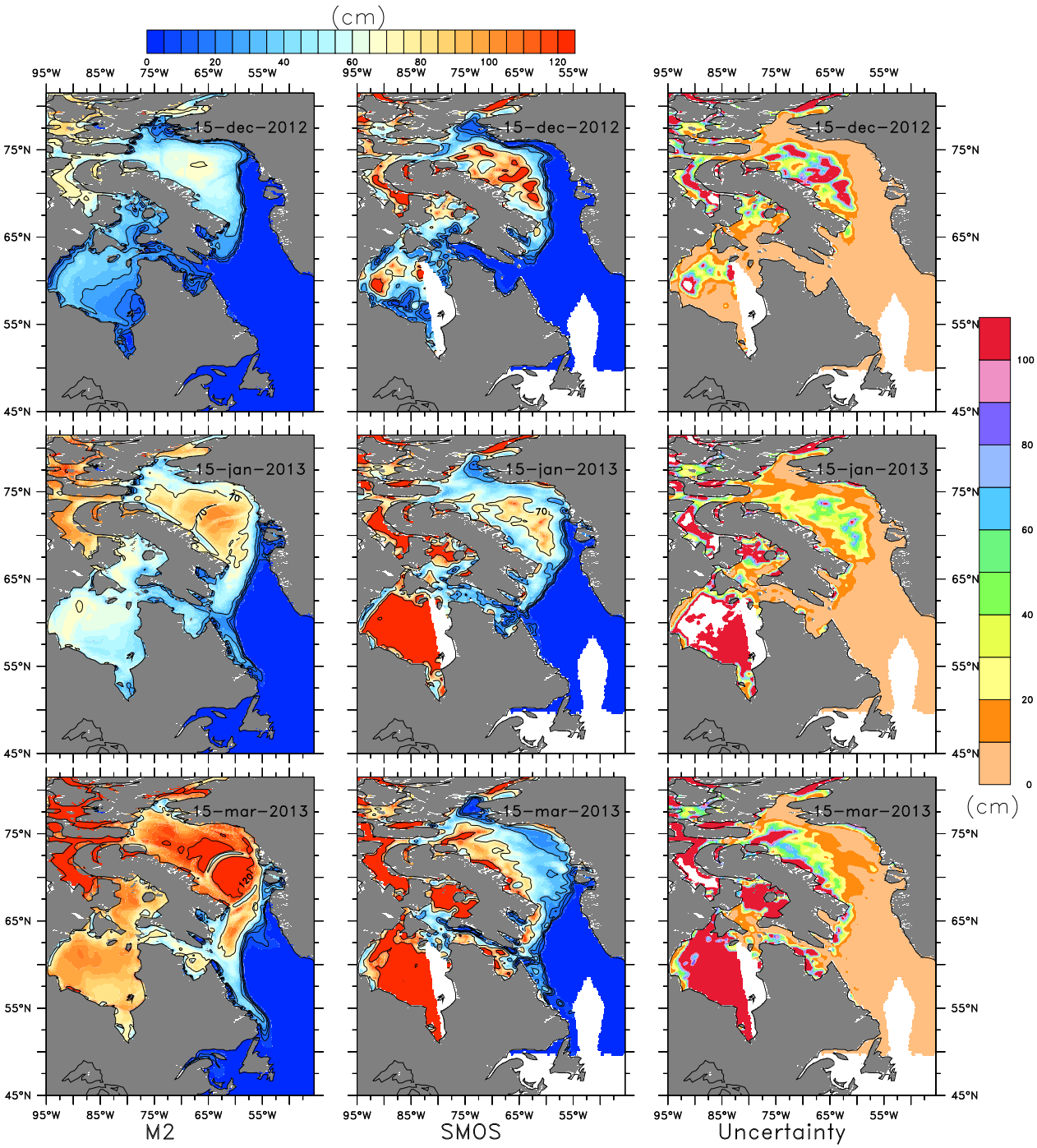

Figure B.3: The model 'M2' estimated ice thickness, ice thickness estimated from SMOS and SMOS uncertainty for 15 December, 15 January and 15 March 2012-2013.

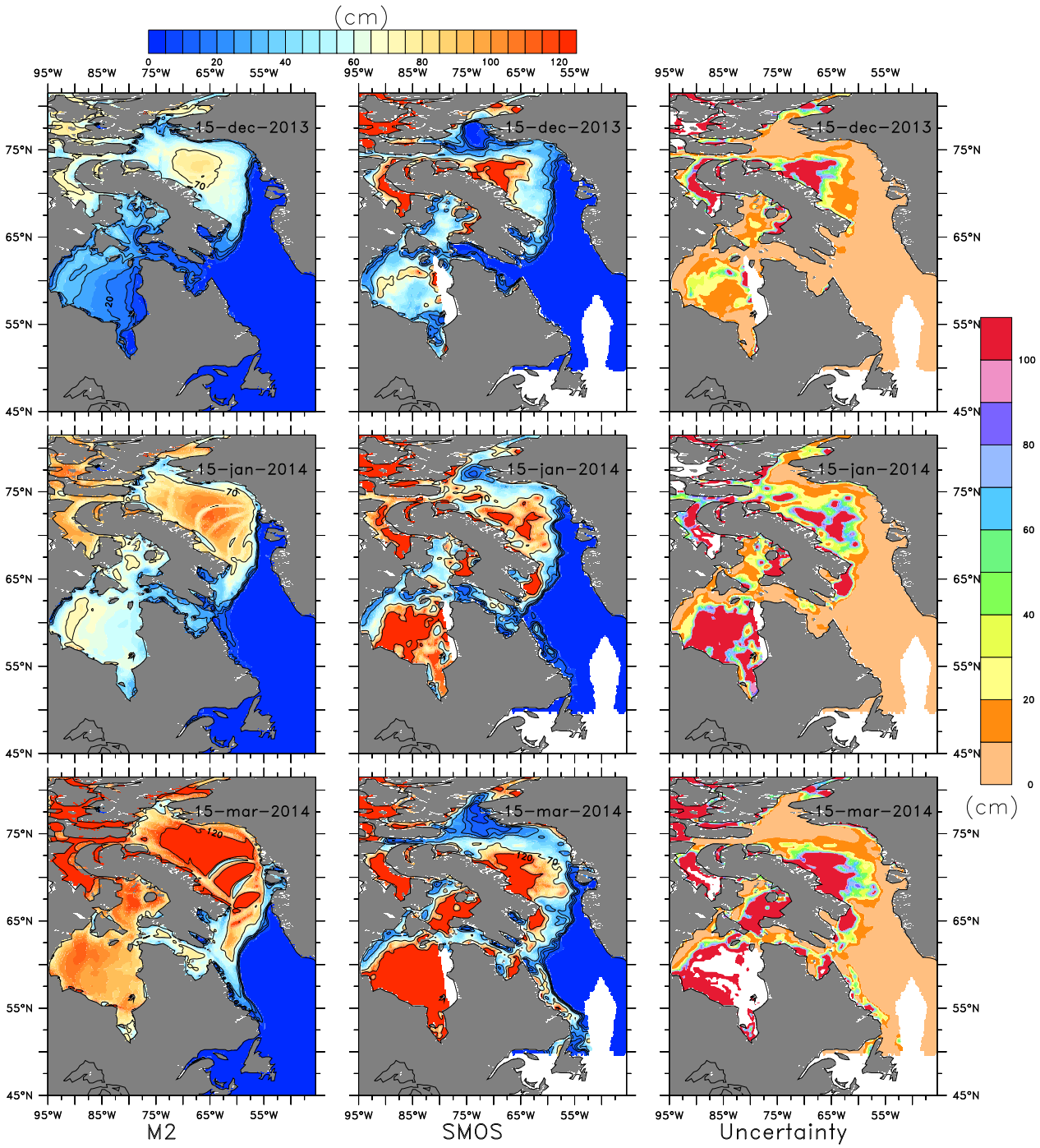

Figure B.4: The model 'M2' estimated ice thickness, ice thickness estimated from SMOS and SMOS uncertainty for 15 December, 15 January and 15 March 2013-2014.

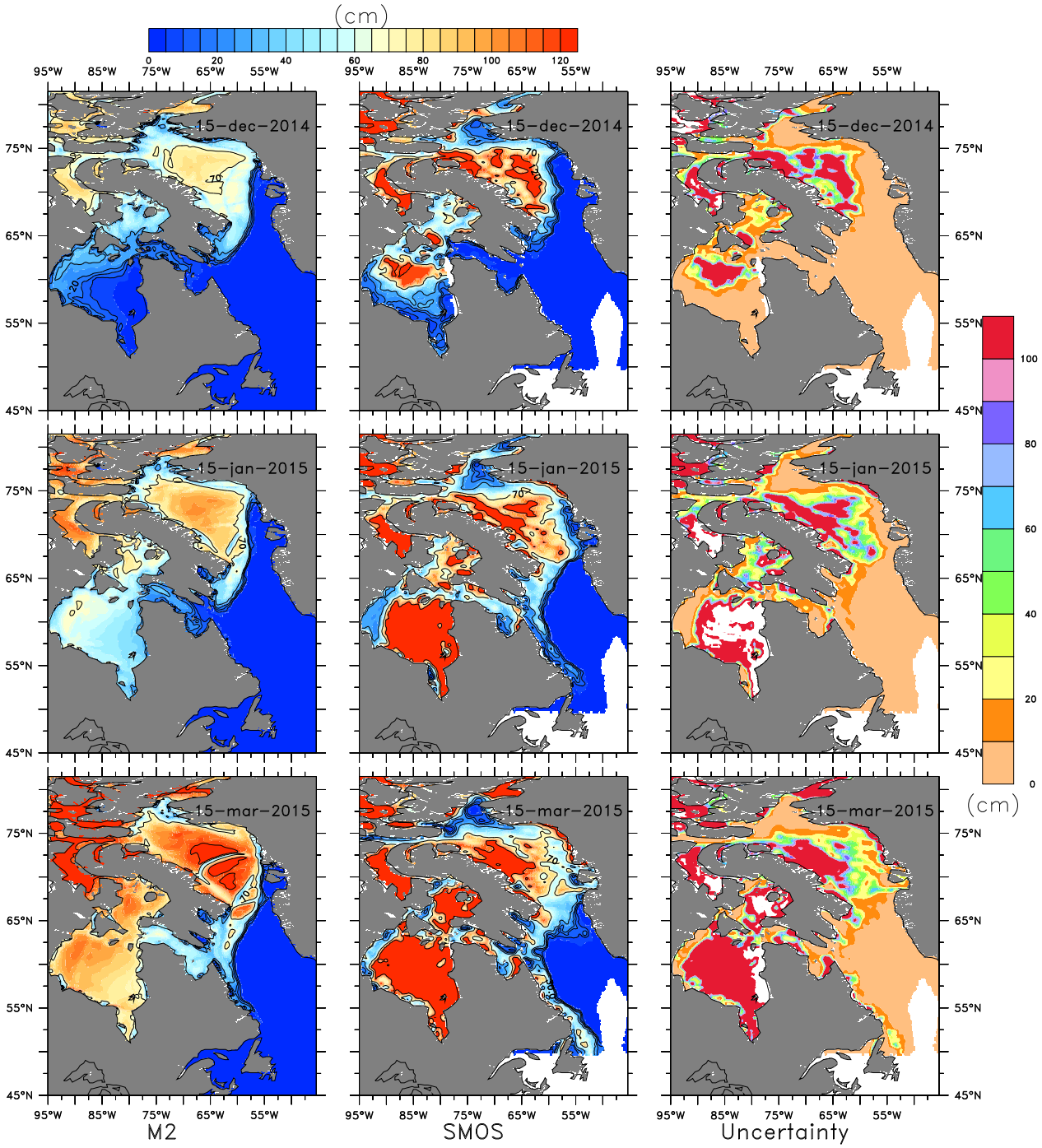

Figure B.5: The model 'M2' estimated ice thickness, ice thickness estimated from SMOS and SMOS uncertainty for 15 December, 15 January and 15 March 2014-2015.

B.4 Ice freeboard error

This Appendix has figures of freeboard absolute error in the regions where ice concentration is less than 90%.

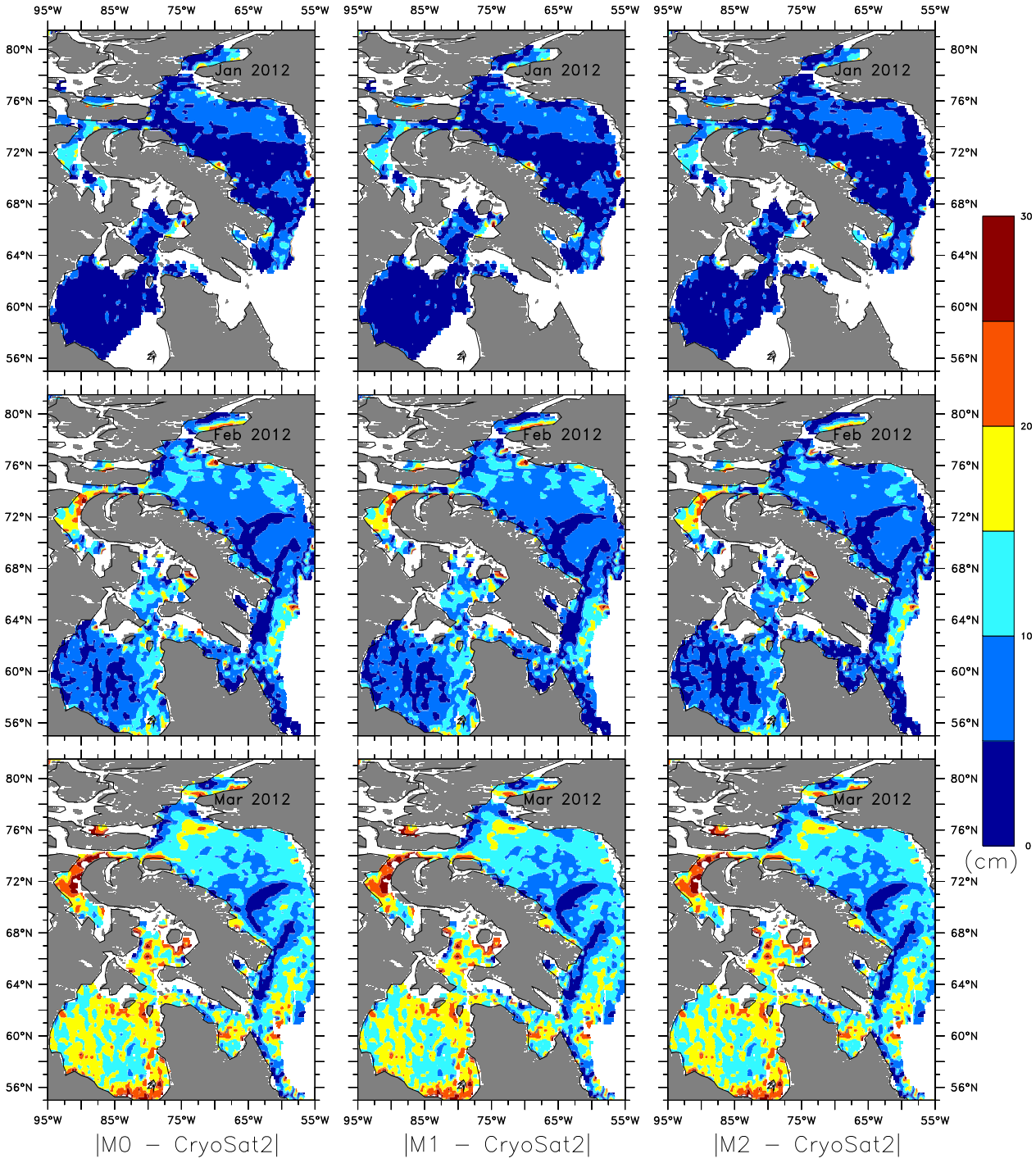

Figure B.6: The absolute error between the model freeboard and CryoSat-2 for 2012.

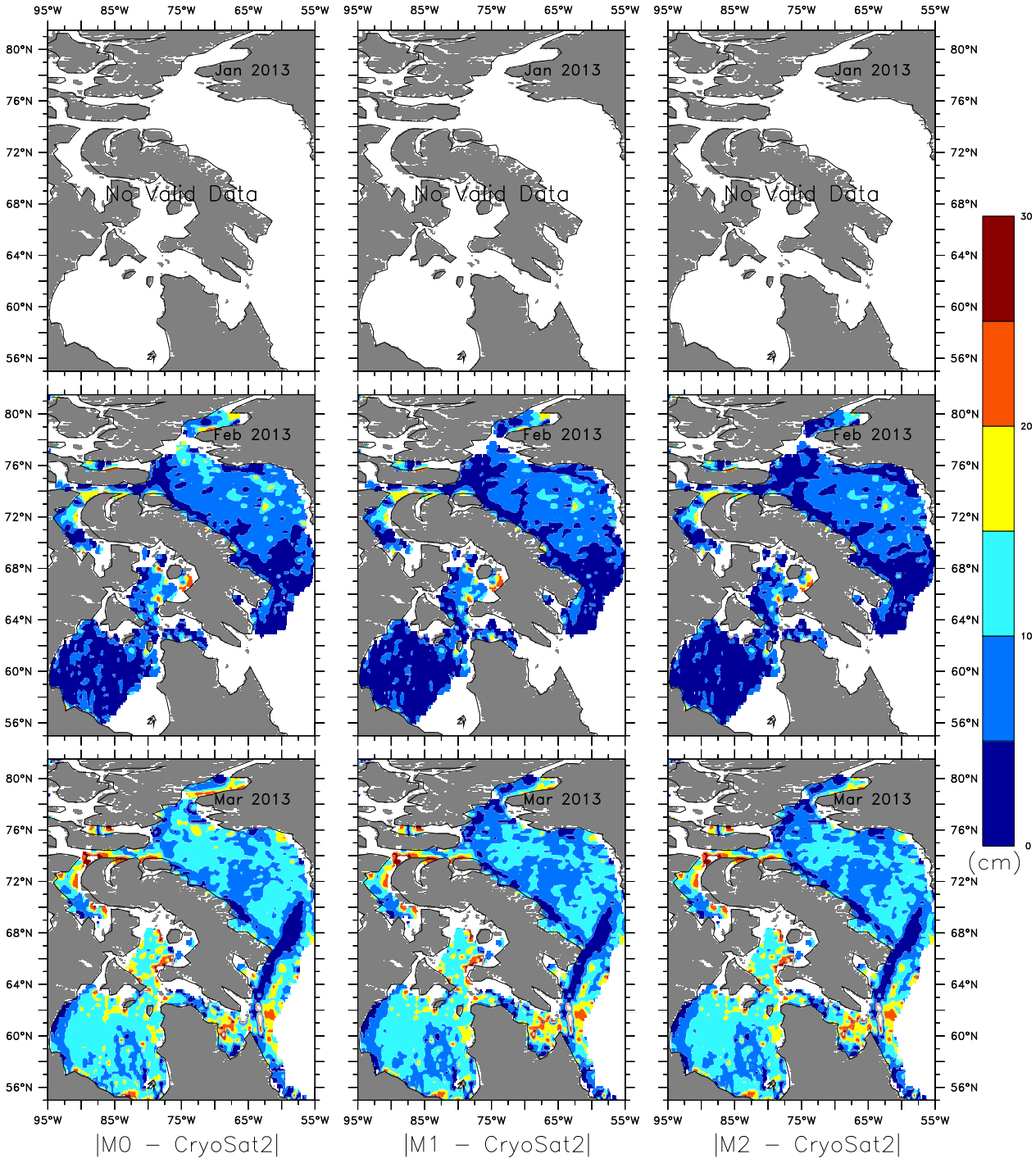

Figure B.7: The absolute error between the model freeboard and CryoSat-2 for 2013.

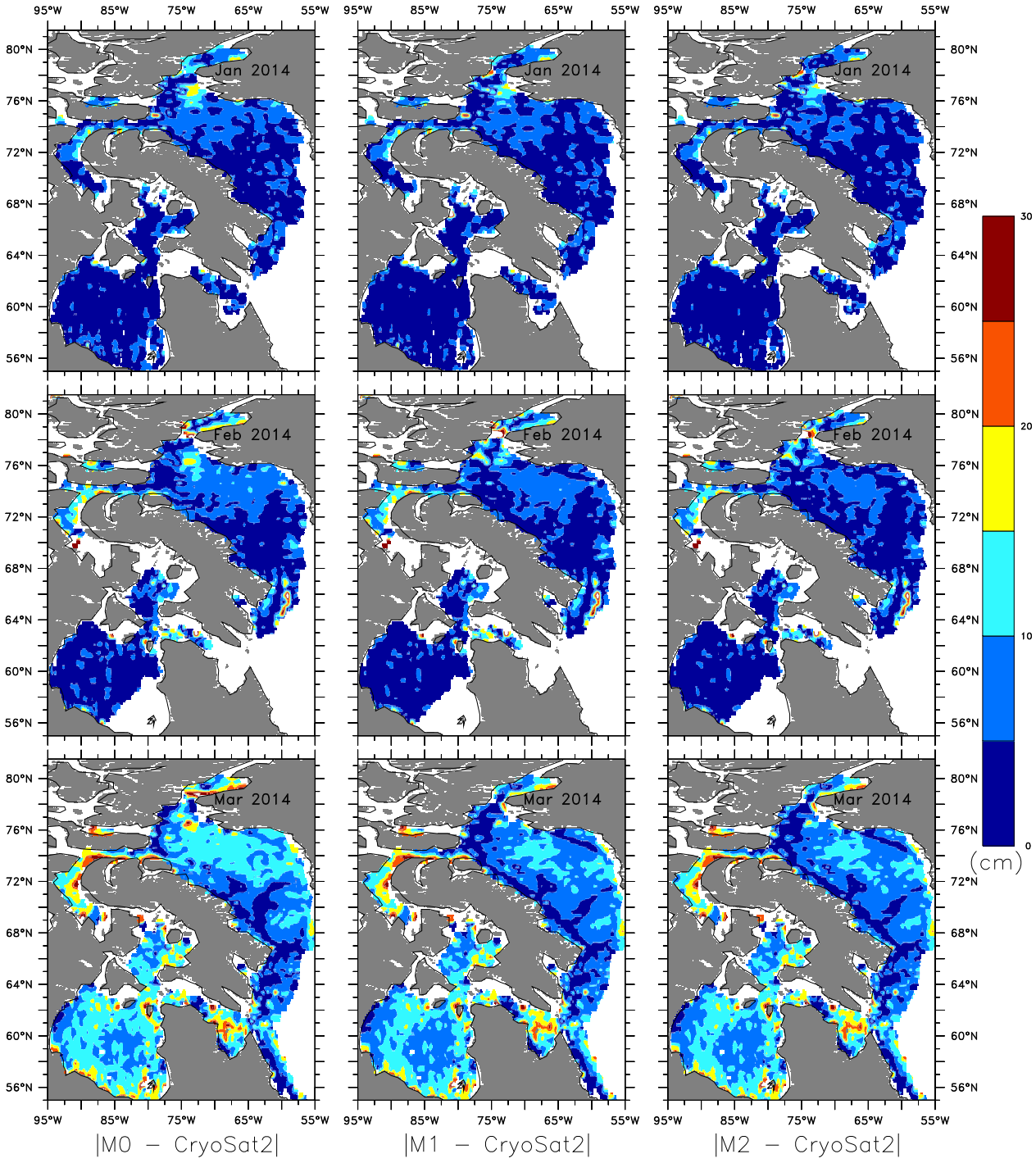

Figure B.8: The absolute error between the model freeboard and CryoSat-2 for 2014.

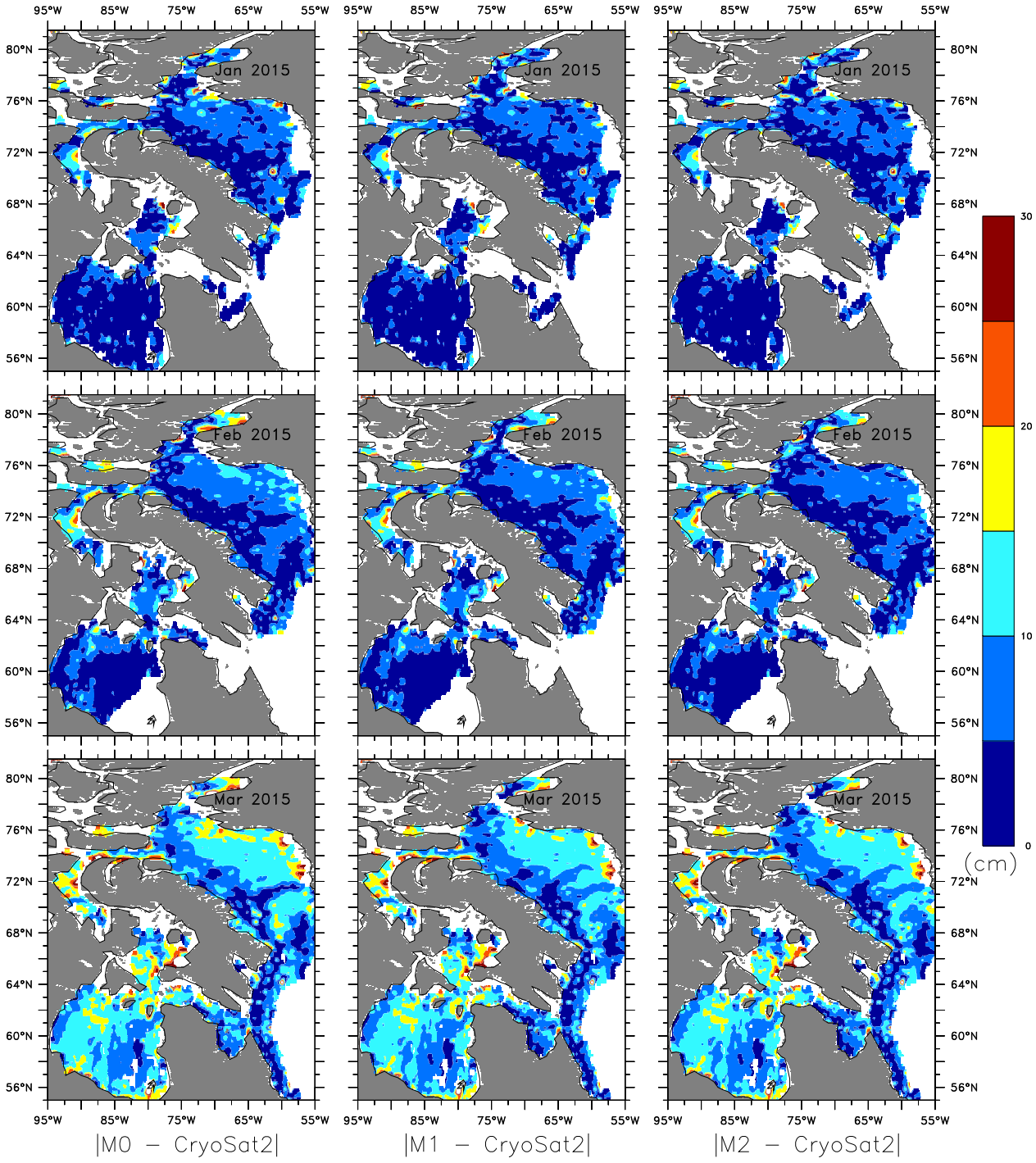

Figure B.9: The absolute error between the model freeboard and CryoSat-2 for 2015.

B.5 Ice freeboard

Figures of ice freeboard form model M2, Observation and observation uncertainty.

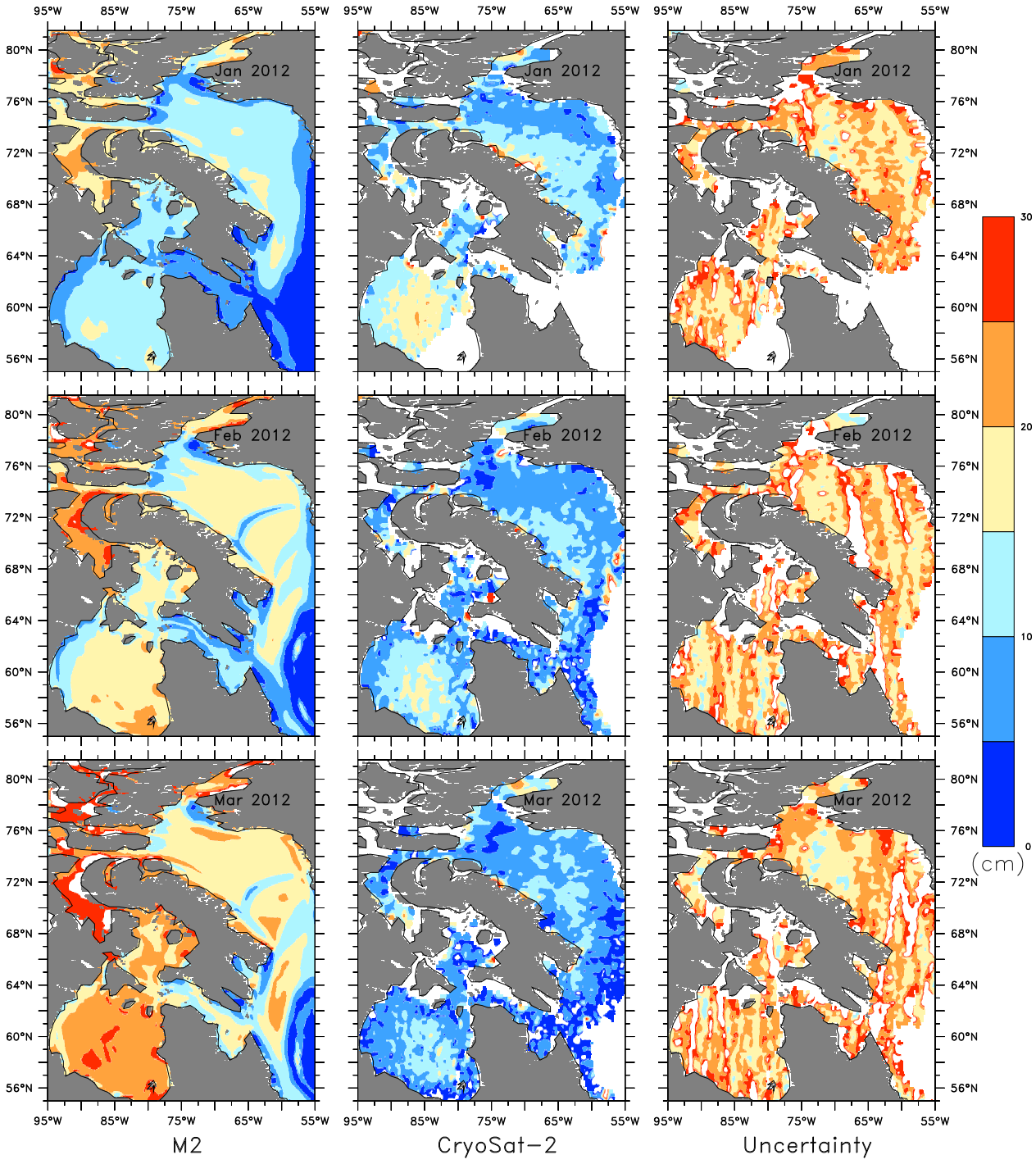

Figure B.10: The Freeboard from model M2, CryoSat-2 and the uncertainty of the observations for 2012.

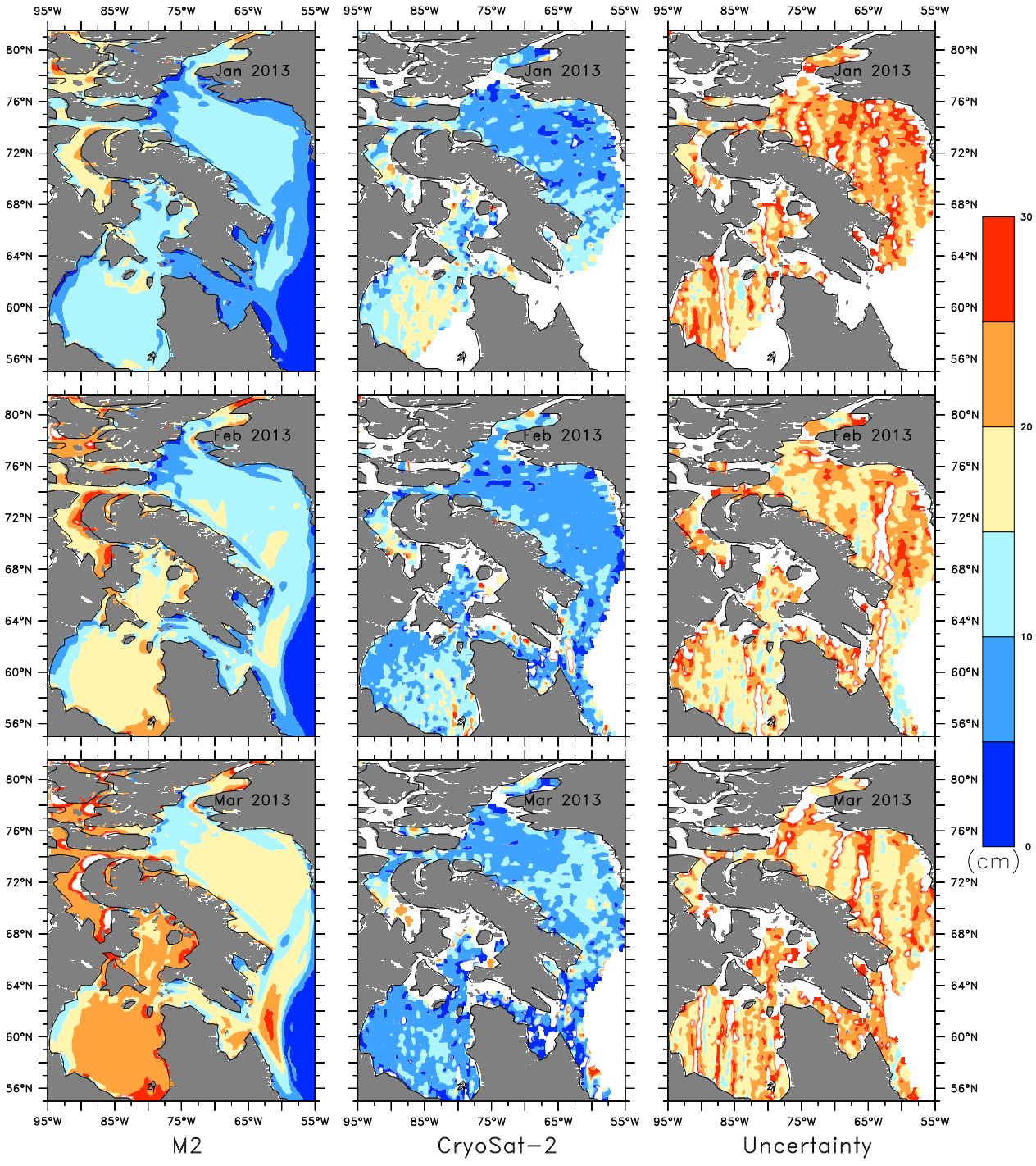

Figure B.11: The Freeboard from model M2, CryoSat-2 and the uncertainty of the observations for 2013.

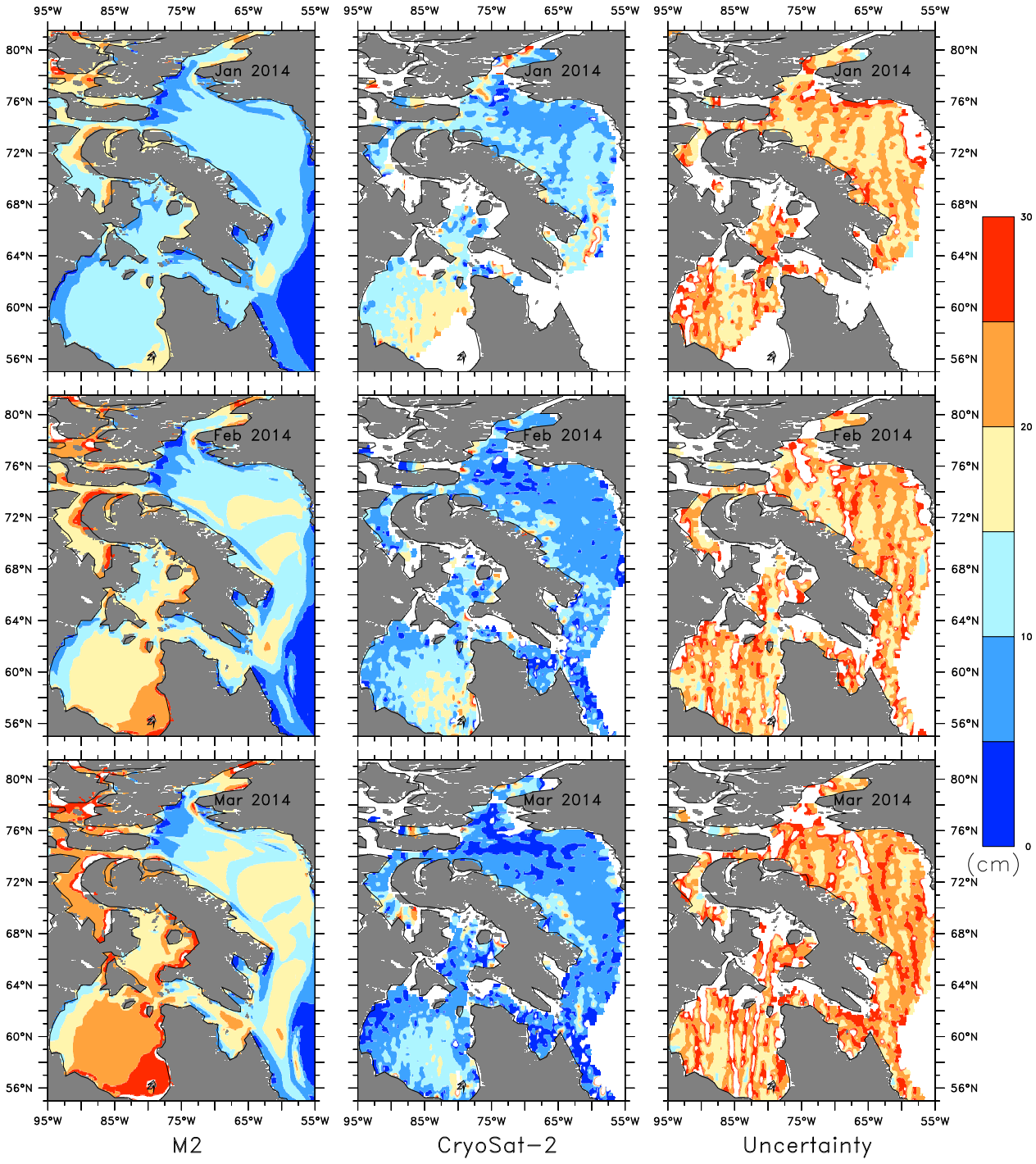

Figure B.12: The Freeboard from model M2, CryoSat-2 and the uncertainty of the observations for 2014.

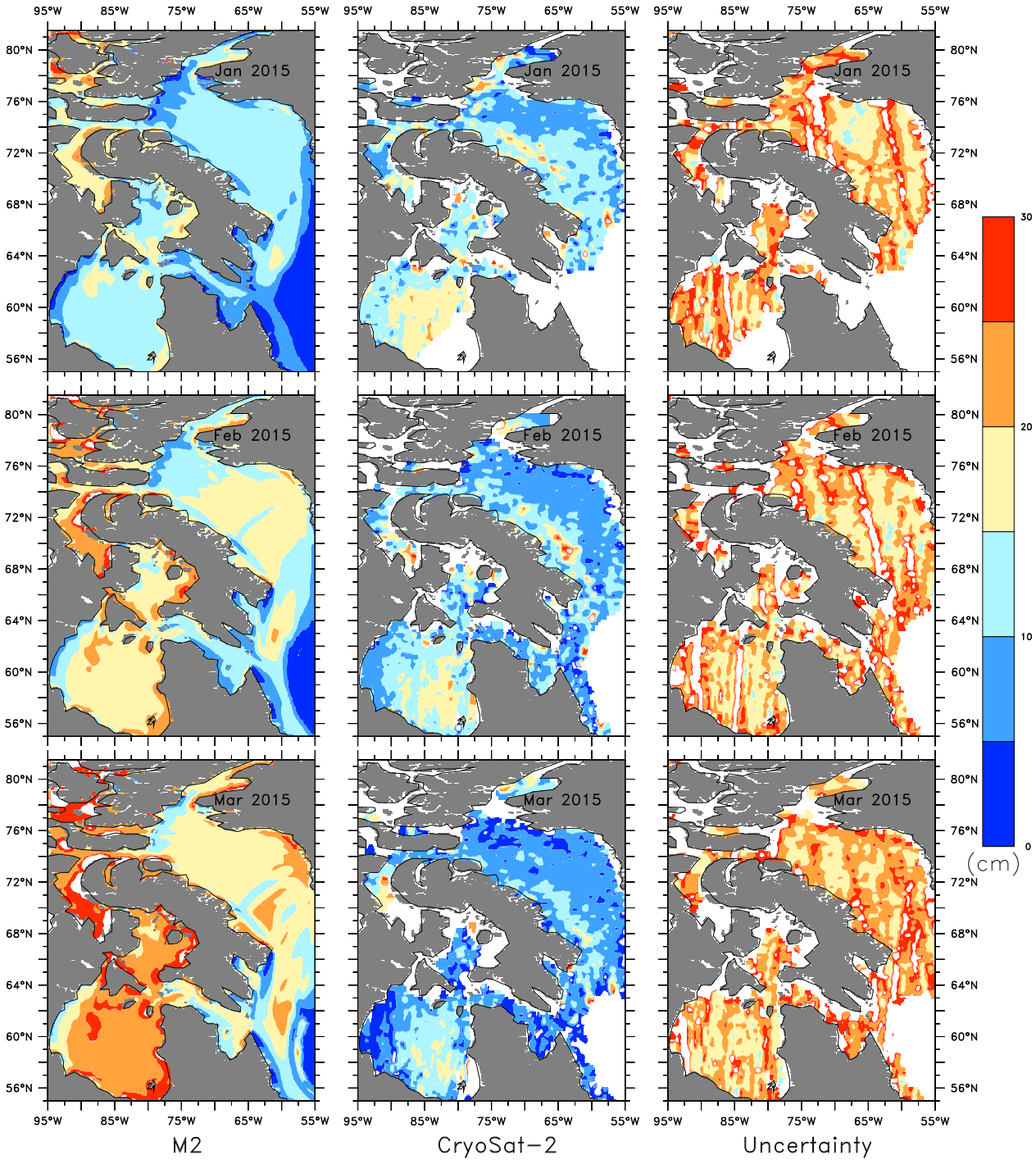

Figure B.13: The Freeboard from model M2, CryoSat-2 and the uncertainty of the observations for 2015.